TÉCNICO LISBOA

Comparison of Low and High-Fidelity Models in Structural Optimization of Strut-Braced Wings

Irene Pareja González

Thesis to obtain the Master of Science Degree in

Aerospace Engineering

Supervisors: Prof. Afzal Suleman
Prof. Frederico José Prata Rente Reis Afonso

Examination Committee

Chairperson: Prof. Fernando José Parracho Lau
Supervisor: Prof. Frederico José Prata Rente Reis Afonso
Member of the Committee: Prof. Pedro Vieira Gamboa

September 2021

Acknowledgments

I would like to pay my special regards to my supervisors Professor Afzal Suleman who brought me the opportunity to realize this project, Professor Frederico Afonso who read everything and sent me feedback to make me appear far more competent and knowledgeable than I actually am and, last but not least, Professor Jose Lobo do Vale who patiently offered me advice, knowledge and loads of help, without their virtual help this project would not have been realized.

I wish to express my deepest gratitude to the European exchange program, Erasmus+, that the Polytechnic University of Valencia granted me. I would not have had the opportunity to do this project and to finish my engineering studies in the Instituto Superior Técnico without it.

I want to acknowledge the trust and encouragement of my friends during my whole engineering studies, they believed in me even when I did not. Thank you for their friendship and for all the exciting non-engineering moments. Also, I want to thank everybody that supported me to continue my sport career at the same time than the engineer one. Thank you for cheering me up when it seemed more complicated than it was and for celebrating it when we achieved our goals. “If you want to go faster, go alone, if you want to go further, go together”.

I finally want to thank my family for the support, moral and financial, that they have offered me to be here. Thank you to my mother and brother for the commitment and endless love. Thank you to my dad for giving me the passion for airplane design, for supporting me in every single decision I have taken and for encouraging me to go further. For this reason, I want to dedicate this project to him.

Resumo

Este trabalho visa estudar a aplicabilidade de um modelo estrutural de Baixa Fidelidade (BF) para a análise e otimização de uma aeronave do tipo *Strut-Braced Wing* (SBW). Para atingir este objetivo, primeiro o comportamento da estrutura quando sujeita a dois carregamentos aerodinâmicos, cruzeiro e manobra de *pull-up*, é comparado com um modelo de Alta Fidelidade (AF). Posteriormente são formulados três problemas de otimização que têm como objetivo obter uma boa correspondência de comportamento estrutural entre estes dois modelos para a condição de cruzeiro. Os dois primeiros problemas de otimização utilizam a distribuição de espessura ao longo da estrutura para atingir esse objetivo, sendo o primeiro não constrangido e o segundo constrangido por uma massa mínima e uma tensão máxima para a manobra de *pull-up*. No terceiro problema, também é permitido alterar a distribuição de torção e são considerados os mesmos constrangimentos do segundo problema. Apenas foi encontrada uma solução viável em termos de tensão para o terceiro problema de otimização. No entanto, ao analisar a deformação, observa-se que o modelo AF otimizado apresenta diferenças em relação ao modelo BF superiores a 10 %. Embora o modelo BF seja vantajoso do ponto de vista computacional, quando comparado ao modelo AF este subestimou tanto a tensão quanto a deformação. Portanto, o modelo BF só deve ser usado para fornecer tendências gerais numa fase preliminar do projeto de uma estrutura SBW. Para uma fase mais avançada do projeto, o modelo AF deve ser utilizado.

Palavras-chave: Modelo Estrutural de Alta Fidelidade; *Strut-Braced Wing*; Análise e Otimização de Estruturas Aeronáuticas; Modelo de Elementos Finitos.

Abstract

The aim of this work is to study the applicability of a Low-Fidelity (LF) structural model for analyzing a given Strut-Braced Wing (SBW) configuration within an optimization environment. To accomplish this goal, the behavior of the structure when subjected to two aerodynamic loads, cruise and pull-up, is firstly compared with a High-Fidelity (HF) model, and then a match between both models is sought. Two optimization problems, one unconstrained and another constrained, set to match the deformed shape of the LF model in the HF one for cruise conditions by changing the thickness distribution, are defined and solved. An additional constrained problem that allows changing the twist distribution is defined as well. Mass and stress for pull-up maneuver conditions are set as constraints for the two constrained problems. A feasible solution in terms of stress is only found when the twist distribution is set as a design variable. However, when analyzing the deformation, the optimized HF model is observed to have differences relative to the LF model higher than 10%. Even though the LF model is computationally advantageous, it underestimated both stress and deformation when compared to the HF model. Therefore, the LF model should only be used to provide general trends at a preliminary design phase of a SBW structure. For a more advanced design stage the HF model should be employed.

Keywords: High-Fidelity Structural Model; Strut-Braced Wing; Structural Design and Optimization; Finite Element Model.

Contents

List of Tables

List of Figures

Chapter 1

Introduction

1.1 Motivation

Aviation industry connects people, cultures and businesses across continents. It is the only rapid worldwide transportation network, which makes it essential for global business. It has several advantages but also some disadvantages. The main disadvantage are the air and noise pollutions [1].

Historically, air transport has doubled in size every 15 years, growing faster than most other industries. As it is expected to continue growing by connecting more people and more places, more often, it is necessary to support the sustainable growth of aviation. This trend has been interrupted by the Covid-19 pandemic, however, some projections predict a growth of air transportation to pre-pandemic situation in few years time [1, 2].

In terms of the economy, airlines suffer financial losses in paying fines for emitting excessive pollutants so a reduction of the pollutant emissions is beneficial for them and for the climate. The International Civil Aviation Organization (ICAO) announced in 2009 a set of sequential goals for air transport to reduce carbon emissions. The CORSIA project (Carbon Offsetting and Reduction Scheme for International Aviation) is a global scheme for the global international aviation industry created by ICAO [3].

The aim of aerospace engineering is to make existing aircraft more efficient. For that purpose, new aircraft concepts are being studied. The Strut-Braced Wing (SBW) configuration is one of the concepts being proposed for the next generation of commercial aircraft due to its potential for fuel burn savings, compared to an equivalent conventional configuration [4].

1.2 Background

This work aims at studying a Strut-Braced Wing (SBW) structure which is one of the configurations being proposed for the next generation of commercial aircraft. The greatest virtues of the SBW are an

improvement in fuel consumption and a smaller engine size, which means that the SBW would cost less to operate, limit pollutant emissions and reduce noise pollution in urban airports. However, the main disadvantage when adding a strut is the significant drag penalty [5, 6]. Some SBW research projects that have been investigated [7–9] showed that the SBW configuration, in terms of design, allows to increase significantly the wing aspect ratio, reduce the wing sweep angle and profile thickness. In addition, all of them concluded that SBW configuration has the potential for fuel burn savings, compared to an equivalent conventional configuration [4].

In order to design it the most efficiently possible, computational tools that integrate the main aircraft disciplines in one problem for Multidisciplinary Design Optimization (MDO) are desired. However, in a typical aircraft the high dimensionality of the problem might turn these computational tools very costly timewise. Thus, multi-fidelity approaches within MDO are being developed and applied to aircraft design problems [10–13].

MDO can be used to design SBW since it allows to incorporate all the relevant disciplines simultaneously to obtain the most desirable trade-off between them [14]. The complexity of MDO in aircraft analysis and design comes from the fact that aerodynamics, structures and performance are coupled. This problem is solved with numerical optimization [15]. Typically, coupled MDO based on computational fluid dynamics/computational structure dynamics (CFD/CSD) aims to optimize the jig shape of aircraft.

Traditional coupled aero-structural design optimization [16–18] of aircraft based on high-fidelity models is computationally expensive and inefficient. To improve the efficiency, the key is to predict aero-structural performance of the aircraft [19]. The most popular aero-structural prediction method is the loosely coupled aeroelastic analysis for its simplicity. It has been studied a coupled aero-structural wing shape design by using Reynolds-Averaged Navier–Stokes (RANS) solver for aerodynamics and NASTRAN for structures and aeroelasticity [20], which are high-fidelity simulation tools. The study concluded that the Euler/RANS solver was still be too expensive for the real-world design environment. There is a methodology named reverse iteration of structural model (RISM) whose main advantage is that it quadruples the efficiency compared with loosely coupled aeroelastic analysis, maintaining almost the same fidelity of this last one [21]. To reduce the computational cost of these simulations, multi-fidelity approaches can be followed. The multi-fidelity calculation method combines low and high-fidelity discipline codes [12]. The purpose is to provide a way to minimize the usage of high-fidelity models to reduce overall computational cost [11] and accelerate convergence of the design problem [22]. The conceptual design phase begins with low-fidelity calculations. Once this phase is completed, the preliminary design can start by recurring to medium-fidelity models [12]. To use high-fidelity methods is very challenging from the design optimization perspective [23, 24], thus multi-fidelity strategies, especially with surrogate models, are preferred.

1.3 Objectives

The overall objective of this thesis is to compare the structural and shape optimization results for validation of a Low-Fidelity (LF) structural model used in surrogate based MDO of a SBW configuration. For this purpose, the specific objectives of the optimization in this thesis are as follows.

- Perform structural optimization in a High-Fidelity (HF) structural model in order to match the deformation resulting from LF structural model based Fluid-Structure Interaction (FSI) analysis for one SBW configuration under a cruise flight loading.
- Perform shape optimization in a HF structural model in order to find the jig shape that under the same load matches the predetermined deformed cruise shape by a LF structural model based FSI for one SBW configuration, starting from the same optimized structure resulting from a (LF structural model based) MDO procedure.

1.4 Methodology

The methodology followed in this thesis can be broken down into different steps that are presented below and are explained in detail throughout the Chapters of the project.

1. Definition and parameterization of the High-Fidelity structural model in ANSYS Mechanical.
2. Comparison of the High and Low-Fidelity structural models results to assess the similarity between the loaded wings on the achieved results.
3. Estimation of the structure deformation condensed to the Low-Fidelity beam model nodes.
4. Optimization of the structure such that the same deformation of the Low-Fidelity beam model is reached.
5. Draw conclusions about the optimization and the results obtained.

1.5 Thesis Outline

This thesis has been structured as follows:

- Chapter 1: this chapter introduces the thesis subject giving an overview of the Strut Braced Wing (SBW), Multidisciplinary Design Optimization (MDO) and the aero-structural design optimization. In addition, it presents the overall objective and the methodology followed throughout the project.
- Chapter 2: contains the literature review of the SBW and MDO, summarizing the state of the art.
- Chapter 3: describes the problem solved in this optimization project, including the case study, computational tools used, modelling methodology, type of elements and loads used, mesh convergence study and a nonlinear analysis to check if there is buckling when applying the case study loads.

- Chapter 4: explains the whole optimization process followed in the project detailing the optimization problem formulation and algorithms, the case study solution and High and Low-Fidelity results comparison.
- Chapter 5: details the optimization results computed for the unconstrained, constrained and jig shape optimizations.
- Chapter 6: concludes the thesis presenting the major achievements of it and some ideas for future work.

Chapter 2

Literature Review

2.1 Strut Braced Wing (SBW)

Strut-braced wing configurations have been used both in the early days of aviation and today's small airplanes. This configuration consists on a conventional wing supported by a pair of struts, one for each wing. It has several structural and aerodynamic advantages and disadvantages that are discussed below.

2.1.1 Airplanes with SBW

During the early years of aviation, bracing was a universal feature of all forms of airplane, including the monoplanes and biplanes which were then equally common. Today, bracing in the form of lift struts is still used for some light aircraft designs where a high wing and a light weight are more important than ultimate performance [25, 26].

Early days

Throughout the history of the aviation, many airplanes with Strut Braced Wing can be found. The first aircraft designed and built was the Wright Flyer in 1903. This aircraft had biplane configuration and the two wings were supported with two light wires. In addition, it had vertical struts which made it more resistant to bending and twisting. This concept has been used until today.

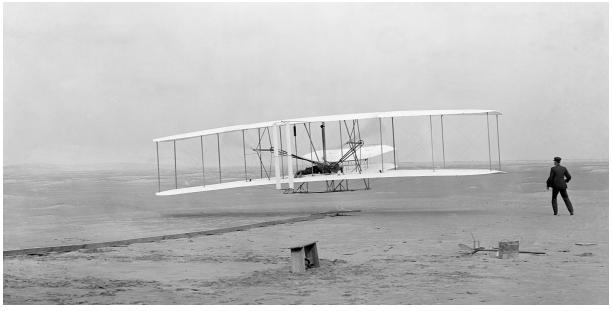

Figure 2.1: Wright Flyer aircraft [27]

At the beginning of the aviation, monoplane, biplane and multiplane configurations had to include struts in their structure to support the weight of the wing. As years have been passing, a lot of investigation and development such as [28–32] has been done and nowadays is possible to use cantilever wings with higher aspect ratio.

Today's small airplanes

Nowadays, Strut Braced Wing are used in small airplanes to make their wing structure lighter and stiffer than a cantilever structure due to the fact that weight saving in that kind of aircraft is essential [33]. Many Cessna models include SBW to brace the wing against lift-induced bending loads by a single strut.

Figure 2.2: Cessna 180 aircraft with SBW configuration [34]

Projects under development

Boeing company is developing its Truss-Braced Wing which is an airliner design with a braced and high aspect ratio wing. One of the developments is the SUGAR (Subsonic Ultra Green Aircraft Research) Volt [8] which is a hybrid aircraft concept proposed by a team led by Boeing's Research & Technology division. It is one of a series of concepts put forward in response to a request for proposals for future aircraft issued by NASA.

SUGAR Volt would have emissions about 70 percent lower than average airliners today. Noise pollution will also be lower than airliners today. SUGAR Volt is designed with a long, braced and high aspect ratio wing that decreases induced drag. The wings of SUGAR Volt would enable it to take off in a shorter distance and generate less noise. The outer wings of the SUGAR Volt should fold to save ground space, increasing weight. NASA is doing test aircraft to evaluate several next-generation, efficiency-improving technologies that could be incorporated into the next single-aisle commercial aircraft, which manufacturers will likely bring to market in the 2030s [36].

In addition to the Boeing project, Lockheed Martin Aeronautical Systems (LMAS), Virginia Polytechnic Institute and State University's (Virginia Tech) [7] and ONERA (French Aeronautics and Space

Figure 2.3: SUGAR Volt development project [35]

Research Center) [9] have recently done research projects about how to improve fuel savings in transport aircraft. All of them have concluded that the SBW configuration has fuel burn savings compared to equivalent conventional configuration. The results of the studies suggest fuel burn savings between 5-10% compared to an equivalent conventional configuration [4].

2.1.2 Advantages and disadvantages of SBW configuration

Adopting thin airfoil sections require external structural wing support to sustain the aerodynamic loads [5]. Favorable interactions between structures, aerodynamics and propulsion give the SBW potential for higher aerodynamic efficiency and lower weight than a cantilever wing [7]. The positive and negative outcomes are going to be detailed below.

On the one hand, the main disadvantage to add a strut is the significant drag penalty. Without an external structure a lower drag could be achieved using a cantilever wing with an appropriate wing-box and thickness to chord ratios. Moreover, there is some additional drag penalty due to interference of the junctions at the ends of the strut, but this can be mitigated by well-designed junction fairings [5, 6].

On the other hand, Strut Braced Wing configuration has numerous advantages compared to the cantilever wing configuration. The main advantage is that the use of wing struts can alleviate stress and reduce weight [37]. This stress reduction offers the opportunity to increase the wing aspect ratio which results in direct aerodynamic performance gains which implies a significant decrease of the induced drag without wing weight penalties relative to a cantilever wing.

Also, the stress reduction makes a lower wing thickness to become feasible which reduces transonic wave drag and hence resulting in a lower wing sweep. Reduced wing sweep and high aspect ratios produce natural laminar flow due to low Reynolds numbers. Consequently, a significant increase in the overall aircraft performance is achieved which added to the weight reduction due to the possibility to have a lighter structure results in a significant fuel consumption reduction. Hence, the operating cost

of the SBW is slightly less than the cantilever one which is economically interesting for the aeronautical industry [5, 37–39].

Finally, it should be noted that, in addition to the reduction in the operating cost, the pollutant and noise emissions will be lower. The noise reduction comes from a reduction of the engine size as a result of a reduction of the overall weight and an improvement in the aerodynamic efficiency [7]. This reduction in both pollutant and noise emission is an advantage for aircraft operating in urban airports.

2.1.3 SBW geometry

There are many designs of Strut Braced Wings. The strut can be over or under the wing depending on the wing configuration or even between both wings in the biplane configuration as in Figure 2.1. In this project is going to be studied the design of a high cantilever wing with a strut in order to assess the differences between a High and Low-Fidelity model. It should be noted that this design is the one that is being studied in all the projects under development.

The aircraft configurations that have Strut Braced Wings is high wing with standard or T-tail. The strut is under the wing and connects the lower surface of it with the lower part of the fuselage. In Figure 2.4 it is shown the strut configuration with all its parameters.

2.1.4 Challenges

Airplanes with SBW configuration are predicted to be more expensive to build than cantilever configuration airplanes due to the higher wing size and complexity [41]. One of the challenges for the SBW configuration is to ensure that the higher cost of production will be covered by the profits during the service life of the aircraft.

Despite all the benefits that SBW configuration has, it is more likely to have aeroelastic problems, such as increased static aeroelastic deformation or reduced flutter and divergence speeds, than cantilever configuration. The main reason is that the reduction on the wing thickness together with shorter wing chords result in smaller wing-box dimensions, thus significantly reducing wing-box torsional stiffness [5]. Therefore, improvements in material science could be a solution for these problems.

One of the main uncertainties of the design is related to the wing and strut weight. Due to the unconventional characteristics of the SBW, design-sensitive wing weight estimation methods must be developed to perform reliable feasibility studies. In this context, [42] presents a method for application in conceptual design. Moreover, Bombardier has developed the ASPER tool for SBW weight estimation, which is shown to adequately capture the large differences in stiffness due to the strut [4].

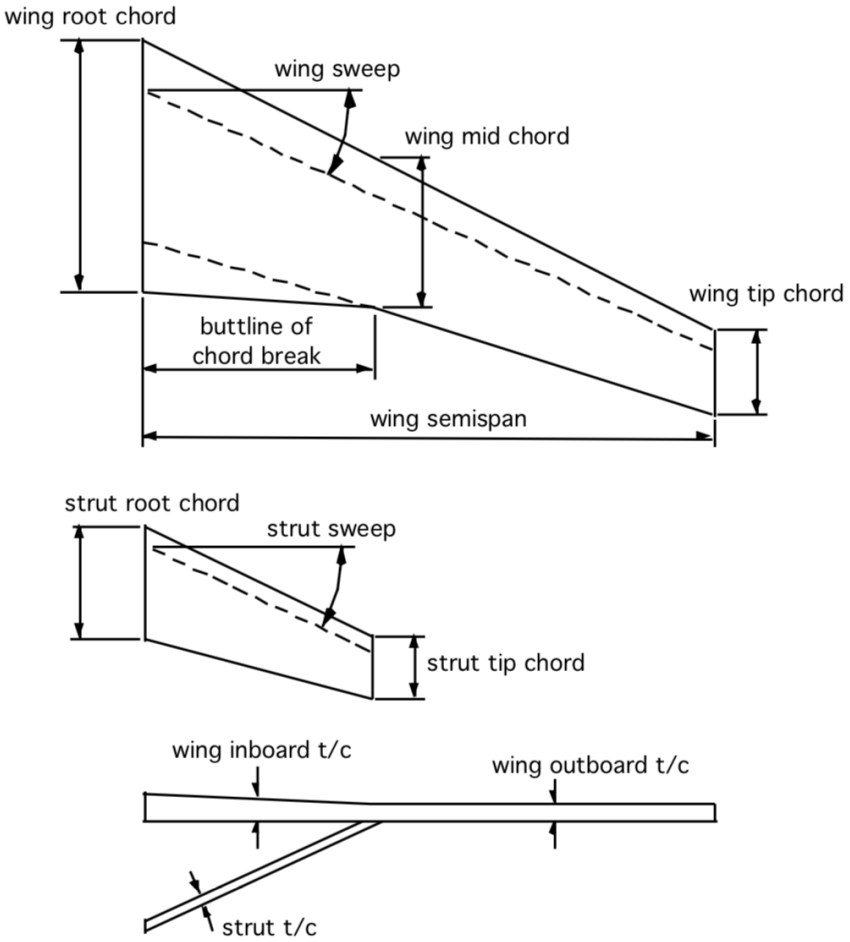

Figure 2.4: SBW configuration [40]

The buckling of the strut under negative maneuvers proved to be the critical structural design challenge in the single-strut configuration [43, 44]. To avoid strut buckling, a telescoping sleeve mechanism was employed in [5] to have the strut active only during positive g maneuvers. For negative g maneuvers, the wing acts like a cantilever wing, rendering the strut buckling constraint unnecessary.

2.2 Multidisciplinary Design Optimization (MDO)

Multidisciplinary Design Optimization is a field of research that studies the application of numerical optimization methods to the design of engineering systems involving multiple disciplines. It allows to incorporate all the relevant disciplines simultaneously obtaining the most desirable trade-off between them. There are many MDO application fields such as aerospace and automobile design, naval architecture, electronics, architecture, computers and electricity distribution. However, the largest number of applications have been in the field of aerospace engineering [45]. This thesis uses the MDO applied to the aircraft design results.

2.2.1 MDO applied to aircraft design

Between 1970 and 1990 the aircraft design changed the approach of the design problems due to the development of computer-aided design and the changes in the procurement policy of most airlines and military organizations from a performance-centered approach to one that emphasized lifecycle cost issues [46]. During this period, it began the application and development of MDO. “Designing the wing involved literally thousands of decisions that could add up to an invaluable asset, a proprietary store of knowledge. A competitor could look at the wing, measure it even, and make a good guess about its internal structure. But a wing has as many invisible tricks built into its shape as a Savile Row suit; you would need to tear it apart and study every strand to figure out its secrets.” (Irving, 1993) [47]

The “thousands of decisions and invisible tricks” that involve wing modeling and design requires the use of MDO due to the analysis and design of aerodynamics, structures and performance being coupled. To optimize aerodynamics and structures, it must be considered the effect of the aerodynamic shape variables and structural sizing variables on the weight, which affects the fuel consumption. The solution of this problem comes from numerical optimization which is a powerful tool that can perform automatically all these trade-offs [14, 15].

In 2013, Martins and Lambe [48] summarized the existing literature in MDO architectures. Two main methodological approaches were established, monolithic and distributed architectures. Monolithic MDO architectures solve a single optimization problem, while distributed architectures solve optimization subproblems for each discipline and a system-level optimization problem. Distributed architectures increase the system flexibility and responsiveness but unless a problem has a special structure, there is no distributed architecture that converges as rapidly as a monolithic one [46].

2.2.2 Multi-fidelity in MDO

Fidelity is defined as the validity and reliability of the entire MDO process and optimization results. The fidelity of multidisciplinary systems, such as those used for aircraft design, depends on the fidelity of each discipline and the complexity of the optimization process. The multi-fidelity calculation method combines low and high-fidelity discipline codes [12]. The purpose is to provide a way to minimize the usage of high-fidelity models to reduce overall computational cost [11].

Furthermore, multi-fidelity optimization approaches seek to bring higher-fidelity models earlier into the design process by using estimations from lower-fidelity models to accelerate convergence of the design problem [22]. The conceptual design phase begins with low fidelity calculations, which can be used in an optimization environment. Once this phase is completed, the preliminary design can start by recurring to medium fidelity models [12].

Considering two different fidelity methods to solve the same problem, the higher-fidelity method can

provide more valuable insights to designers of complex systems. On the one hand, high-fidelity methods require longer calculation times and more computational resources than low-fidelity ones, which is frequently over the design budget [12, 22]. High-fidelity models include the compressible Euler/Navier-Stokes equations and structural finite element methods [19]. The low-fidelity methods are less accurate than the high-fidelity ones, but their computational efficiency is much higher. If both methods are used, i.e. using a multi-fidelity calculation method, the poor accuracy of the low-fidelity can be improved and the high-fidelity computational cost can be significantly reduced [12].

The high computational cost mentioned previously, in addition to the high-dimensional spaces (which is usually the case of an aircraft design problem) and the use of costly high-fidelity solvers to accurately simulate the coupled multiphysics system, renders high-fidelity methods very challenging to be used for design optimization [23, 24]. In [24], they combine multi-fidelity Gaussian process regression and Bayesian optimization to construct probabilistic surrogate models and explore high-dimensional design spaces in a cost-effective manner.

Due to all the advantages of using high-fidelity methods, the field of multidisciplinary optimization has experienced great developments and progress over the last two decades to support the solving of complex design problems. In addition, the rapid improvement of computer resources during recent years has helped to overcome the expensive computational cost of using the high-fidelity analyses [23, 24].

Multi-fidelity optimization models have already been used in aeronautical engineering [24]. Typically, conceptual aircraft design optimization is based on semi-empirical equations that were well-established at the beginning of aircraft design [23]. In [13], they performed a shape optimization analysis constructing a hierarchical multi-fidelity response surface efficiently combining a linear panel method with an Euler solver. Additionally, multi-fidelity design strategies were used in [49] to combine conceptual and preliminary designs for a high-speed civil transport wing optimization. A multi-fidelity method commonly used is the polynomial fitting method developed in [50, 51]. The polynomial interpolation was used to fit the high-fidelity data with the low-fidelity data, but the error has shown to be large. Co-Kriging method [52] can be used to construct a multi-fidelity surrogate model with both low and high-fidelity data. Its accuracy has been validated using aerodynamic calculations in [53, 54]. Furthermore, an extended Co-Kriging method with higher accuracy has been recently developed in [55].

The aeroelastic behavior of adaptive wings, with compliant airfoils has been studied with Fluid-Structure Interaction (FSI) investigation and optimization [56, 57]. FSI is the multiphysics study on how fluids and structures interact. The fluid flow may exert pressure and/or thermal loads on the structure which cause structural deformation. FSI problems can be solved with high-fidelity CFD models [58]. Some applications of metamodeling-based methods involve wing design [59] and aeronautical applications [60, 61]. It also has been studied a coupled aero-structural wing shape design by using Reynolds-Averaged Navier–Stokes (RANS) solver for aerodynamics and NASTRAN for structures and

aeroelasticity [20], which are high-fidelity simulation tools. The study concluded that the Euler/RANS solver was still be too expensive for the real-world design environment.

2.2.3 MDO for aero-structures and aeroelasticity problems

The integrated aerodynamic/structural design optimization has been widely investigated during the last 30 years. This optimization is necessary to get the optimum wing since aerodynamic loads affect the structural deformations, which in turn change the aerodynamic shape [21].

Previous studies on multilevel techniques for practical aeronautical applications have been made, such as in [62]. Many aeroelastic studies have been carried out such as [63–65]. In [63], it is presented a differentiated unsteady aeroelastic analysis module suitable for large scale MDO problems which are typical in the preliminary aircraft design. In [64], it is performed a flutter analysis of a slender wing in compressible flow using state-space representation of the unsteady aerodynamic behavior. Within MDO, a comparative sensitivity study for the bending–torsion flutter instability of flexible aircraft wings in subsonic flow has been presented in [65].

An improvement is achieved when the subsystems are developed in parallel under a multidisciplinary formulation [66], which is demonstrated in [67] where the objective was to improve the overall efficiency of aero-structural optimization, by simplifying the system-level problem, and thereby reducing the number of calls to a potentially costly aerodynamics solver. Traditional coupled aero-structural design optimization [16–18] of aircraft based on high-fidelity models is computationally expensive and inefficient. Nowadays, the aim of aero-structural design optimization is to reduce computational cost and speed up the optimization procedure [21]. To improve the efficiency, the key is to predict aero-structural performance of the aircraft [19]. Some researchers developed effective optimization frameworks based on genetic algorithm and all kinds of surrogate models [68–72] for aerodynamic/structural design optimization. Multi-fidelity methods are not only applied within a surrogate based optimization framework but also can be successfully integrated in gradient-based methodologies which are more computationally efficient [19]. Some applications of surrogate modelling and multi-fidelity techniques can be found in [73–75].

Gradient-based algorithms use gradients of both the objective and constraint functions with respect to the design variables [76]. This is accomplished either by finite differences or the adjoint method. The latter is typically more computationally efficient, where the expense is independent of the number of design variables [19]. The convergence of the adjoint equations needs to be improved greatly [77] before it is widely used in aero-structural design optimization due to its complexity [19].

The most popular aero-structural prediction method is the loosely coupled aeroelastic analysis for its simplicity. It solves first the aerodynamic problem and then the structural problem. It repeats the full

cycle until the deformation of the wing converges. Usually, it needs at least five iterations of repeated full-cycle aerodynamic/structural analysis, which is very time-consuming and inefficient. Another prediction method, which is rarely found in commercial software packages due its complex implementation, is the tightly coupled method. Contrary to the loosely coupled method, this one is a very efficient method where system consists of a structure and flow subproblems, and they are successively solved at each time step [19].

Traditional coupled multi-disciplinary design optimization based on computational fluid dynamics/ computational structure dynamics (CFD/CSD) aims to optimize the jig shape of aircraft [21]. Many algorithms, such as Infinite-Plate Spline (IPS), Boundary Element Method (BEM), Constant-Volume Tetrahedron (CVT) and Radial Basis Functions (RBF), have been developed to transfer data between CFD and CSD models [78–80].

The jig shape is the aircraft shape that does not undergo aerodynamic load, gravity, and propulsive forces. At cruise conditions, it deforms into cruise shape due to the applied forces [19]. There is a methodology named reverse iteration of structural model (RISM) proposed in [21], where it is used to get the aero-structural performance in cruise directly due to the fact that the cruise shape can be transformed into jig shape. The main advantage of RISM is that the efficiency can be improved by at least four times when compared with loosely coupled aeroelastic analysis, maintaining almost the same fidelity of the loosely coupled aeroelastic analysis [21]. In [19], RISM methodology is used but the computation has been done in graphical processing units (GPGPU) to accelerate the RISM and construct a GPU-accelerated RISM whose efficiency can be raised about 239 times compared with the one of the loosely coupled aeroelastic analysis.

Aly, in [81], proposed a decoupled approach of aero-structural design optimization to avoid the repeated aerodynamic/structural analyses during CFD/CSD analysis. Unfortunately, Aly's methodology does not lead to the true optimal solution of aero-structural design optimization due to optimizations are conducted sequentially [21]. In [82], the jig shape correction is applied to get the structural performance of the aircraft using Aly's methodology to get the initial jig shape.

2.3 MDO in SBW

In the 80's, the applications of MDO began in aircraft wing design [83–85]. These papers show that aerodynamics, structures, and controls are strongly coupled. In addition, research about a high aspect-ratio (AR) SBW was conducted in Hampton Technical Center [37], where they did a study to determine if this proposal had performance improvements in cruise range when compared to a baseline concept. The results of the study indicated that an optimum SBW configuration with AR of 28 has a 31% improvement when compared to a baseline concept with a wing AR of 10.

In the 90's, the use of MDO has been documented in some papers such as Sobieski and Haftka [86] and Kroo [87]. In addition, Virginia Tech applied MDO to the design of a High-Speed Civil Transport in [49, 88, 89] and compared a SBW configuration to the cantilever one in [7]. The analysis demonstrated that the greatest virtues of the SBW are the improvement in fuel consumption and a smaller engine size, which means that the SBW would cost less, limit pollutant emissions and reduce noise pollution in urban airports.

Recently, more MDO in SBW configuration analysis has been made. In Von Karman Institute for Fluid Dynamics [15] they have presented a framework for aerodynamic and aero-structural design optimization of aircraft wings. The methods used successfully tackled the compounding challenges of modeling the wing with high fidelity, while optimizing it with respect to hundreds of design variables. On the other hand, SBW with high AR has also been investigated. ONERA in the ALBATROS project [9] has conducted research activities on the SBW transport aircraft configuration. The investigation showed that the SBW configuration allows to increase significantly the wing aspect ratio, reduce the wing sweep angle and profile thickness in order to achieve laminar flow on a large part of the wing surface. The results in terms of structural design showed that the SBW allows to keep a relatively light wing primary structure despite the significant aspect ratio increase and the limited wing box thickness.

Chapter 3

Problem description

3.1 Description of structure and load cases

A previously optimized structure from a Low-Fidelity structural model based Fluid-Structure Interaction analysis for a Strut-Braced Wing configuration under a cruise and pull-up maneuver loads is going to be used to perform the optimizations. The geometrical dimensions of the model are detailed in Table 3.1.

General geometry	
Area [m^2]	66.6
Aspect Ratio [-]	21.2
Span [m]	37.5
Mean chord [m]	1.95
Taper ratio [-]	0.275
Sweep [deg]	13.7
Strut Position [$\%$]	60

Table 3.1: Model geometrical dimensions

A brief overview of the aircraft main wing components is provided below. It is based on the textbook by Megson [90], followed by the material composition and properties used in this work.

The aircraft structure aims at transmitting and resisting the applied loads, providing an aerodynamic shape and protecting passengers and payload from the environmental conditions encountered in flight. The main components of an aircraft wing are illustrated in Figure 3.1. Their functions are explained below [90, 91]:

- Skin: resists distributed and concentrated loads, such as aerodynamic pressure and undercarriage loads. Also, it redistributes stress around discontinuities. Although the thin skin is efficient in resisting shear and tensile loads, it buckles under low compressive loads. Rather than increasing the skin thickness and suffering a consequent weight penalty, stringers and ribs are attached to the skin to increase the buckling load and failing stresses.

- Ribs: increase the buckling load of the skin panels and help to maintain the airfoil shape. The dimensions of the ribs are given by the loads they are required to support. For instance, closer to the wing root, the ribs must absorb and transmit large concentrated loads, such as the ones transmitted from the undercarriage.
- Stringers: divide the skin into small panels which increase the buckling load and failing stresses without requiring the skin thickness to be increased. They are attached to the skin and to the ribs.
- Spar webs: develop shear stresses to resist both shear and torsion loads. Together with the skin, they also perform the function of stabilizing the spar flanges which resist the compressive forces arising from axial loads and bending effects.

It should be noted that the basic principles and components of wing structures described previously apply to all aerodynamic surfaces, such as horizontal and vertical tails, all control surfaces and the strut in the case of SBW configuration. The Figure 3.1 exemplifies the structural components of a main wing and an empennage.

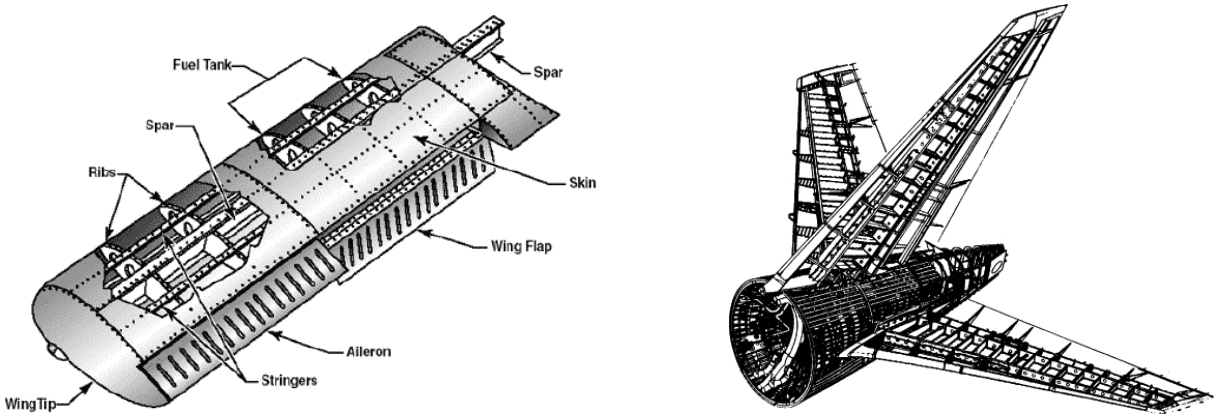

(a) Main wing components [91]

(b) Structural components of the empennage [92]

Figure 3.1: Aircraft structural components

The airframe of an aircraft includes the fuselage, undercarriage, empennage and wings. It is usually made of a combination of different materials such as aluminium alloys, titanium and composite materials. Nowadays, the manufacture with composite materials is increasing but up to now its major component was aluminium with 80% of its structure weight made of it [93]. To simplify this case study, it is going to be considered that the wing and the strut are made of an aluminium alloy since it is still the material most used.

The wing and strut structures need a material that has great resistance to support flight loads and fatigue, as well as good machinability. However, resistance to high temperatures is not as important as in the engines. As a result, among the large amount of aluminium alloys, aircraft manufacturers use high-strength alloys, such as 7075 which is commonly known as Zicral [94]. The composition and the properties of it are shown in Table 3.3 and 3.2. As it can be deduced from the yield stresses shown in

Table 3.3, the safety factor used in the analysis is 1.5.

Properties aluminium 7075	
Density [kg/m^3]	2800
Young Modulus [GPa]	72
Poisson Coefficient [-]	0.33
Yield stress [MPa]	400
Yield stress with safety factor [MPa]	266

Table 3.2: Aluminium 7075 (Zicral) properties

Composition aluminium 7075	
Aluminium [%]	89.3 – 91.6
Zinc [%]	5.1 – 6.1
Magnesium [%]	2.1 – 2.5
Copper [%]	1.2 – 1.6
Silicon, iron, manganese, titanium, chromium and other metals [%]	0 – 0.5

Table 3.3: Aluminium 7075 (Zicral) composition

The structure modelled for the analysis of this case study has been simplified to a wing box whose skin is aligned with the airfoil shape. The wing box starts at a given percentual chord distance behind the leading edge ($x_{WB,s}$) and ends at a prescribed percentual chord distance after the leading edge ($x_{WB,e}$) as shown in Figure 3.2. The upper and lower surfaces simulate the skin of the structure and the side surfaces simulate the spars of the structure.

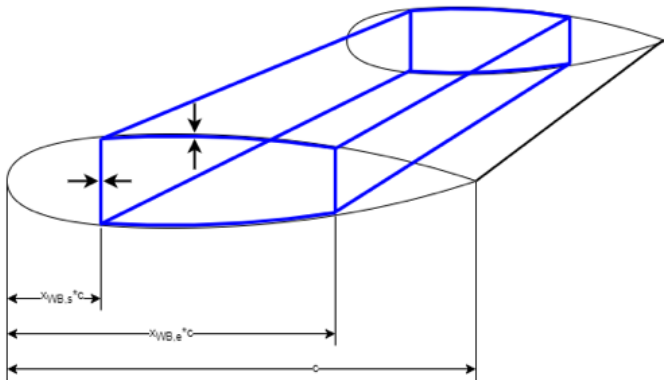

Figure 3.2: Wing box sketch

The main wing has an imposed external twist distribution, which is bilinear along the span. However, the strut has no twist. In addition, the thickness distribution along the wingspan has two linear distributions. One between the wing root and the joint connecting the main wing and the strut, and another one between the joint mentioned previously and the wing tip. The strut thickness distribution is linear around the wing-strut joint, constant from the joint until a given percentual length of it and linear at the

strut-fairing joint. Lastly, the fairing thickness distribution is constant.

The skin and spar areas have different thickness values. The values of the thickness distribution for the main wing, strut and fairing for the Baseline case study are plotted and detailed in Figure 3.3 and Table 3.4, respectively. In Chapter 4, these values are going to be optimized for the case study described previously in Table 3.5. It should be noted that the fairing is represented in the plot as the first part of the strut, from 0 to 1 meter approximately.

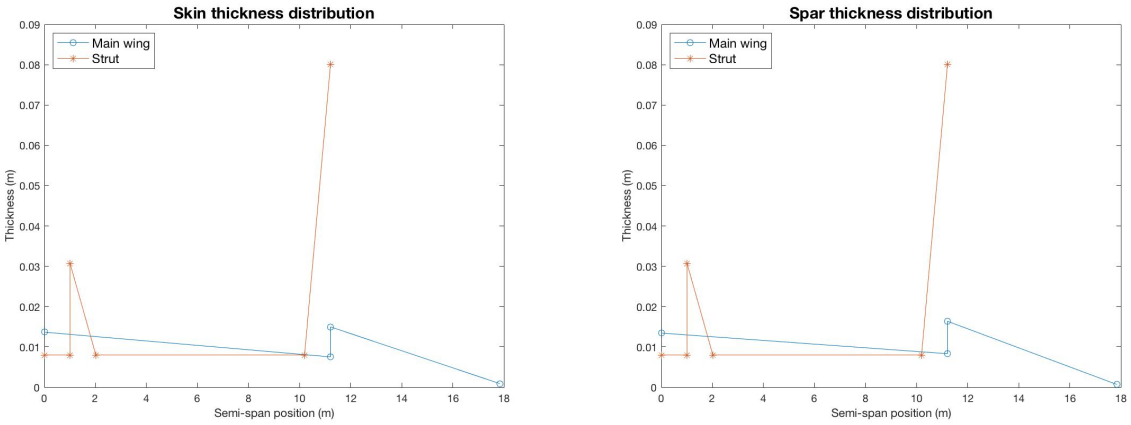

(a) Skin thickness distribution

(b) Spar thickness distribution

Figure 3.3: Thickness distribution of the Baseline case study

Variables		Value
Skin thickness	root $[mm]$	13.67
	joint inboard $[mm]$	7.54
	joint outboard $[mm]$	14.98
	tip $[mm]$	0.92
Spar thickness	root $[mm]$	13.44
	joint inboard $[mm]$	8.32
	joint outboard $[mm]$	16.34
	tip $[mm]$	0.71
Strut thickness	@joint $[mm]$	80.06
	main $[mm]$	8.01
	@fairing $[mm]$	30.72
Kink position strut	@joint $[\%]$	10.0
	@fairing $[\%]$	90.6

Table 3.4: Values of the Baseline case study optimization variables

Due to symmetry, only one half of the aircraft is going to be modeled and analyzed.

The case study for which the thickness and its distribution are going to be optimized has two load cases, cruise and pull-up maneuver. The Baseline configuration is the one that loads the structure with the pull-up maneuver load. As it is going to be further detailed in the Chapter 4, the deformation obtained

by the High-Fidelity model has to match the deformation of the Low-Fidelity one in the cruise load case. Additionally, the structure has to support a pull-up maneuver load case. The specifications of the aircraft and the conditions at cruise and pull-up maneuver are detailed in Table 3.5.

	Aircraft data	
Maximum Take Off Mass (MTOM) [kg]	30938.83	
Structural mass [kg]	3272	
	Cruise	Pull-up Maneuver
Load factor [-]	1g	2.55g
Angle of attack [deg]	2.5	3.4
Altitude [m]	10668	7620
Air density [kg/m^3]	0.3805	0.5489
Airspeed [m/s]	225.367	235.349
Mach number [-]	0.76	0.76

Table 3.5: Case study data

The loads, which are further detailed in Section 3.5, for the cruise and pull-up maneuver are obtained from an Aerodynamic Force distribution and its points of application. The Boundary Condition set in the model is the restriction of all the degrees of freedom of the nodes located on the wing root, i.e. *y = 0* of the global coordinate system.

3.2 Computational tools

The main computational tool used throughout this project to model and parametrize the geometry is Ansys Parametric Design Language (APDL). Ansys is an engineering simulation software for product design, testing and operation. Ansys Mechanical Finite Element Analysis software is used to simulate computer models of structures, electronics or machine components for analyzing strength, toughness, elasticity and other attributes. APDL is the foundation for all sophisticated features, many of which are not exposed in the Workbench Mechanical user interface. It also offers many conveniences such as parameterization, macros, branching and looping and complex math operations. All these benefits are accessible within the Ansys Mechanical APDL user interface [95].

In addition to ANSYS, the software Matlab has been used in the modeling process to create some of the keypoints added in the APDL code. For instance, given the airfoils and the twist distribution of the main wing, the points of the airfoils have been rotated and translated in Matlab and then, the main wing has been modelled in Ansys using the transformed points.

The computational tool used in the optimization process is Matlab. More specifically, the nonlinear programming solvers *fmincon* and *fminunc* provided by Matlab's Optimization Toolbox. *fmincon* and *fmi-*

nunc are solvers that find a constrained and unconstrained minimum, respectively, of a scalar function of several design variables starting at an initial estimate. They have several algorithm options that are detailed in the Chapter 4. The inputs that have to be specified to use these optimization tools are: the function to be optimized; the starting point which in this case study is the baseline case whose values are detailed in Table 3.4; the constraints; and bounds which are both detailed in the Chapter 4. These last two are not required by the *fminunc* solver due to the fact that as its name suggests, it solves unconstrained problems. The outputs given are the design variables optimized and some data structures that contain information about the optimization process such as the number of iterations performed and the stopping criteria.

3.3 Geometry modelling methodology in Ansys

The geometry modelling has been performed creating firstly an APDL code and then running it in Ansys Mechanical. Before creating the APDL code it has been necessary to rotate and translate the airfoils points. Once all the points are located properly, the strut, main wing and fairing can be modeled. As it has been mentioned and showed previously in Figure 3.2, the geometry has been simplified to a wing box like structure. For that purpose, it has been necessary to select with a Matlab code the points that make the wing box.

The steps followed to model the strut, main wing and fairing, once all the keypoints coordinates have been obtained, are enumerated next:

1. Definition and identification of the geometry points.
2. Creation of the lines to link the airfoil points by splines in the areas of the upper and lower surfaces and by straight lines in the points that link both surfaces.
3. Creation of the areas selecting the previous lines. Each section between airfoil has four areas: upper and lower that simulate the skin of the structure, and front and back that simulate the spars of the structure.
4. Definition of the thickness distributions in APDL language and creation of the sections associated to each thickness distribution.

After modelling the geometry in Ansys, which is shown in Figure 3.4, the load and the constraints have to be defined. As it has been mentioned previously, the loads applied in this case study are a high load maneuver of 2.55g and a cruise load whose distributions have also been used in the Low-Fidelity study. The loads are described in more detail in Section 3.5. All the degrees of freedom of the points that are located at $y = 0$, which are the points located in the symmetry plane of the whole aircraft, are constrained.

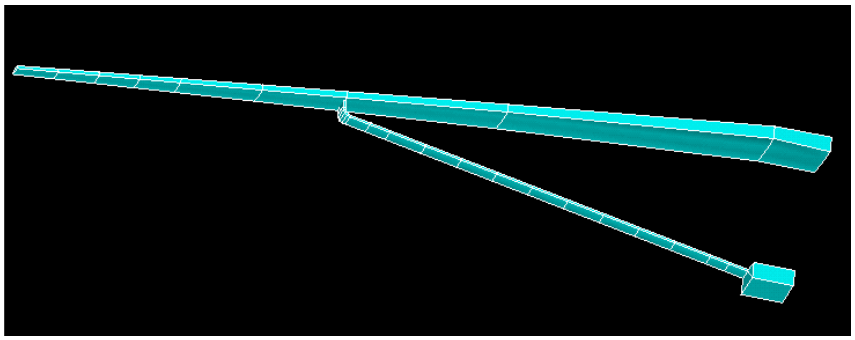

Figure 3.4: ANSYS Structural model

3.4 Finite elements

Two type of elements from the Ansys APDL element library are used to build the finite element model: SHELL181 and MPC184. The shell elements are used to model the skin and spars of the structure and the MPC elements are used to model the ribs distributed along the structure. A brief overview of the SHELL and MPC elements is provided below, which is based on the ANSYS Mechanical APDL Element Reference [96].

Generally, shell elements are used to analyze thin to moderately-thick structures, where one dimension is much smaller than the other two dimensions. Since they decouple the deformation on the surface and the deformation in the normal direction, the structure simulation is simplest and efficient. The shell elements are created by associating them with some data displayed in APDL tables to represent the thickness along the model and the material properties.

SHELL181 is a four-node element with six degrees of freedom at each node: x,y,z translations and rotations about the x,y,z axes. It is well-suited for linear applications, which are the type of analyses performed along this project, in addition to large rotation and large strain nonlinear applications. The element formulation is based on logarithmic strain and true stress measures and the element kinematics allow for finite membrane strains. However, the curvature changes within a time increment are assumed to be small.

MPC184 elements comprises a general class of multipoint constraint elements that apply kinematic constraints between nodes. They are divided in two type of elements: constraint elements and joint elements. It has been selected the MPC184-rigid beam, which is inside the constraint elements group and it is a rigid beam with two nodes and six degrees of freedom at each node. Since the aim of these elements is to model the structural ribs which are a rigid part of the structure, all the degrees of freedom should be constrained. Because this type of element models a rigid constraint, material stiffness properties are not required. As well as the SHELL181 elements, this type of element is well suited for linear, large rotation and large strain nonlinear applications. The kinematic constraints are imposed using the direct elimination method, wherein the kinematic constraints are imposed by internally generated multi-

point constraint (MPC) equations.

The Low-Fidelity model is a beam model. The reason of getting the deformation at the beam nodes is that the Low-Fidelity model provides its results there so, as the results of the High and Low-Fidelity models are going to be compared in Section 4.5, it is necessary to obtain the results of the design parameters at these nodes.

Usually, the MPC184-rigid beam element can be used to model a rigid constraint between two deformable bodies, which in this work the bodies linked are the skin/spars with the ribs, or as a rigid component used to transmit forces and moments in engineering applications. The link between both elements has been made linking nodes, the ones from the shell elements which are around each beam node together with each beam node itself. Therefore, the motion of the shell elements is transmitted to the MPC elements which allows the movement of the ribs together with the skin and spars. In addition, linking them together also allows to get the deformation at the beam nodes that are located in the middle of the ribs.

3.5 Loads

Initially, the load data for the maneuver and cruise cases was given by distributed forces files which came from a 3D Panel Method code. Both distributed loads applied to the deformed structure are shown in Figures 3.5 and 3.6. Both pictures show two apparent steps in the load distribution between the strut joint and the tip of the main wing. The steps in the load are due to this part of the wing has a denser mesh so, as a result, this part of the wing has more elements per area that allow to have the load more distributed, being lower the load in each strip.

After checking the large amount of time required to run a single simulation, it has been necessary to reduce the size of the load files to accelerate the computations. Due to the computational cost needed, using the distributed forces files makes the optimization process unfeasible. The new condensed load files contain the load information on the beam nodes used in the Low-Fidelity structural model.

To check if the results obtained with these new load files are reliable and accurate, it has been performed the verification of the condensed forces comparing the loads applied and reactions obtained when loading the structural model with both load files: the condensed and the distributed one. The comparison of the results applying the distributed and condensed files can be found below in Section 4.4.2. The results of the reactions for both load files and load cases are shown in Table 3.6.

It can be seen in Table 3.6 that in both cases, cruise and maneuver, the load reactions F_x, F_y and F_z are exactly the same in both load files. In addition to the load reactions, Ansys shows the moments

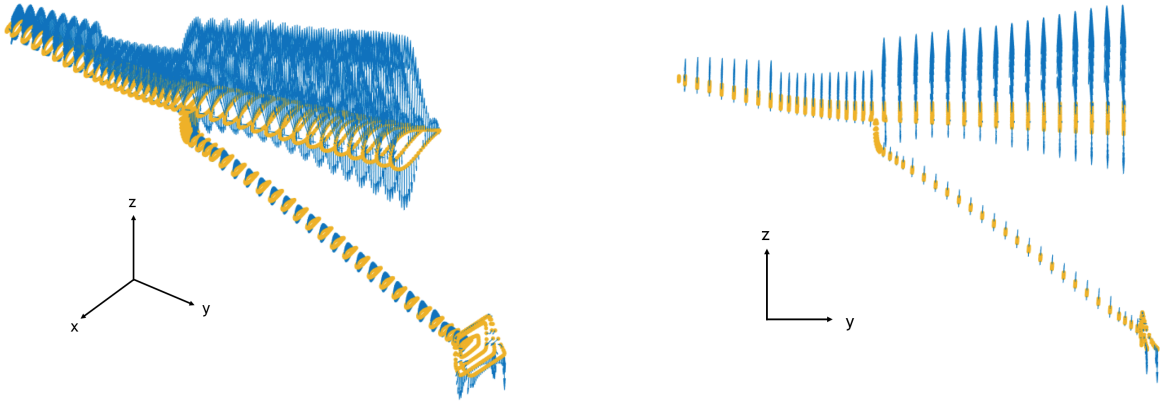

(a) Isometric view (b) Front view

Figure 3.5: Cruise load

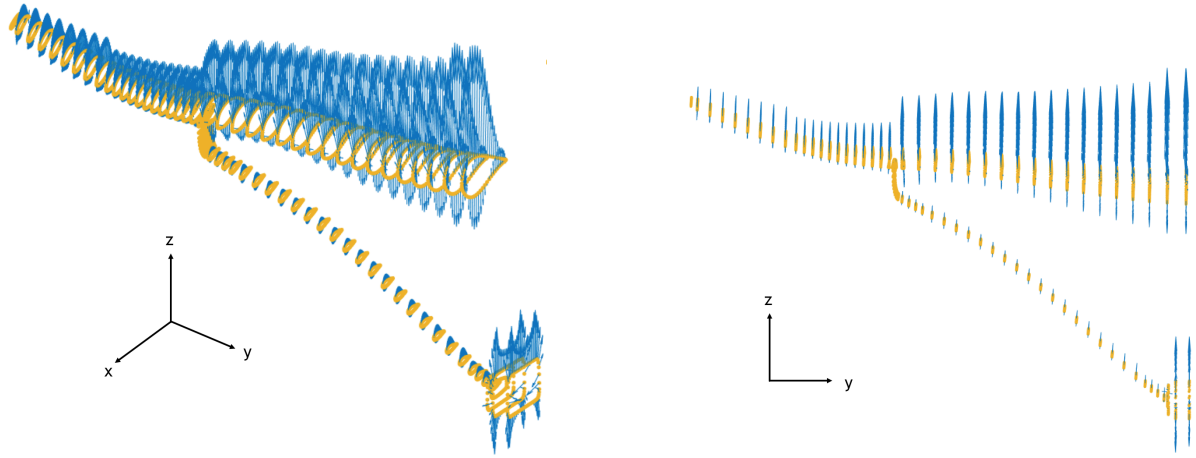

(a) Isometric view (b) Front view

Figure 3.6: Maneuver load

Reactions		Cruise	Maneuver
Distributed loads	Fx $[N]$	-3241.4	-8989.3
	Fy $[N]$	1695.3	8830.9
	Fz $[N]$	136690	374530
Condensed loads	Fx $[N]$	-3241.4	-8989.3
	Fy $[N]$	1695.3	8830.9
	Fz $[N]$	136690	374530
Distributed moments	Mx $[Nm]$	-15419	-37515
	My $[Nm]$	-2740.7	-6761.7
	Mz $[Nm]$	3181.3	6447.7
Condensed moments	Mx $[Nm]$	-14990	-48201
	My $[Nm]$	-2875.8	-8751.1
	Mz $[Nm]$	3215.5	6503.7

Table 3.6: Reactions values of the distributed and condensed forces and moments

Error cruise [%]		Error maneuver [%]	
Fx	0	Fx	0
Fy	0	Fy	0
Fz	0	Fz	0
Mx	2.78	Mx	28.48
My	4.93	My	29.42
Mz	1.08	Mz	0.87

Table 3.7: Differences between the distributed and condensed forces and moments

reactions, M_x, M_y and M_z. As a result of applying the loads in different structural nodes which are moving when the load is applied, the moment reactions cannot be compared directly. That is the reason why the moments are different. As a result of deformation, when Ansys calculates the reactions the structure is already deformed.

It can be concluded that, as there are no significant differences in all the reactions, the condensed load files can be used for the whole analysis. Otherwise, the computational cost would be prohibitive.

3.6 Mesh

To ensure that the results obtained from the Ansys simulation are adequate it is necessary to do a mesh convergence study which consists on simulating the same problem with finer meshes and compare the results. It is said that the mesh has converged when a finer mesh provides a negligible change in the numerical solution [97]. The problem chosen for the mesh study has the same parameters as the Baseline configuration, but different load for speeding up the mesh convergence study, since running both load cases requires a large computational time. The load used is a point load of 3000 N upwards in the vertical direction and it has been located at the tip of the main wing.

Mesh refinement must be a trade-off between the accuracy of the numerical solution and the computational cost. If the mesh is too fine, the computational resources to evaluate the model will be prohibitive but if the mesh is too coarse, the numerical solution provided by the model will be inaccurate.

Generally, it is not required the same size of element in the whole model since not all the areas have the same stress gradients [97]. To obtain a better trade-off between the accuracy of the numerical solution and the computational cost a fine mesh should be used in the areas of high stress gradients and a coarser mesh where the stress gradients are small. Thus, the areas near the main wing root should have lower element sizes due to these areas are the ones that support the higher stresses. The mesh in the root is shown in Figure 3.7.

The element size has been controlled assigning the number of elements per area. For the mesh

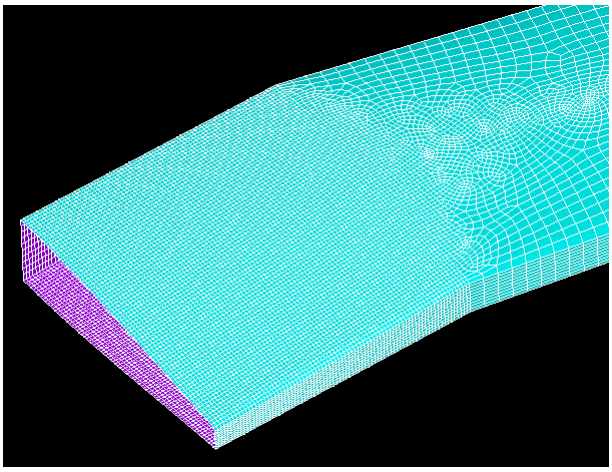

Figure 3.7: Mesh refinement at the root

convergence study, the number of elements has been increased, differently in each area because they have large differences in size. For instance, the spar areas are smaller than the skin areas, that is the reason why the number of elements in one skin area is going to have a larger increase than the spar area in the next mesh. The total number of elements for each mesh is detailed in Table 3.8.

It is important to ensure the quality of the mesh which can be assessed by different metrics that are usually based upon the geometrical properties of the mesh cells, such as the aspect ratio, or upon the relation between neighboring cells. In the whole mesh convergence study, it has been verified that the aspect ratio of the elements is adequate in all the model areas. The suitability of a mesh for a simulation is also strongly influenced by the simulated physics, the simulation solver, and the geometrical domain. The quality metrics can give an indication if a mesh is a good fit for a simulation setup [98].

This work considers that the mesh has converged when the difference between results obtained by finer meshes are lower than 1%. The mesh convergence study performed is shown in Tables 3.8 and 3.9. The results used to compare the meshes in the convergence study are vertical displacements in two structural nodes, structural mass, maximum stress and maximum strain energy. Only the vertical displacement is compared since from the three displacements (x,y,z) it is the one with the highest magnitude. The nodes selected to compare the vertical displacements are the ones located at the tip of the main wing (node 16) and at the main wing-strut joint (node 5).

In Table 3.8 it can be seen that even though the displacements reach the convergence criterion in the second mesh, the maximum stress and the maximum strain energy of the structure have higher variations and do not reach the convergence until the mesh number 14 and 15, respectively. The reason is that sometimes the displacement at one point of the structure is nearly constant, but the structure is still deforming differently giving a different value of the strain energy, thus a finer mesh is required to predict accurate results. Hence, the strain energy is the parameter that assures that the mesh has converged. It has been used the relative error with respect to the finest mesh, mesh number 17 in Table

3.9, to be able to compare the results between meshes. The relative error is given by the following formula:

$$\text{Relative error} = \frac{\text{Absolute error}}{\text{Real value}} = \frac{\text{Mesh N - Mesh 17}}{\text{Mesh 17}} \tag{3.1}$$

where N is the number of the mesh. In Figure 3.8 the relative errors of the maximum stress and maximum strain energy with respect to the finest mesh are plotted as a function of the number of elements. It can be seen that the curve plotted is not smooth and has two points where the stress and strain energy relative error is higher than the coarser mesh. These two points have higher relative error because, even though both meshes are finer than the previous one, the points where the Ansys compute the parameters are different due to fact that the meshes have changed. Given the fact that the computational cost is an issue in the simulations and that Ansys has a limitation of 125000 mesh elements, it has been decided to reduce the number of elements in the areas that do not show high stresses, such as the joint between the strut and the fairing, to be able to increase it in the areas of interest, which are the skin and spar areas of the main wing. That is the reason why the mesh number 14 has higher number of elements than the mesh number 15, which is finer than the previous one, but has lower relative error with respect to the finest mesh which is the mesh number 17 of the Table 3.9.

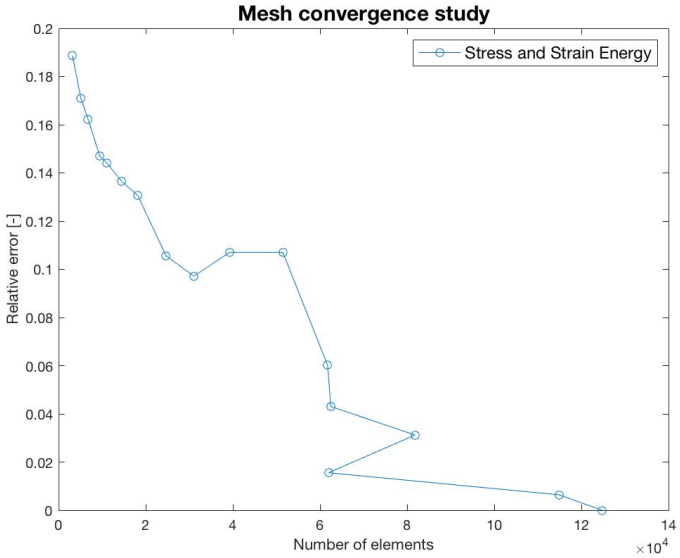

Figure 3.8: Stress and strain energy relative errors respect to the finer mesh

From the mesh convergence study it is concluded that the first mesh that reaches the convergence criteria in all the parameters with the lowest computational cost is the mesh number 15. For this reason, the mesh number 15 is the one used in the simulations of this project.

Mesh	Vertical displacement node 5 [mm]	Error [$\%$]	Vertical displacement node 16 [mm]	Error [$\%$]	Number of elements
Mesh 1	-4.856E-03	2.783	-1.668E-01	1.526	3190
Mesh 2	-4.725E-03	0.126	-1.642E-01	0.295	5136
Mesh 3	-4.719E-03	0.154	-1.638E-01	0.354	6767
Mesh 4	-4.711E-03	0.036	-1.632E-01	0.638	9475
Mesh 5	-4.710E-03	0.104	-1.642E-01	0.951	11111
Mesh 6	-4.705E-03	0.058	-1.627E-01	0.298	14469
Mesh 7	-4.702E-03	0.044	-1.632E-01	0.487	18187
Mesh 8	-4.700E-03	0.048	-1.624E-01	0.106	24665
Mesh 9	-4.698E-03	0.152	-1.622E-01	0.028	31081
Mesh 10	-4.705E-03	0.019	-1.622E-01	0.0001	39243
Mesh 11	-4.704E-03	0.045	-1.622E-01	0.052	51473
Mesh 12	-4.702E-03	0.087	-1.621E-01	0.053	61743
Mesh 13	-4.706E-03	0.048	-1.620E-01	0.088	62496
Mesh 14	-4.704E-03	0.033	-1.618E-01	0.012	81823
Mesh 15	-4.702E-03	0.013	-1.618E-01	0.0001	61970
Mesh 16	-4.702E-03	0.004	-1.618E-01	0.014	114908
Mesh 17	-4.701E-03	-	-1.618E-01	-	124710

Table 3.8: Mesh convergence study: displacements and number of elements

Mesh	Maximum stress of the structure [Pa]	Error [$\%$]	Maximum strain energy of the structure [J]	Error [$\%$]	Structural mass	Error [$\%$]
Mesh 1	8.338E+07	2.137	1.158E-03	2.137	1.885E+03	0.023
Mesh 2	8.520E+07	1.030	1.183E-03	1.030	1.886E+03	0.003
Mesh 3	8.609E+07	1.808	1.196E-03	1.808	1.886E+03	0.006
Mesh 4	8.767E+07	0.329	1.218E-03	0.329	1.886E+03	0.003
Mesh 5	8.796E+07	0.872	1.222E-03	0.872	1.886E+03	0.008
Mesh 6	8.873E+07	0.684	1.232E-03	0.684	1.886E+03	0.007
Mesh 7	8.934E+07	2.792	1.241E-03	2.792	1.886E+03	0.006
Mesh 8	9.191E+07	0.935	1.277E-03	0.935	1.886E+03	0.005
Mesh 9	9.278E+07	1.107	1.289E-03	1.107	1.886E+03	0.009
Mesh 10	9.176E+07	4.982	1.274E-03	4.982	1.886E+03	0.009
Mesh 11	9.657E+07	1.793	1.341E-03	1.793	1.886E+03	0.004
Mesh 12	9.834E+07	1.222	1.366E-03	1.222	1.886E+03	0.004
Mesh 13	9.955E+07	1.590	1.383E-03	1.590	1.886E+03	0.005
Mesh 14	1.012E+08	0.922	1.405E-03	0.922	1.886E+03	0.004
Mesh 15	1.021E+08	0.213	1.418E-03	0.213	1.886E+03	0.002
Mesh 16	1.023E+08	0.429	1.421E-03	0.429	1.887E+03	0.001
Mesh 17	1.028E+08	-	1.427E-03	-	1.887E+03	-

Table 3.9: Mesh convergence study: stress, strain energy and structural mass

3.7 Nonlinear analysis

Nowadays, the computational power and the concurrent advances in numerical simulation have made possible to perform nonlinear analyses and better designs. Numerical simulation, based on finite element methods, plays an indispensable role in the manufacturing process, improving quality and performance while reducing developing times. It has been used as an acceptable mean of model validation and it has replaced the traditional build-and-break prototyping. For instance, as it has been mentioned

previously, the High-Fidelity model analyzed in this work is used to validate a Low-Fidelity model [99].

On the one hand, a linear static analysis is an analysis where a linear relation holds between applied forces and displacements. In structural problems, a linear analysis is applicable when the stresses remain in the linear elastic range of the used material and the deformations are relatively small. In this case, the model's stiffness matrix is constant, and the solving process is relatively short compared to a nonlinear analysis on the same model. Therefore, for a first estimate, the linear static analysis is often used prior to performing a full nonlinear analysis [100].

On the other hand, a nonlinear analysis is an analysis where a nonlinear relation holds between applied forces and displacements. The result of the nonlinear effects is a stiffness matrix which is not constant during the load application. As a result, a different solving strategy is required for the nonlinear analysis but modern analysis software makes possible to obtain solutions to this type of problems [100]. Ansys is a pioneer in the discipline of nonlinear analysis. Its nonlinear capabilities have evolved according to the emerging analysis needs, the new nonlinear methods and the increasing computing power [99].

The aim of doing a nonlinear analysis, after doing a linear one, is to check if there is buckling in the structure when both load cases, the one from the pull-up maneuver and the one from the cruise, are applied. If the loads would have caused buckling it would have been necessary to strengthen the structure by adding ribs. Fortunately, the nonlinear analysis converged for both loads as shown in Figures 3.9 which means that there is not buckling when the loads are applied.

The solver used in the nonlinear analysis performed is a sparse direct solver which is a robust choice for all forms of nonlinear analysis since it is applicable to real, complex, symmetric and non-symmetric systems. It has been optimized for sparsely populated matrices like those found in finite element analysis [99]. The deformed shape together with the undeformed edge are plotted in Figure 3.9.

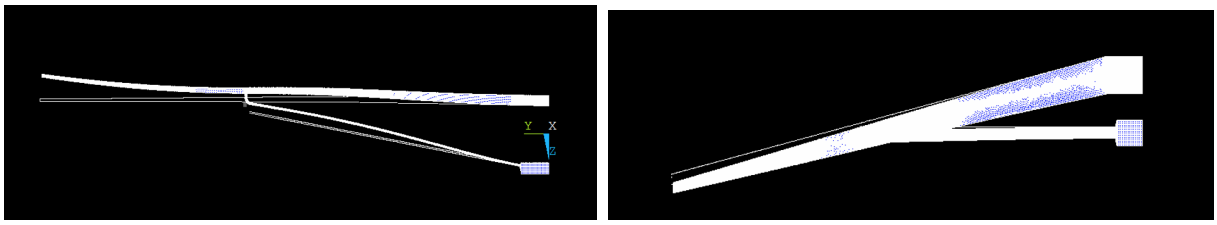

(a) Front view (b) Top view

Figure 3.9: Deformed shape of the High-Fidelity model

Chapter 4

Optimization

Optimization helps to design more efficient structures, finding the best possible solution by changing variables. Design optimization is a tool that replaces a large iterative design process and obtains better results [101]. It requires a formulation of the optimization problem that includes design variables, objective function to be minimized or maximized and constraints that need to be satisfied. The design variables are changed automatically by an optimization algorithm. An MDO architecture involves multiple disciplines although in this project only one discipline will be used.

As in any computational tool, design optimization must be a trade-off between the fidelity and the cost. If the models are too computationally expensive to evaluate in each iteration, it should be considered to decrease the fidelity. After the optimization, the design has to be validated by evaluating the design with higher-fidelity simulation tools or performing experiments. A brief theoretical overview of optimization is provided in the next section based on the textbook by Martins and Ning [76], followed by the problem formulated for this work.

4.1 Optimization Problem Formulation

The first step when solving an optimization problem is to describe it, including a statement of all the goals and requirements to be fulfilled. In addition, all the inputs and outputs of the analysis should be identified.

This project is going to solve two different optimization problems. The first optimization problem is an unconstrained problem which quantify the differences between the Low and High-Fidelity models. The Low-Fidelity model provides the deformation and the stress, and this first optimization computation is going to check if the High-Fidelity model, given the thickness distribution of the SBW, gets the same results. The second optimization problem is a constrained problem that optimizes the thickness distribution to obtain the minimum structural weight given deformation and stress constraints. Both problems are defined with more detail below.

4.1.1 Design Variables

The design variables are the inputs parameters that are allowed to change during the optimization process. They remain fixed at each optimization iteration and are modified according to the optimizer algorithm chosen. The number of design variables, n_x, determines the dimensionality and degrees of freedom of the problem. They are represented by a column vector:

$$x = [x_1, x_2, ..., x_{n_x}] \tag{4.1}$$

There are two types of design variables, continuous or discrete. This project is going to use only continuous variables which are real numbers that are allowed to vary continuously within a prescribed range without gaps. This can be written mathematically as:

$$\underline{x_i} \leq x \leq \bar{x_i}; \quad i = 1, \ldots, n_x \tag{4.2}$$

Both optimization problems have the same design variables which are the skin and spar thicknesses distributions of the main wing and strut, and the kink position of the strut at the fairing and at the joint between the main wing and strut. The total amount of design variables is 13. They are detailed in Table 4.1, as well as their lower and upper bounds.

Variable	Lower bound	Upper bound	Description
x_1 $[mm]$	2	23	Skin thickness at the root
x_2 $[mm]$	5	14	Skin thickness at the joint inboard
x_3 $[mm]$	8	30	Skin thickness at the joint outboard
x_4 $[mm]$	0.5	8	Skin thickness at the tip
x_5 $[mm]$	2	22	Spar thickness at the root
x_6 $[mm]$	5	13	Spar thickness at the joint inboard
x_7 $[mm]$	8	30	Spar thickness at the joint outboard
x_8 $[mm]$	0.5	8	Spar thickness at the tip
x_9 $[mm]$	20	100	Strut thickness at the joint
x_{10} $[mm]$	8	50	Main strut thickness
x_{11} $[mm]$	30	70	Strut thickness at the fairing
x_{12} $[\%]$	5	25	Kink position at the joint measured as strut length %
x_{13} $[\%]$	75	95	Kink position at the fairing measured as strut length %

Table 4.1: Optimization design variables

4.1.2 Objective function

The objective function, *f(x)*, is a scalar function of what is used to quantify whether one design is better than another. This function should be minimized or maximized by changing the design variables mentioned previously. The selection of the objective function is essential to be successful in the design optimization. If it does not represent the aim of the optimization, the optimum computed will not be the optimum of the optimization problem intended to be solved.

In the first optimization problem, the unconstrained one, the objective function measures how far or

how close is the deformation obtained by Ansys to the one from the Low-Fidelity model in cruise flight condition. As the objective is to match the deformations, the more similar are the deformations, the better. To do so, it has been used the estimator Mean Square Error (MSE) which measures the average squared difference between the estimated value which is the one from Ansys and the actual value which is the one from the Low-Fidelity model. Generally, the MSE has the same units of measurement as the square of the quantities being estimated which, in both optimization problems, are meters and radians.

In Equation 4.5 the displacement and rotation MSE are summed, but even if initially the units of measurement are not the same, each one of this two magnitudes include in the different factors (A to F) that multiply each MSE value the dimensionalization required to sum the rotation and displacement MSE. It has to be noted that, the values calculated with Equation 4.5 in each optimization are just an indicator of how close is the deformation of the High-Fidelity model to the Low-Fidelity one.

The deformation considers both transational and rotational displacements in x,y,z directions. Due to the type of load applied, not all the displacements and rotations are equally important, being the vertical and the twist the most important ones, which corresponds with the displacement in z and rotation around the y axis of the global reference system of the model. The MSE has been calculated for each one of the six degrees of freedom and the MSE for each coordinate has been multiplied by a coefficient to be able to prioritize the important displacements. The process to determine the coefficients and its values are detailed in Section 4.3.2. In Section 3.1, where the Boundary Conditions of the case study are defined, some beam nodes have all their degrees of freedom restricted. These beam nodes, which are located at the main wing root and fairing, together with the following beam node in the outboard direction are not used in to compute in Matlab the objective function shown in Equations 4.3 and 4.4. The reason is that they have zero displacement and rotation or a very small value so a slight difference between the High and Low-Fidelity models will result in a large error.

The Mean Square Errors for the transational and rotational displacements in x,y,z can be expressed as:

$$MSE_{xyz} = \frac{1}{n}\sum_{i=1}^{n}(A \cdot (\Delta x_i - \Delta\hat{x_i})^2 + B \cdot (\Delta y_i - \Delta\hat{y_i})^2 + C \cdot (\Delta z_i - \Delta\hat{z_i})^2) \tag{4.3}$$

$$MSE_{\theta_{xyz}} = \frac{1}{n}\sum_{i=1}^{n}(D \cdot (\Delta\theta_{x_i} - \Delta\hat{\theta}_{x_i})^2 + E \cdot (\Delta\theta_{y_i} - \Delta\hat{\theta}_{y_i})^2 + F \cdot (\Delta\theta_{z_i} - \Delta\hat{\theta}_{z_i})^2) \tag{4.4}$$

The MSE used in the unconstrained optimization is given by the sum of the weighted transational and rotational MSE calculated as previously shown:

$$MSE = MSE_{xyz} + MSE_{\theta_{xyz}} \tag{4.5}$$

The objective function for the second optimization problem, the constrained one, is to minimize the

structural mass. To do so, the structural mass resulting of the optimization (M) is compared with the one of the Low-Fidelity model (M_0) detailed in Table 3.5 dividing both masses as shown in Equation 4.6. If the objective value is lower than one, the optimized thickness distribution will require lower weight than the Low-Fidelity one. In the opposite case, if the objective value is higher than one, the optimized structure will heavier.

$$f(x) = \frac{M}{M_0} \tag{4.6}$$

4.1.3 Constraints

Constraints are used to restrict the design variables and they define the feasible region which is the region in the design space that satisfies all the constraints. There are two type of constraints, the equality constraints that restrict the function to be equal to a fixed value and the inequality constraints that restrict the function to be less or equal than a value. As the problem must not be over-constrained, the number of independent equality constraints must be less or equal to the number of design variables $g_i(x) \leq 0$.

The first optimization problem is unconstrained in order to check the accuracy of the Low-Fidelity model, as it has been mentioned previously. The optimizer has absolute freedom in all the parameters to match the objective displacements. On the other hand, the second optimization problem is a constrained one. The constraints are the deformation, that should be the same as the one obtained with the Low-Fidelity model, and the stress, that should not exceed the maximum yield stress of the material. As it has been detailed in Section 3.1, the stress constraint is for the pull-up maneuver because the wing has to resist stresses in this high load case.

The equations for the constrained problem are given by:

$$\begin{aligned} g_1 = A \cdot max(|\frac{\Delta x - \Delta x_0}{\Delta x_0}|) + B \cdot max(|\frac{\Delta y - \Delta y_0}{\Delta y_0}|) + C \cdot max(|\frac{\Delta z - \Delta z_0}{\Delta z_0}|) + \\ + D \cdot max(|\frac{\Delta \theta_x - \Delta \theta_{x_0}}{\Delta \theta_{x_0}}|) + E \cdot max(|\frac{\Delta \theta_y - \Delta \theta_{y_0}}{\Delta \theta_{y_0}}|) + F \cdot max(|\frac{\Delta \theta_z - \Delta \theta_{z_0}}{\Delta \theta_{z_0}}|) - m \end{aligned} \tag{4.7}$$

$$g_2 = \frac{\sigma - \sigma_{max}}{\sigma_{max}} \tag{4.8}$$

where Δ are the displacements and rotations of the High-Fidelity model, Δ_0 are the ones of the Low-Fidelity model and m is the margin that allows some freedom to the optimizer to accommodate some differences between the deformations of both models. In the same way as the objective function detailed in Equation 4.5, the beam nodes located at the main wing root and fairing, together with the following beam node in the outboard direction are not used to compute in Matlab the Equation 4.7. The margin is further explained in Section 5.2 where a parametric study is performed to see the implications of it

in terms of mass and stress. Both, displacement and rotations, are computed for each beam node. In the same way as in the objective function of the unconstrained optimization, each degree of freedom is multiplied by a coefficient from A to F that will be defined below in Section 4.3.2 where an objective function study is performed for the unconstrained optimization. Since the constraint has to be a number and not an array with all the MSE values, instead of computing the MSE for the deformation constraint, it has been taken the maximum value of the relative error for each degree of freedom. Then, all these values have been multiplied by a coefficient and have been summed. The second equation define the stress constraint. The never exceed stress is σ_{max} = 266 MPa, which is the ultimate strength of the aluminium alloy (400 MPa) taking into account the safety factor (1.5).

4.1.4 Optimization Problem Statements

The optimization problem statement arises from the design variables, objective function and constraints defined previously. A generic optimization problem can be stated as: minimize the objective function by varying the design variables within the bounds subjected to the constraints. It can be written mathematically as follows:

$$\begin{aligned} \text{find} \quad & x \\ \text{to minimize} \quad & f(x) \\ \text{by varying} \quad & \underline{x}_i \leq x \leq \bar{x}_i \qquad i = 1, \ldots, n_x \\ \text{subject to} \quad & g_i(x) \leq 0 \qquad j = 1, \ldots, n_g \end{aligned} \tag{4.9}$$

On the one hand, the statement of the first optimization problem is to optimize the thickness to obtain the same deformation that the one of the Low-Fidelity model in a cruise flight condition by varying the thickness and its distribution along the main wing and the strut.

$$\begin{aligned} \text{find} \quad & x \\ \text{to minimize} \quad & f(x) = MSE_{xyz} + MSE_{\theta_{xyz}} \\ \text{by varying} \quad & \underline{x}_i \leq x \leq \bar{x}_i; \quad i = 1, \ldots, 13 \end{aligned} \tag{4.10}$$

On the other hand, the statement of the second optimization problem is to minimize the structural weight while trying to obtain the same deformation that the one of the Low-Fidelity model also in a cruise flight conditioning by varying the thickness and its distribution along the main wing and the strut without exceeding a given value of stress in pull-up maneuver conditions.

$$
\begin{aligned}
\text{find} \quad & x \\
\text{to minimize} \quad & f(x) = \tfrac{M}{M_0} \\
\text{by varying} \quad & \underline{x}_i \leq x \leq \bar{x}_i \qquad i = 1, \ldots, 13 \\
\text{subject to} \quad & g_1 \leq 0 \qquad g_2 \leq 0
\end{aligned}
\tag{4.11}
$$

4.2 Optimization Algorithms

An optimization algorithm is a procedure which is run iteratively and compares the solutions of each iteration until the optimum solution is found. Several algorithms have been developed to solve optimization problems but not all the algorithms are adequate for all the optimization problems. For this reason, the selection of an appropriate algorithm is crucial and depends on the types of variables involved.

4.2.1 Classification

Optimization algorithms can be classified by order, search, optimality criterion, iteration procedure, function evaluation, stochasticity and time dependence. Figure 4.1 shows the details of the classification.

For zeroth order information, gradient-free algorithms are used. They require to provide the models that compute the objective and constraint values. Gradient-based algorithms use gradient of the objective and constraint function with respect to the design variables. The gradients provide more information about the function behaviour and are used to check if the analysis has reached the optimum solution. A great advantage of the gradient-based algorithms is their self-adaptivity which is shown at each iteration when the variables are adjusted with an adequate magnitude, based on the gradient value.

Gradient-free algorithms are based on both mathematical and heuristic optimality criteria. However, gradient-based algorithms are usually based on mathematical principles. In addition, gradient-based algorithms are usually deterministic which means that, given a particular input, the algorithm always evaluates the same points and converge to the same result.

Most of the engineering problems are constrained. There are three methods for constrained optimization problems: penalty functions, sequential quadratic optimization and interior-point methods. This last two methods are the ones used nowadays in gradient-based algorithms since the penalty functions have been replaced by more effective methods. Both methods are applications of Newton's method to the Karush–Kuhn–Tucker (KKT) conditions. The main difference among them is the treatment of the inequality constraints. Penalty functions are used for gradient-free algorithms.

On the one hand, sequential quadratic programming (SQP) methods solve iteratively a sequence

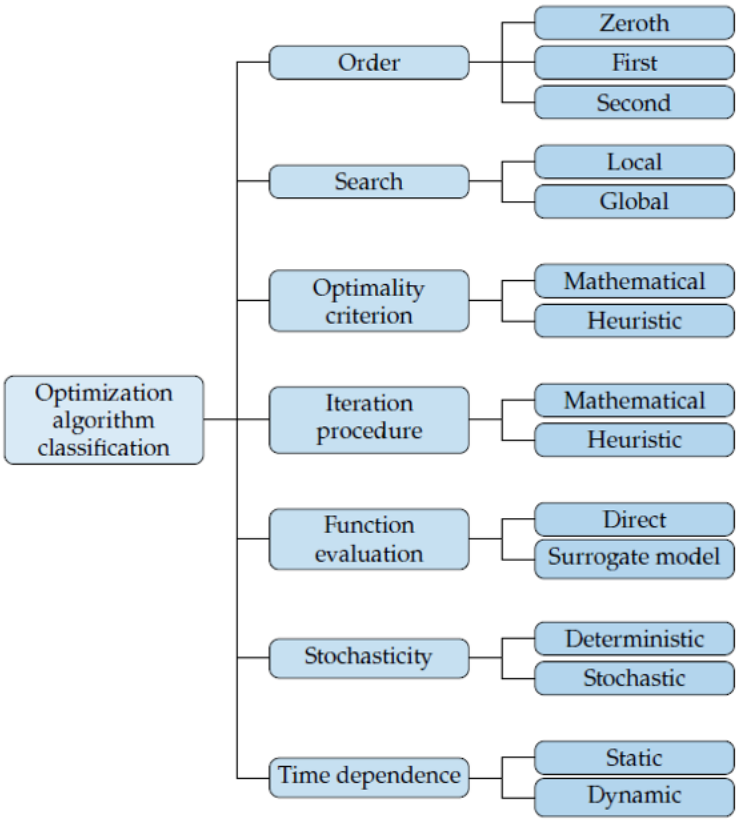

Figure 4.1: Optimization Algorithms Classification [76]

of quadratic programming problems. They are used on mathematical problems for which the objective function and the constraints are twice continuously differentiable. SQP methods differentiate active and inactive constraints, using the potentially active constraints like equality constraints and ignoring the potentially inactive ones.

On the other hand, Interior Point Methods are a certain class of algorithms that solve linear and nonlinear convex optimization problems. They add slack variables to force all constraints to behave like equality constraints.

While most of the engineering problems are constrained, unconstrained problems can also be required as it occurs in this work. The unconstrained optimization problems are solved using gradient information to determine a path from a baseline design to the optimum. Gradient-based algorithms start with a guess and generate a series of points that converge to a local optimum. At each iteration, some form of the Taylor series about the current point is used to find the next point. Because of the Taylor series being only guaranteed to be a good model locally, a globalization strategy is needed to ensure convergence to an optimum. In this context, globalization means to make the algorithm robust enough that it is able to converge to a local minimum starting from any point in the domain. There are two main globalization strategies, line search and trust region.

The line search approach consists of three main steps for each iteration that must be repeated until some convergence criterion is satisfied. First of all, choose a suitable search direction based on a Taylor series approximation. Then, perform a line search to determine how far to move in the direction chosen previously. Last, move to the new point and update all the values. The method used to find the search direction is what names the particular algorithm such as Newton's method that uses second-order information to enable better estimates of favorable search directions or Quasi-Newton's method which uses gradients along each step in the iteration path to build an approximation of the Hessian.

Trust region strategy also consists of three steps for each iteration. First of all, create a model about the current point based on a Taylor series approximation or another type of surrogate model. Then, minimize the model within a trust region around the current point to find the step. Finally, move to the new point, update the values and adapt the size of the trust region.

Generally, trust-region methods are more strongly dependent on accurate Hessians than line search methods. Thus, they are only effective when exact gradients are supplied. Although trust-region methods generally require fewer iterations than quasi-Newton methods, each iteration requires more computational cost because it needs at least one matrix factorization. As supplying second derivatives is often prohibitive, typically quasi-Newton methods are used where the Hessian is estimated from changes in the gradients.

4.2.2 Algorithm implemented

As it has been mentioned previously, the computational tool used to do the optimization is Matlab. More specifically, the nonlinear programming solvers *fmincon* and *fminunc* provided by Matlab's Optimization Toolbox.

The *fmincon* solver finds a constrained minimum of a scalar function of several variables starting at an initial estimate. It has five algorithm options: Interior Point Method, Trust Region Reflective, SQP, SQP-legacy and Active-Set. The one selected to perform the structural optimization of this project is Interior Point Method since it is a good option to obtain a feasible solution because this algorithm tries first to reach a feasible solution and then it minimizes the objective function. If a feasible solution is provided by this algorithm, the SQP algorithm will be computed to see if it can provide a better minimum. This type of algorithm tries first to minimize the objective function and then tries to reach a feasible solution.

The *fminunc* solver finds an unconstrained minimum of a scalar function of several variables starting at an initial estimate. Matlab gives two algorithm options for this solver: Quasi-Newton and Trust-Region. It has been selected the first option in order to avoid a poor optimization if the gradients supplied are not exact due to its lower dependence on accurate Hessians than trust-region methods. In addition,

Quasi-Newton method is a well-known effective method for solving unconstrained optimization problems. The algorithm used by Matlab is more specifically a Broyden–Fletcher–Goldfarb–Shanno Quasi-Newton method with a cubic line search procedure which uses gradients along each step in the iteration path to build an approximation of the Hessian.

Below is described a gradient-based unconstrained optimization using a line search algorithm with a Quasi-Newton method to determine the searching direction. Furthermore, an schematic chart of the optimization process followed is shown in Figure 4.2.

Algorithm 1 Line search algorithm

Input:

$x^{(0)}$: baseline thickness distribution ▷ Starting point

τ ▷ Convergence criteria

Output:

x^* : ▷ Optimal point

$f(x^*)$: ▷ Corresponding function value

1: **while** $||\nabla f||_\infty > \tau$ **do** ▷ Optimality condition

2: Determine search direction, $p^{(k)} = -B^{(k)^{-1}} \nabla f^{(k)}$ ▷ Quasi-Newton method

3: Determine step length, $\alpha^{(k)}$ ▷ Line search algorithm

4: $x^{(k+1)} = x^{(k)} + \alpha^{(k)} p^{(k)}$ ▷ Update design variables

5: $k = k + 1$ ▷ Increment iteration index

6: **end while**

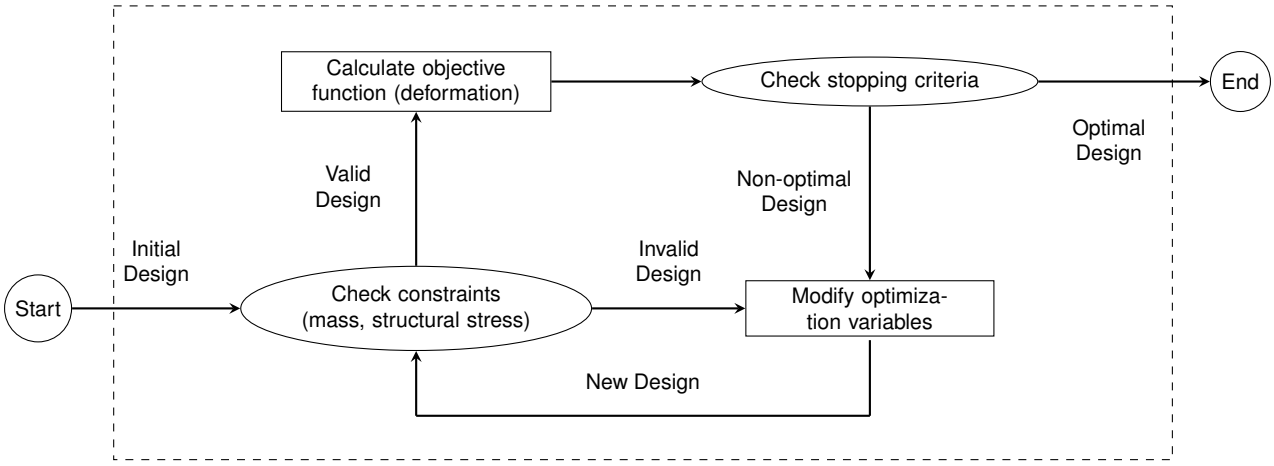

Figure 4.2: Optimization Flow Chart

4.3 Design optimization

Given the dependence of the results and convergence of gradient based algorithms on the starting point, it is highly recommended to test different starting points within the design space. If only one starting point is tested, the solution given by the optimizer could be a local minimum and not the global

minimum of the problem. As in the constrained optimization problem there are upper and lower bounds for all the design variables, shown in Table 4.1, the different starting points tested in both, constrained and unconstrained, optimization problems are within the design variables bounds.

Below are going to be detailed more design optimization issues that have been taken into consideration such as the problem scaling and the objective function study.

4.3.1 Problem scaling

Problem scaling is one of the most important considerations to put optimization in practice. For general nonlinear functions, poor scaling of the problem can decrease the effectiveness of any method used to solve the optimization [76].

Both optimization problems described in Section 4.1 have two types of design variables, one type related to the thickness which is measured in millimeters and the other type related to the kink positions at the strut which is measured in meters. If both type of design variables were measured in meters, then the derivative in the thickness direction would be large compared to the derivative in the kink position direction. In other words, the design space would have an extremely steep and short valley in one direction, and gradual and long in the other so the optimizer would have difficulties to solve the problem with this type of problem scaling. That is the reason why it is important the unit choice selected for each design variable.

Usually, a good starting point for many optimization problems is to scale every design variable to be around unity [76]. The design variables related to the thickness used in both optimization problems are scaled with the maximum upper bound thickness. Thus, all the design variables related to the thickness and the lower and upper bounds of them used in the constrained optimization problems are between 0 and 1. The design variables related to the kink positions at the strut are also scaled to be between 0 and 1. The one which is related to the kink position at the joint has been divided by 100 and the one related to the kink position at the fairing is divided by 10. They have different scaling due to their one order of magnitude difference.

4.3.2 Objective function study

As it has been mentioned previously, the objective in the unconstrained optimization problem is to match the deformation of the Low-Fidelity model. The deformation of the structural model is given by the displacements and rotations in the three axis. As a result of the loads applied and of the aim to match the deformation, the vertical displacement and the rotation in the spanwise direction axis are the most important ones, but the weight of them in the objective function is unknown. For this reason, it is going to be performed an objective function study where the Mean Square Error (MSE) is going to

be computed with different coefficients for each coordinate. The aim of it is to find out what values of the coefficients A to F of Equations 4.3 and 4.4 minimize the objective function, match better the two relevant degrees of freedom which are vertical displacement and twist and require a lower structural mass without increasing considerably the maximum stress value. These magnitudes, for the different objective functions computed, are shown in Table 4.3. In addition to these magnitudes, the bending has been added to check that the difference between both models is small so it does not affect significantly the lift distribution.

To describe the rotations the terms bending, twist and sweep are going to be used referring to the rotation around the x, y and z axes, respectively. Throughout the thesis when comparing the results and in the optimization processes, twist is going to be considered more important than bending due to its impact on aerodynamics. A slight modification in the twist results directly in a change in the angle of attack, which is important to bear in mind because a small difference in the angle of attack of the airfoils along the structure is going to change the lift distribution. The aim of both optimization problems, that are going to be solved, is to match the deformation between the High and Low-Fidelity models which results in having the most similar lift distribution possible. In addition, bending is related to the dihedral angle which, in turn, is the one related to the vertical displacement. If the dihedral angle is changed a few degrees, the change in the lift distribution is negligible. The lift distribution resulting of varying slightly the dihedral angle would be the initial lift distribution multiplied by the cosine of this dihedral angle which is approximately the unity so it remains the same.

The different weight configurations for each one of the six degrees of freedom used to obtain the thickness distribution shown in Table 4.3 are presented in Table 4.2. The sum of the different coefficients that multiply the MSE of each degree of freedom is 1 but to ease the understanding of the values they are going to be presented as percentages in Table 4.2.

The objective function study has been performed using the first optimization problem described, the unconstrained one. The objective function selected in this section is going to be used in both, unconstrained and constrained, optimization problems but in the former is used as objective function and in the latter the coefficients obtained in this study are used in the constraint function. In the hypothetical case that the High and Low-Fidelity deformations were the same, the objective function will be zero. As any optimization process, it has been allowed some tolerance in the results so the deformation is going to have some error. As the aim of it is to represent the goal of the optimization, all the degrees of freedom need to be summed to compare both deformations.

From the objective function thk1 to thk7 it can be observed that the % of twist increases progressively. When observing the results, this degree of freedom was the one that had the worst match to the Low-Fidelity result. As it has been mentioned, the twist is one of the most important degrees of freedom, so the aim is to adjust the objective function to match it on the best way possible. The other degrees of

Objective function name	Chordwise (A) x [%]	Spanwise (B) y [%]	Vertical (C) z [%]	Bending (D) θ_x [%]	Twist (E) θ_y [%]	Sweep (F) θ_z [%]
Thk1	10	15	15	25	20	15
Thk2	5	5	5	35	30	20
Thk3	5	5	5	25	40	20
Thk4	5	10	15	10	50	10
Thk5	1	10	5	5	69	10
Thk6	1	5	5	4	71	14
Thk7	1	2	2	4	81	10
Thk8	1	2	2	40	30	25
Thk9	1	2	2	50	30	15
Thk10	15	20	25	15	15	10
Thk11	20	25	30	10	10	5

Table 4.2: Objective function study - Weight configurations

freedom have different factors along these distributions, being higher the ones of the rotations than the ones of the displacements because it was noticed that the displacements match very well with a small weight. It can be seen in Table 4.3, where the results of the different objective functions are summarized, that the higher is the twist factor, the higher are the structural mass and the maximum stress.

The objective functions thk8 and thk9 give more importance to the bending rather than to the twist to check if a higher bending factor is helpful to match the twist without increasing the maximum stress and the structural mass. These objective functions have very small displacement factors because they match as well as with higher ones so, in this way, it is possible to increase it in the rotations that give worst results. Further down in Table 4.3, it can be seen that it does not help to match the twist nor to have a lower maximum stress neither a lower structural mass.

In the objective functions thk10 and thk11 it has been given more importance to the displacements rather than to the rotations to see if the mass and/or the maximum stress could be reduced since the values from the previous objective functions were not very suitable, being the structural mass and the maximum stress significantly higher than the ones from the baseline thickness distribution. It has been found (Table 4.3) that these objective functions do not give better results in terms of mass nor stress.

The results shown in Table 4.3 are going to be detailed next. The different thickness distributions of the first column are related to the distributions of Table 4.2 and the objective value is an indicator of the deformation between the High and Low-Fidelity models, as mentioned previously. The lower is the objective value, the better. The optimization time has been included to have a general idea of how hard for the optimizer is to match the objective but its value did not influence in the selection of the objective function. Furthermore, the structural weight and the maximum stress computed by Ansys are tracked to consider them in the selection of the objective function because, in principle, the intention is not to increase tremendously the structural mass and the stress to improve slightly the match in deformation between both models. The values of vertical displacement, bending and twist shown are the absolute maximum difference in each between the High and Low-Fidelity models in the whole structure. In other

Objective function name	Objective value	Optimization time $[s]$	Structural weight $[kg]$	Nodal stress max $[MPa]$	Vertical displacement $[m]$	Bending $[°]$	Twist $[°]$
Thk0	-	-	1928.5	225	0.0295	0.7485	0.3799
Thk1	6.5565e-06	34896.6	2367.5	194	0.0089	0.4714	0.5301
Thk2	5.0872e-06	38271.8	2306.3	354	0.0107	0.3575	0.4738
Thk3	3.9301e-06	55243.3	2295.6	282	0.0093	0.3409	0.3931
Thk4	4.9929e-06	63379.7	2289.0	320	0.0075	0.4595	0.3764
Thk5	4.3385e-06	51361.5	2362.7	318	0.0077	0.5400	0.3488
Thk6	4.0998e-06	56194.3	2412.2	350	0.0077	0.5642	0.3395
Thk7	3.8707e-06	49480.6	2488.1	398	0.0137	0.6766	0.3056
Thk8	4.3192e-06	42298.5	2333.5	418	0.0113	0.3204	0.4673
Thk9	4.3733e-06	54034.8	2358.0	408	0.0110	0.2983	0.4712
Thk10	6.9432e-06	29002.6	2546.7	361	0.0087	0.5296	0.5434
Thk11	6.5813e-06	38294.8	2577.9	305	0.0084	0.5336	0.5512

Table 4.3: Objective function study - Results

words, the value where each degree of freedom of the High-Fidelity model matches less the value of the Lower-Fidelity one.

It has to be highlighted that the objective function study has been computed with the unconstrained optimization which loads the structure in cruise flight conditions. As the maximum stress allowable by the structure is 266MPa, all the thickness distributions except the first one (thk1) exceed the stress limit. As the maneuver load is 1.5g bigger, the stress supported by the structure will be higher in pull-up maneuver flight conditions which is used in the constrained optimization. Consequently, the constrained optimization will require a heavier structure which is the main reason why is important to select an objective function that does not exceeds hugely the maximum stress limit neither the structural weight matching in the best possible way the deformation. As all the structural weight values are substantially higher than the one from the baseline thickness distribution (thk0), the structure required to support maneuver flight conditions will be even higher. The objective functions that compute lower structural mass, being the values significantly higher than the baseline ones, are thk3 and thk4.

In terms of deformation, the objective functions that have the lower differences between the High and Low-Fidelity models, hence the lowest objective values, are thk3 and thk7. If the vertical displacement column is observed, it can be noted that the difference in the values shown in Table 4.3 is very small, even if the factor is increased the differences are between 0.7cm and 1.3cm which is not determinant to choose between one objective function or another. However, bending and twist show significant changes in the results when different percentages are used. The best match in bending and twist is given by the objective functions thk9 and thk7, being its percentages 50% bending and 81% twist as shown in Table 4.2, respectively. This results do not differ from the ones expected because these objective functions are the ones that give the most importance to the bending and twist.

The best objective function in terms of stress is thk1, followed by thk3 which has better match in deformation than the former. In addition, thk3 requires lower structural weight than thk1. The rest of

the objective functions have higher stress and higher mass and do not match better the deformation. Since none of the objective functions match significantly better the deformation and thk3 has the second best stress, mass and deformation values, it has been decided to select the objective function thk3 for the unconstrained optimization and the factors from thk3 for the constraint function of the constrained optimization. The objective and constraint functions, detailing the coefficients A to F from thk3, are shown in Equations 4.12 and 4.13.

$$MSE = \frac{1}{n}\sum_{i=1}^{n}(0.05 \cdot (\Delta x_i - \Delta \hat{x_i})^2 + 0.05 \cdot (\Delta y_i - \Delta \hat{y_i})^2 + 0.05 \cdot (\Delta z_i - \Delta \hat{z_i})^2) + \\ + \frac{1}{n}\sum_{i=1}^{n}(0.25 \cdot (\Delta \theta_{x_i} - \Delta \hat{\theta}_{x_i})^2 + 0.4 \cdot (\Delta \theta_{y_i} - \Delta \hat{\theta}_{y_i})^2 + 0.2 \cdot (\Delta \theta_{z_i} - \Delta \hat{\theta}_{z_i})^2) \quad (4.12)$$

$$g_1 = 0.05 \cdot max(|\frac{\Delta x - \Delta x_0}{\Delta x_0}|) + 0.05 \cdot max(|\frac{\Delta y - \Delta y_0}{\Delta y_0}|) + 0.05 \cdot max(|\frac{\Delta z - \Delta z_0}{\Delta z_0}|) + \\ + 0.25 \cdot max(|\frac{\Delta \theta_x - \Delta \theta_{x_0}}{\Delta \theta_{x_0}}|) + 0.4 \cdot max(|\frac{\Delta \theta_y - \Delta \theta_{y_0}}{\Delta \theta_{y_0}}|) + 0.2 \cdot max(|\frac{\Delta \theta_z - \Delta \theta_{z_0}}{\Delta \theta_{z_0}}|) - m \quad (4.13)$$

4.4 High-Fidelity results

In this section the results of the High-Fidelity model for both flight conditions, pull-up maneuver and cruise, are going to be presented. In addition, the results of the High-Fidelity model computed with two types of load files are going to be compared. As the aim of this thesis is to assess the differences between the Low and High-Fidelity models, the design parameters that are considered relevant to do so are the displacements and rotations in the three axes and the Von Misses stress resulting from applying the loads.

To simplify the plots and to avoid confusing the reader, this section is going to present only the essential data to understand the results. For a better understanding of them, the distribution of the different degrees of freedom displacements along the structural model, obtained with the commercial software Ansys, are going to be displayed together with the graphs in the Appendix A.1. It has to be highlighted that the plot results by Ansys shown in the Appendix A and along the thesis are nodal solutions whose values are averaged at each global node. The nodal solution of a parameter at a global node is the average of all the local values of all the elements sharing that global node whereas the element solution is a non-averaged result, being unique to an individual element [95]. The reason of showing nodal plots instead of element plots is to facilitate the visualization of the results since in the element plots the mesh is displayed together with the variable plotted so this latter cannot be seen properly. The graphs of the results along the thesis show the values of the different displacements in the beam nodes whose distribution is shown in Figure 4.3.

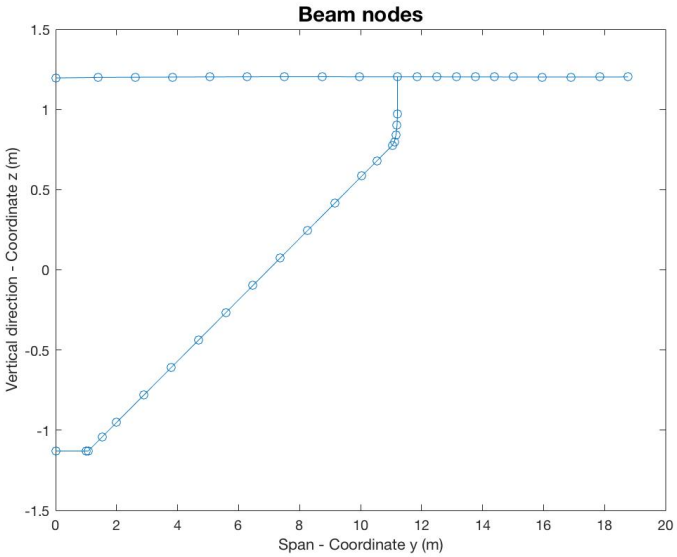

Figure 4.3: Beam nodes model distribution

4.4.1 Baseline High-Fidelity results

First of all, the results of the High-Fidelity model in cruise and pull-up maneuver flight conditions are going to be presented. As is going to be further detailed in Section 4.4.2, these results are computed using the distributed load case file, loading the skin instead of the beam nodes, which is the load file that gives the most accurate results. As all the plot legends detail, the main wing and strut beam nodes are plotted in different curves being the curves with dots for the main wing and the curves with asterisks for the strut.

Cruise flight condition

In Figure 4.4 are shown the displacements and rotations in the three coordinate axes computed with the High-Fidelity model for the cruise flight condition. As it can be seen, the biggest displacement is 0.53m in the vertical direction at the main wing tip. The vertical displacement increases smoothly from the main wing root until the main wing-strut joint but after it the slope of the curve is steeper reaching the maximum at the end of it. The displacements in x and y which are the chordwise and spanwise directions, respectively, do not present significant changes in the slope and their value increases along the wing.

As it happens in the vertical displacement, the main wing-strut joint is the point where the bending changes its behaviour and the curve starts showing a steeper slope from the joint to the tip. The reason is that the strut stiffens the first segment of the main wing. As expected, the biggest rotation is in bending at the main wing tip with a value of 4.5 degrees. The sweep is the rotation that has the lowest values, being between 0 and 1 degree in the whole wing structure and the twist goes from 0 at the root to 2 degrees at the tip without inflection points.

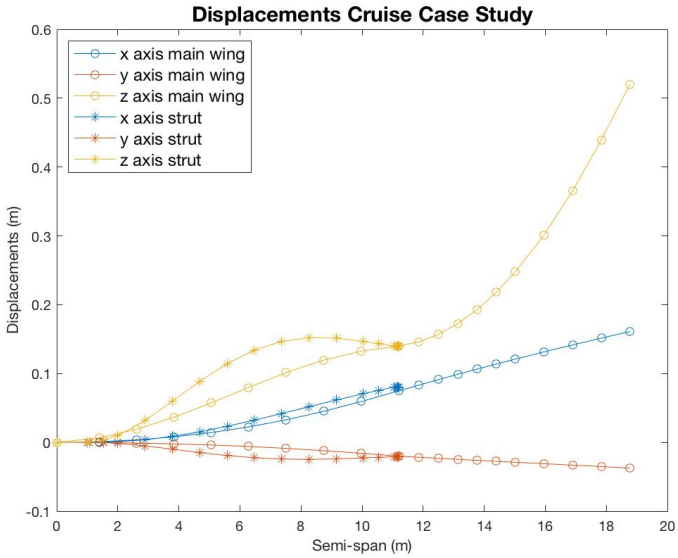

(a) Displacements

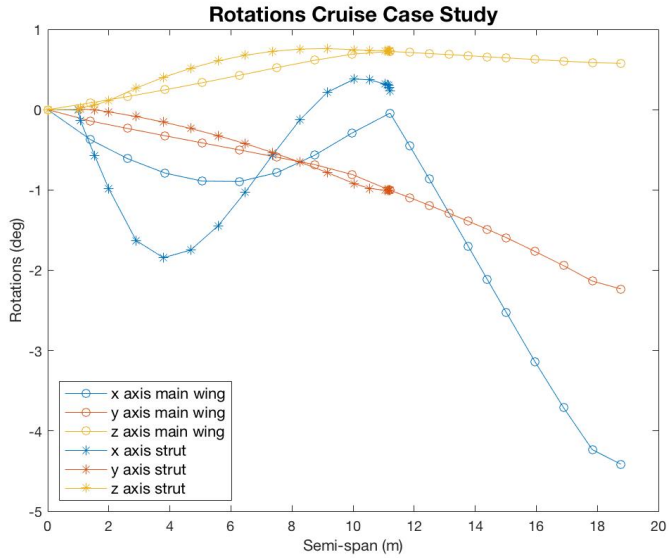

(b) Rotations

Figure 4.4: High-Fidelity model deformation results for the Cruise Case

Figure 4.5 condensate the stress results of the main wing and the strut computed with the High-Fidelity model in cruise flight conditions. The Ansys nodal stress images are presented in Figure 4.6 of the Appendix where the whole stress distribution along the structure is plotted. The stress values of Figure 4.5 are just from one small box around the beam nodes since the aim of this stress plot is to condensate the information of different sections of the structure in some points to see the general behaviour along the wing. The reason of selecting the nodes from a small box around each beam node is to be able to compare the values with the Low-Fidelity model. Since in each beam node there is an MPC element and the stress is given only by the shell elements, it has been necessary to select the maximum stress from a box around each beam node instead of selecting the stress of the beam node

itself. It is important to highlight that the maximum and minimum stress values can be in some nodes outside the box mentioned previously, as a result, the stress graphs presented along this chapter give a general idea of the stress distribution but the maximum values cannot be taken from them.

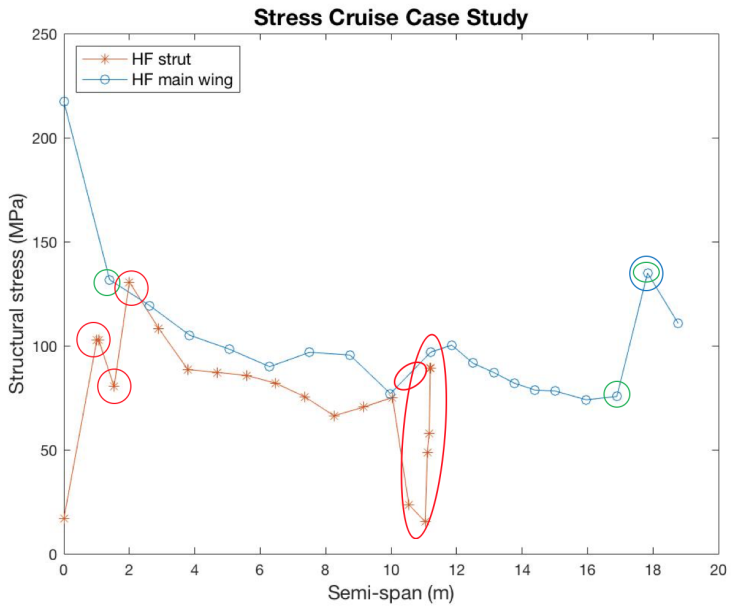

Figure 4.5: High-Fidelity model stress results for the Baseline cruise load case (distributed)

To facilitate the understanding of the results, the stress plot has some points circled with different colours. The red circles indicate the points where there is a steep thickness transition which can be verified in Figure 3.3 where the Baseline thickness distribution in plotted. As a consequence, there is a peak in the stress distribution. The steepest thickness transition is located at the main wing-strut joint at 11m in the span direction which causes the most abrupt stress change. The first strut thickness variations which show stress peaks are due to the transition from the fairing to the strut which has higher thickness at the joint but in the faring and strut itself the thickness has the main strut thickness value.

The blue and green circles represent an out of context stress value and a stress transition due to a rib, respectively. Each beam node represents a structural rib, which is a structural stiffener. In Figure 4.6, the Ansys nodal stress plot shows lower stress lines in the chordwise direction along the whole structure. This stress reduction is caused because the MPC elements prevent the skin of deforming. Furthermore, it can be noticed that the minimum stress is located at some point near the third main wing rib and the maximum stress is located near the wing tip and has a value of 287MPa. This latter is an unexpected result, which is explained later.

The minimum stress computed by Ansys is 0.194e-5MPa which is one local value and does not represent the stress in the area near that point of the structure which has the lowest stress values. It can be noticed that in the other points near it the stress values are higher.

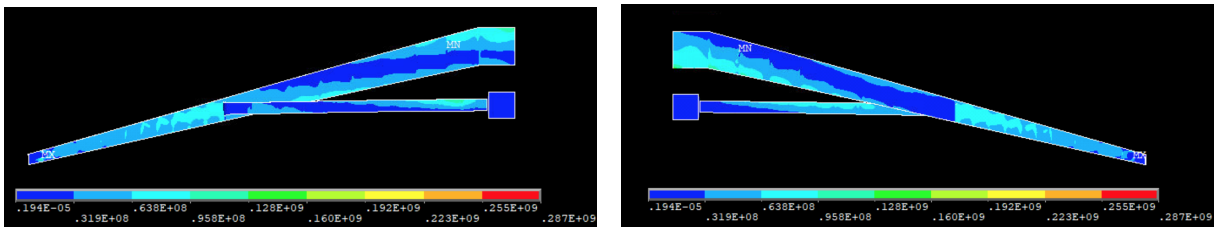

Figure 4.6: Von Misses stress results in of the High-Fidelity model for the Cruise Case

The maximum stress computed by Ansys, located near the main wing tip, is out of context. It is not distributed along the airfoil, being only a stress concentration in one small spot. In Figure 3.5, where the load distribution simulated in Ansys is shown, it can be noticed that near the wing tip there is a small load step. This small load step cannot produce the value computed by Ansys. If the maximum stress was distributed over a wider area, as it happens in the main wing root, and load step was bigger or a thickness transition that justifies the value, it would have been considered the maximum stress value computed by Ansys. Consequently, the maximum stress value shown in Figure 4.6 is going to be ignored due to the fact that is a very localized stress and is not representative of the stress along the wing. The maximum value that is going to be considered is the maximum stress at the main wing root area which is 223MPa, as shown in Figure A.3. The reason why this value is computed is that the algorithm, made to read the distributed load file and find the nearest nodes around each load, concentrates all the load on a small number of nodes instead of distributing it along the airfoil because it is not finding more nodes. Then, the MPC element, which is one type of element that simulate the ribs, constraints the area and it ends up creating the stress concentration.

Pull-up maneuver flight condition

In Figure 4.7, the displacements and rotations in the three coordinate axes are plotted for the High-Fidelity model and considering the pull-up maneuver flight condition. Even though both curves have the same trend, the magnitude is now higher than for cruise flight condition, as expected, given the higher load. As in the previous load case, the biggest displacement (0.90m) is in the vertical direction at the main wing tip. The displacements in the chordwise and spanwise directions are smooth along the wing span and their maximum values are 0.34m and 0.09m, respectively.

As it has been mentioned in the cruise flight condition results, the main wing-strut joint is the inflection point in the bending. It increases from this point to the tip where its value is maximum (7.2 degrees). The sweep is between 0 and 1.5 degrees in the whole wing structure and the twist goes from 0 at the root to 4 degrees at the tip. Compared with the cruise flight condition, the twist at the tip in the maneuver condition reaches a greater value, being approximately double.

As in the cruise flight condition, Figure 4.8 condensates the stress results computed with the High-

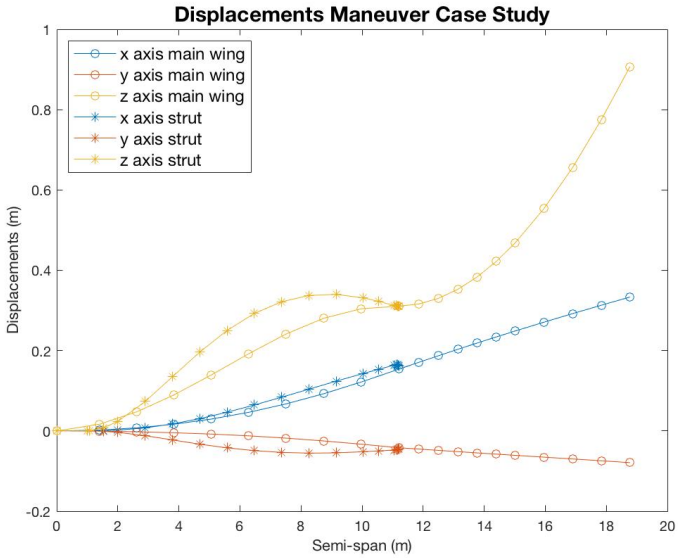

(a) Displacements

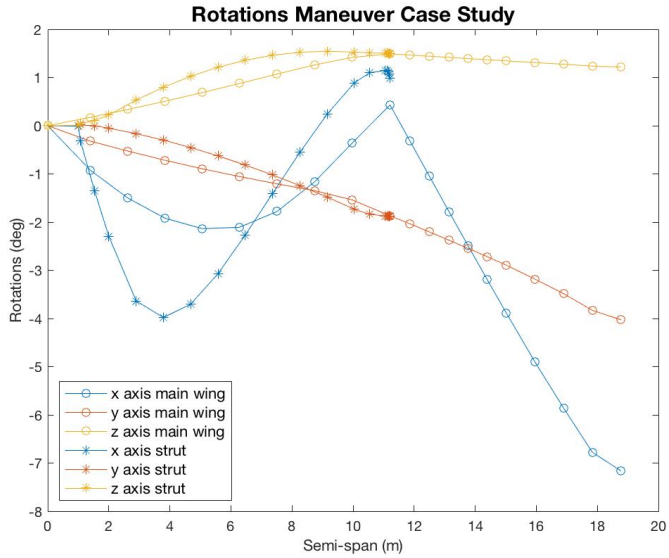

(b) Rotations

Figure 4.7: High-Fidelity model deformation results for the Maneuver Case

Fidelity model in pull-up maneuver flight conditions. This is a high load case, thus, it is expected to reach higher stresses than in cruise conditions. If both stress plots are compared, Figure 4.5 and 4.8, it can be observed that the curve trend is the same in both, but the maneuver case shows higher stress values. As in cruise condition, the stress plot has some points circled in red, blue and green which indicates big thickness transition, out of context value and rib, respectively. The baseline thickness distribution is used for both, cruise and maneuver, flight conditions which is the reason why the stress peaks due to thickness transition are the same in both stress plots. Moreover, the ribs located in the structure are the same for both flight conditions and, as in the cruise load, the maneuver load shown in Figure 3.6 has a small step located near the main wing tip. For the same reason as explained before, the maximum value computed by the software, shown in Figure 4.9, is going to be ignored since it is deemed out of context.

The maximum stress value considered is the one computed by Ansys at the main wing root which is 508MPa, shown in Figure A.3.

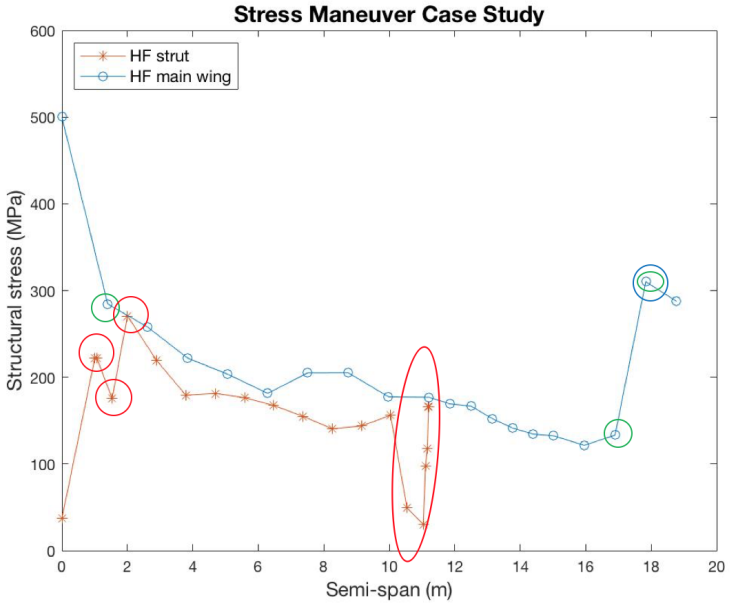

Figure 4.8: High-Fidelity model stress results for the Maneuver Case

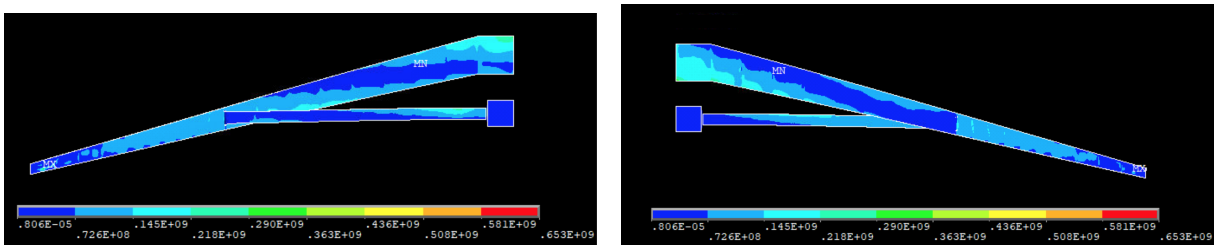

Figure 4.9: Von Misses stress results of the High-Fidelity model for the Maneuver Case

The stress at the main wing-strut joint is 200MPa, the double of the one obtained for cruise, but it is still within the allowed stress values. The maximum stress value considered is 508MPa, which exceeds in 1.91 times the maximum allowable stress limit of 266MPa. In addition, half of the main wing and the fairing-strut joint also exceed the maximum allowable stress. To be within the stress limit, it would be necessary to change the thickness distribution, adding more material where it is required which will result in a heavier structure. However, if numerical optimization is used to re-distribute the thickness distribution it might be possible to maintain or even reduce the structural weight.

4.4.2 Results comparison from condensed and distributed loads

In this section, the deformation and stress results from applying three different types of load files in the High-Fidelity model are going to be compared. Initially, the load files of both flight conditions, cruise and maneuver, were provided by the Low-Fidelity model because, as the aim of the thesis is to compare

both models, the same load has to be used. These files have the load distributed along the whole wing skin, but the main problem when using this type of load files to compute the simulation is the prohibitive computational cost which makes the optimization problem infeasible. That is the reason why it was imperative to condense the load files to make the optimization possible.

The condensed files have the loads applied only at the beam nodes which requires two orders of magnitude less time than the distributed ones, due to the fact that the former has two orders of magnitude less information in the load file than the latter. To quantify the differences in the results when the condensed files are used, it has also been computed the distributed load file applying the loads at the beam nodes. In this way, the differences between applying the load at the beam nodes instead of applying them on the skin and between reading them from a condensed file instead of a distributed one will be assessed. To summarize, the three types of load files computed are: the initial load file with the distributed load on the skin, the initial load distributed load file but applying the loads at beam nodes and, lastly, the condensed load applied at the beam nodes.

The detail of the load reactions computed by Ansys for the three different type of loads used are shown in Section 3.5. As detailed there, the reactions have been checked to verify if both, condensed and distributed load files, have the same amount of load. It was noted that the results obtained with the new condensed load file are reliable and accurate.

It is known that the most precise results in the optimizations would be the ones computed with the distributed loads on the skin. That is the reason why the reference results on the comparison of this section are the ones from the High-Fidelity model that uses the distributed load file applied on the skin.

Cruise flight condition

The results obtained at the beam nodes from applying the cruise load, considering the condensed load at the beam nodes and the distributed load on the skin and at the beam nodes, are going to be presented. The main wing and strut beam nodes are represented in the result plots by dots and asterisks, respectively. In Figure 4.10 the vertical displacement and the twist are shown since they are the most relevant degrees of freedom, as explained previously. The rest of the degrees of freedom can be consulted in the Appendix A.2.

When the cruise load is applied, the distributed and condensed files roughly get the same results as one can observe in Figure 4.10. The most significant differences are obtained for twist in the strut and last wing segment and for bending near the wing tip. The twist plot in Figure 4.10 show that the distributed file loaded at the beam nodes and the condensed file curves are coincident since both loads are applied at the same nodes. The maximum twist difference (0.25 degrees) between the distributed load on the skin and at the beam nodes is found at the tip, being the one in the beam nodes the lower in absolute value.

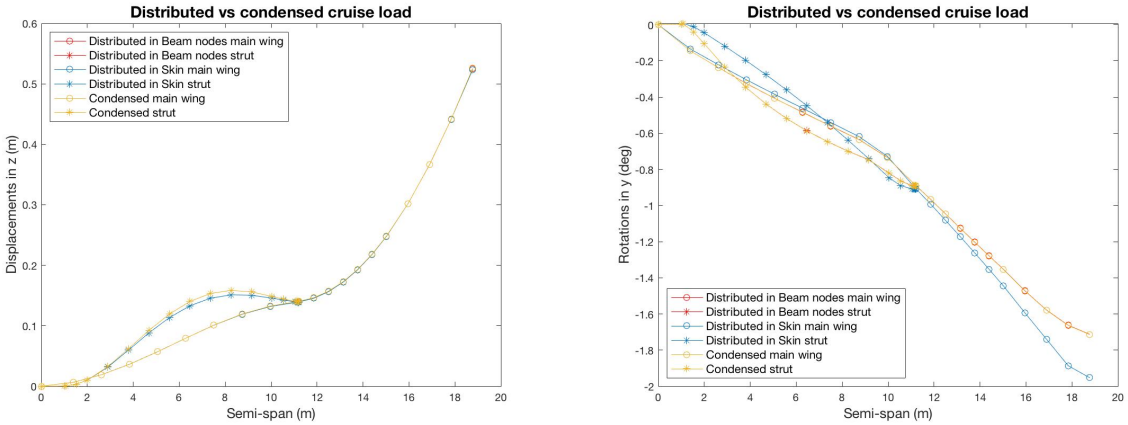

(a) Vertical displacement

(b) Twist

Figure 4.10: Vertical displacement and twist results comparison of the distributed and condensed loads for the Cruise Case

In Figure 4.11 are shown the nodal stress values, in the main wing and in the strut separately, for the condensed and distributed load files. It can be noted that the distributed load is more conservative than the condensed one, given the higher stress levels. The largest differences are located at the main wing tip and fairing-strut joint.

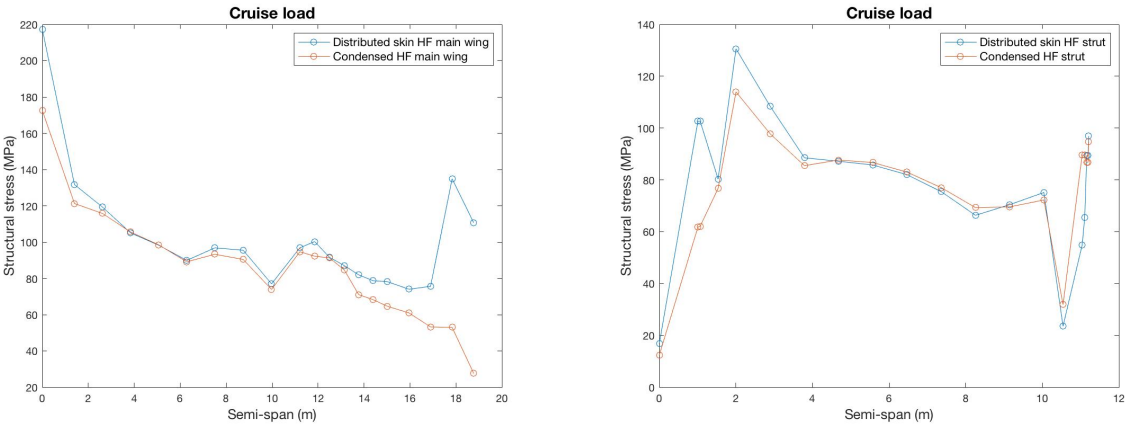

(a) Main wing

(b) Strut

Figure 4.11: Nodal stress results comparison of the distributed and condensed loads for the Cruise Case

The stress distributions along the structure and their maximum values computed by the software Ansys are shown in the Appendix A.2. The maximum stress considered for the condensed and distributed loads considering the cruise flight conditions are 219MPa and 223MPa, respectively.

These values cannot be seen in Figure 4.11 since this plot is a condensation of the stress results from a small box around each beam node and not the complete stress distribution. Since in each beam node there is an MPC element and the stress is given only by the shell elements, it has been necessary to select the maximum stress from a box around each beam node instead of selecting the stress of

the beam node itself to be able to plot the stress at the beam nodes. The maximum stress values are indicated in Figures A.8 and 4.5. The condensed load has its maximum stress value located at the main wing root. However, the distributed load gets the maximum value near the tip, where the Figure 4.11 shows a peak at the end of the main wing stress curve. As detailed in the previous section, this value has been ignored and the maximum stress value for the distributed load is also located at the main wing root. It should be noted that the distributed load is a bit more conservative than the condensed one, but none of them exceeds the maximum stress value which is 266MPa.

Pull-up maneuver flight condition

The deformation and stress results in the beam nodes obtained from applying the pull-up maneuver load are going to be shown below for the condensed load at the beam nodes and the distributed load on the skin and at the beam nodes. In the same way as in the cruise flight condition, this section presents the results of the most relevant degrees of freedom, vertical displacement and twist, in Figure 4.12. The rest of the degrees of freedom are presented in the Appendix A.2.

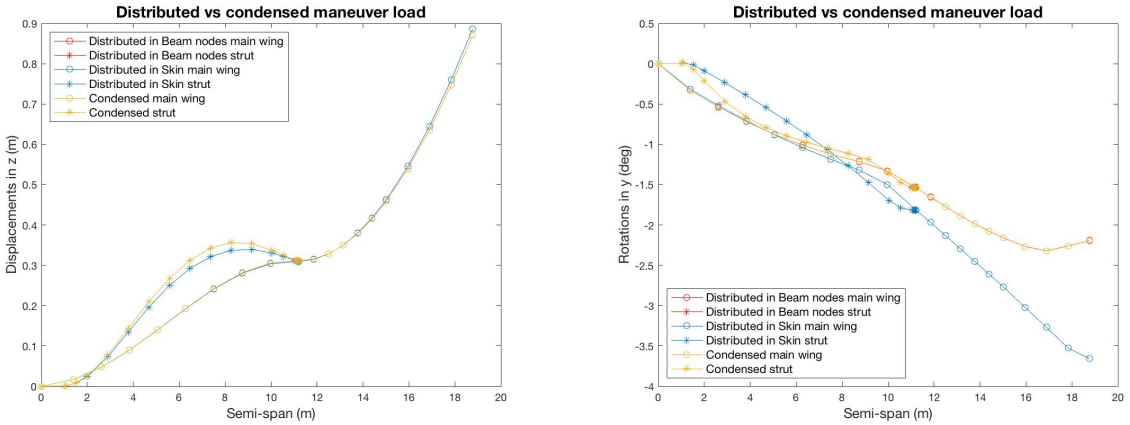

(a) Vertical displacement

(b) Twist

Figure 4.12: Vertical displacement and twist results comparison of the distributed and condensed loads for the Maneuver Case

As in the cruise condition described above, the displacements and rotations are the same in the condensed and both distributed loads; but not the twist which presents bigger differences than in cruise due to the fact that the load in maneuver is also significantly larger. The maximum difference is 1.5 degrees observed at the tip, being the distributed load on the skin the one that gets the larger value in absolute value.

In Figure 4.13 are shown the nodal stress values in pull-up maneuver flight conditions from a small box around each beam node. The complete stress distribution is shown in Figures A.9 and 4.9. As happened in the previous flight condition, the distributed load is more conservative than the condensed one, but the maximum value is almost the same which can be seen in the Ansys plots shown in the Appendix A.2. At some strut nodes both stress results are coincident but in general the distributed load

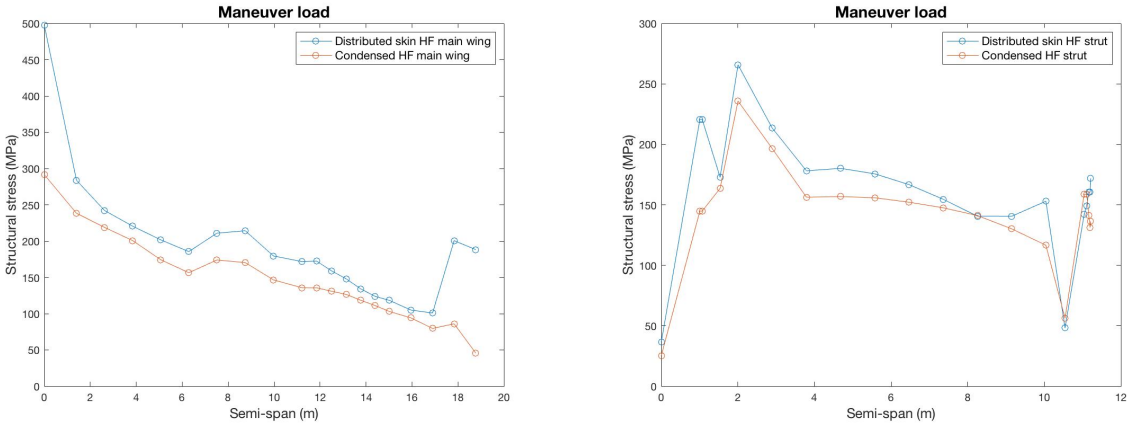

(a) Main wing

(b) Strut

Figure 4.13: Nodal stress results comparison of the distributed and condensed loads for the Maneuver Case

results in higher strees values. The stress distribution computed by Ansys where the maximum and minimum values are detailed can be found in the Appendix A.2. The maximum stress computed by Ansys has been ignored, by the same reason as before, and the value considered for the distributed load on the skin is the one at the main wing root, which is 508MPa, shown in Figure A.3. The maximum stress value computed with the condensed load is 505MPa, located at the main wing root.

Summary of the comparison

To conclude the comparison between the condensed and distributed loads it should be emphasized that without the condensed load file both optimization problems would not be possible to solve. As detailed previously, the only degree of freedom that presents significant deviations when using the condensed load file is the twist. Although it has been mentioned several times that is one of the most important degrees of freedom in this thesis, the differences have been quantified (12.8% in cruise). Furthermore, it has to be emphasized that in the optimization process, the cruise load is the one used to match the deformation between the High and Low-Fidelity models. The rest of degrees of freedom from which the deformation is calculated do not have significant aerodynamic load implications so it can be said that the deformation computed with the condensed load file is a good approximation to the one computed with the distributed load file.

Regarding the stress results, the distributed load is more conservative than the condensed one in both flight conditions. As the pull-up maneuver load is larger, the differences along the wing are bigger than in cruise. As it has been detailed previously, the maximum stress shown in the Ansys results plots with the distributed load is located near the main wing tip, but this value has been ignored and the value considered is the maximum stress located at the main wing root areas. To sum up, both stress distributions computed by Ansys, presented in the Appendix A, show a high stress area near the root whose maximum stress value is located at the upper trailing edge point of the root wing box. The nodal stress distributions computed are not exactly the same because the condensed load loads all the beam nodes

shown in Figure 4.3, but the distributed load loads the wing skin. As the maximum stress values do not have large differences, the safety factor used in both optimizations is not going to be modified. Even though the distributed load is a little more conservative than the condensed one in both flight conditions, the differences are not significant.

To sum up, the results obtained from both files have slight differences, being the ones from the condensed files the less accurate ones, but they are still representative of the problem which is going to be solved in both optimizations. Therefore, the results computed by the High-Fidelity model using the condensed load files are considered valid and they can speed up in two orders of magnitude the solving time which make the optimization process feasible.

4.5 High-Fidelity and Low-Fidelity results comparison

The Low-Fidelity results presented in this section are obtained from an in-house equivalent beam model code [102]. The stress results are obtained using the Euler-Bernoulli beam model. The Low-Fidelity model uses beam elements to represent the wing box showed in Figure 3.2 which is used as well in the High-Fidelity model to represent the wing structure. The Low-Fidelity model and the commercial software Ansys, used for the High-Fidelity analysis, use Finite Element Methods to perform the numerical analyses. The main difference between both models, which is also the main reason for the expected discrepancies in the results, is the element type. The former uses beam elements and the latter uses shell elements to represent the wing box. Although both elements can represent the structural model at a preliminary aircraft design level, the beam element model is not able to capture some local phenomena such as buckling of the wing box.

Theoretically, shell elements (2D) are more accurate than beam elements (1D) to model an entire structure. However, the main disadvantage of using the former is that they are more computationally expensive. On the other hand, the main disadvantage of beam elements in commercial finite element packages is that, even though they can model residual stress and capture spread of plasticity, they cannot model local buckling, which limits the accuracy of the analysis [103].

As the aim of this thesis is to validate the Low-Fidelity model, the differences between both Fidelity models are going to be quantified in this section. Even though it is expected differences between the High and Low-Fidelity model in the deformation and stress results, the trends of the results are expected to be the same. It should be noted that the results from both models are obtained using linear analyses. The differences found for both load cases, cruise and maneuver, are detailed below.

4.5.1 Cruise flight condition

As it has been mentioned previously, the two most important degrees of freedom are the vertical displacement and the twist, which are the ones presented below. Although all the differences in displacements and rotations are going to be discussed in these sections, the detailed plots of the chordwise and spanwise displacement as well as the bending and sweep are shown in the Appendix A.3.

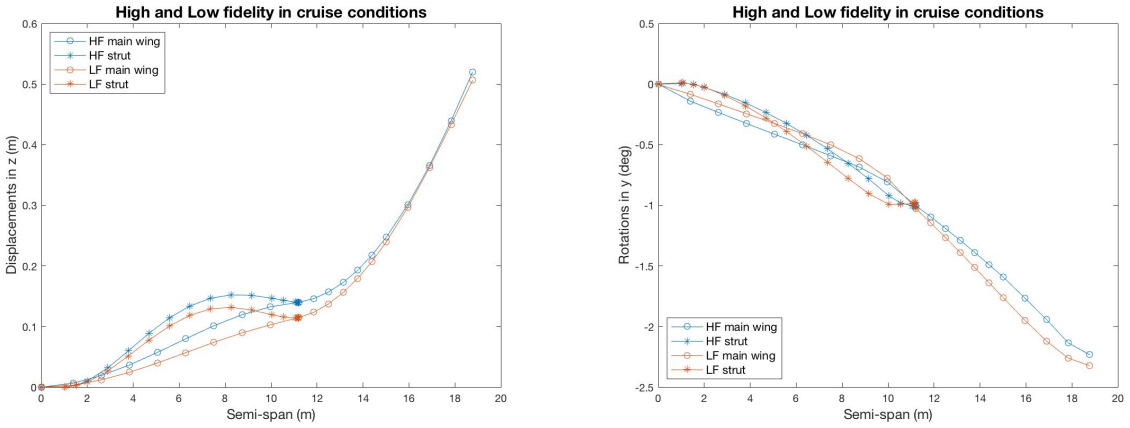

(a) Vertical displacement

(b) Twist

Figure 4.14: Vertical displacement and twist results comparison of the High and Low-Fidelity models for the Cruise Case

In general, LF underestimates the value of the displacements of the Strut-Braced Wing structure in cruise flight conditions. The largest differences in the chordwise direction displacements for the wing occur in the joint-tip segment, being the largest difference 0.95cm at the tip, where the relative error between the Low and High-Fidelity models is 6.26%. However, the spanwise and vertical displacement are well estimated in the joint-tip segment of the main wing, being the maximum difference in the spanwise direction 0.17cm (9.09%) and in the vertical direction 2.95cm (32.94%), both near the joint region. The chordwise, spanwise and vertical displacement differences in the strut increase from the fairing to the joint, being their values 0.43, 0.33 and 2.47cm at the joint node. Regarding the main wing rotations, bending and twist are underestimated only in the root-joint segment, while they are overestimated in the joint-tip segment. The largest differences in bending and twist are 0.75 degrees in the tip and 0.38degrees at one node near the tip. On the other hand, sweep is underestimated in the whole main wing, however, its maximum difference is only 0.04 degrees.

Regarding the strut displacements, the LF follows the same trend as the main wing, underestimating the displacements in the three axes. The differences in displacements are bigger at the joint, having the vertical displacement the largest difference around 2.68cm and being lower than 0.5cm in both chordwise and spanwise directions. The bending and sweep in the strut are underestimated, while the twist is overestimated. All the differences in rotation in the three axes are lower than 0.51 degrees.

It can be concluded that the largest differences are found in the vertical displacements and in the bending. Nevertheless, the High and Low-Fidelity models do not present large differences in deformations, which implies that the Low-Fidelity model gives adequate results in cruise flight condition.

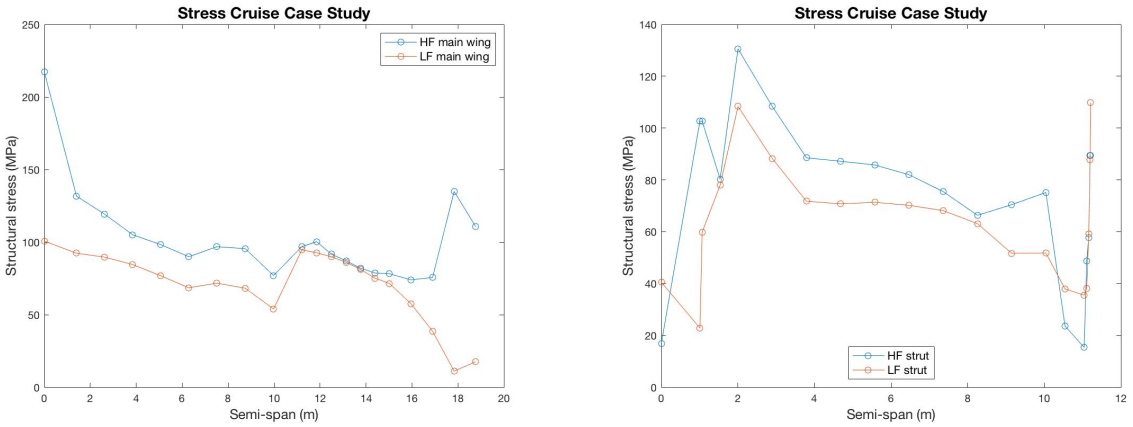

(a) Main wing (b) Strut

Figure 4.15: Main wing and strut nodal stress results comparison of the High and Low-Fidelity models for the Cruise Case

Regarding the structural stress at the main wing, the LF model is less conservative than the High-Fidelity model. The stress curve follows the same trend in the first segment of the main wing but after the joint, specially near the tip, the LF model estimates that the stress decreases significantly while the HF model estimates a lower stress decrease and a stress peak where there is load step as seen in Figure 3.5. In addition to the differences near the tip, the root also shows stress differences between both models. As it has been highlighted in the High-Fidelity results section, it is worth to recall that the stress plots presented throughout the thesis are the stress values at the beam nodes shown in Figure 4.3, which are useful to have a general idea of the stress trend along the structure. The maximum stress obtained by the software Ansys in cruise flight conditions is 223MPa at one point near the main wing root which is detailed in Section 4.4. Although the maximum stress estimated by the HF model is located at the wing tip, it is a local value and does not represent the higher stress areas which are located near the wing root, as in the LF model. The maximum stress computed by the HF model is more than twice the value estimated by the LF model, but it does not exceed the maximum stress allowable of 266 MPa.

The structural stress at the strut estimated by the LF model is also less conservative than the HF one, but not at the main wing-strut joint. The largest differences in the stress curve between both models are shown at the fairing-strut joint, where the Low-Fidelity model underestimates the stress by approximately 80 MPa. In the main wing-strut joint, where the structure presents areas with high curvature, the stress is overestimated by 20MPa.

It can be concluded that the main wing and strut stress values are underestimated by the Low-Fidelity model. However, this model overestimates the stress at the main wing-strut joint, where thickness value

has the possibility to be reduced.

4.5.2 Pull-up Maneuver flight condition

As well as in the previous section, the differences in displacements and rotations of the six degrees of freedom are going to be discussed for the pull-up maneuver, although only the vertical displacement and twist are shown in Figure 4.16. The chordwise and spanwise displacements in addition to the bending and sweep plots are shown in the Appendix A.3.

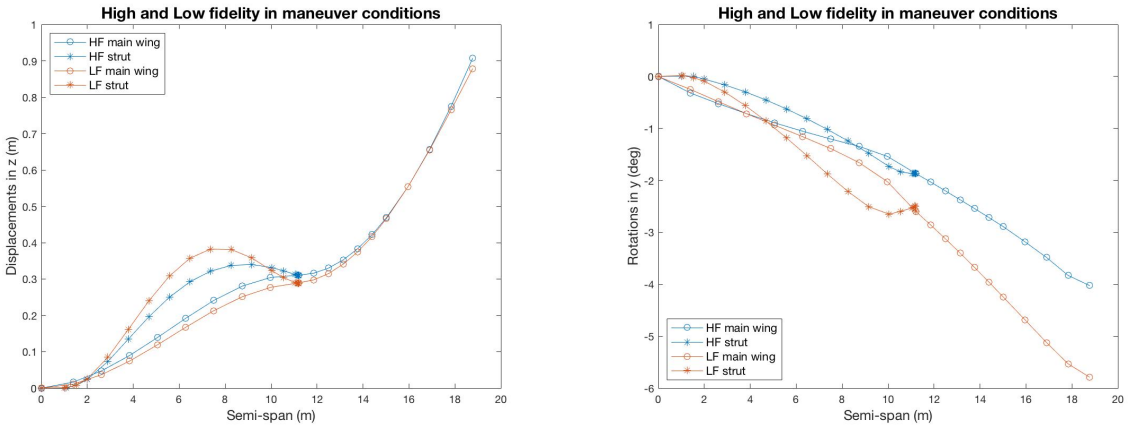

(a) Vertical displacement

(b) Twist

Figure 4.16: Vertical displacement and twist results comparison of the High and Low-Fidelity models for the Pull-up Maneuver Case

In general, LF matches well the wing, but not very well the strut. It can be noted that the displacement in the chordwise direction is the only degree of freedom that is well estimated by the LF model. The largest differences in the main wing displacements occur in the joint-tip segment, where the maximum difference in the chordwise and spanwise directions are lower than 0.92cm. The chordwise and spanwise strut displacements does not present significant differences, lower than 1.21cm for both directions. The vertical displacement presents larger errors between the High and Low-Fidelity models, being the largest displacement difference 2.69cm (13.24%) at the middle of the strut. Regarding the rotations, LF makes a good estimation of the bending and sweep for the whole main wing, but not the tip neither the strut which is overestimated in both, bending and sweep, rotations. It is important to highlight that the degree of freedom that yields largest differences is the twist. The twist differences increase in the spanwise direction up to 2.13 degrees (30.05%) at the tip.

To summarize, the displacements in the three axes are well estimated for the wing in maneuver flight conditions. However, the twist present larger differences. The estimation by the Low-Fidelity model is more accurate in cruise flight conditions, as expected, since the load is significantly lower than in pull-up maneuver conditions. Consequently, the larger is the load, the more significant the differences will be between both models.

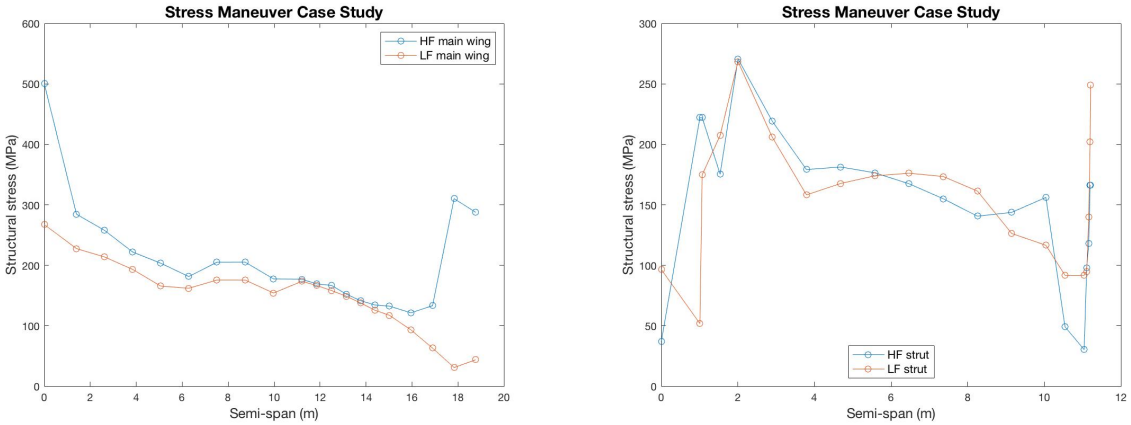

(a) Main wing

(b) Strut

Figure 4.17: Main wing and strut nodal stress results comparison of the High and Low-Fidelity models for the Pull-up Maneuver Case

Even though the stress curve follows the same trend throughout the wing, the LF model is less conservative in the main wing structural stress than the High-Fidelity model. In addition to the tip, the root shows high stress differences (87.3%) between both models. In Figure 4.9 of the Appendix it can be noticed that the maximum structural stress in pull-up maneuver conditions is 653MPa at one point near the main wing tip. However, as explained in previously, the maximum stress value considered is 508MPa at one point near the main wing root.

Regarding the structural stress strut curve, it does not have exactly the same trend in the High and Low-Fidelity models. The bigger differences are shown at the fairing-strut joint where the Low-Fidelity model underestimates the stress 175 MPa. The main wing-strut joint also present large stress differences, but in this critical part, where the structure has high curvature and a larger thickness, the Low-Fidelity model overestimates the stress between 50 MPa (in the part close to the main wing) and 80 MPa (at the joint). The HF model shows peaks of stress when there is a change in the thickness distribution, as explained in Section 4.4.1. The peak rounded in red in the strut stress plot shown in Figure 4.17 is the point that the LF model better estimates the stress. This point is located at the beginning of the strut, where the thickness value is lower compared to the one at the fairing-strut joint, as shown in Figure 3.3.

It can be concluded that the main wing stress is underestimated by the Low-Fidelity model and the baseline thickness distribution is not adequate for the pull-up maneuver case due to the maximum stress estimated by the High-Fidelity model is 1.91 times higher than the maximum stress allowable. Moreover, the main wing-strut joint does not have as much stress as the one expected by the Low-Fidelity model, which results in the possibility of reducing the thickness value in that part of the wing box.

4.5.3 Summary of the comparison

In general, LF underestimates the value of the displacements of the Strut-Braced Wing structure in both cruise and maneuver flight conditions. The biggest differences are found in vertical displacement (cruise condition 2.95cm, 32.94%), bending (maneuver condition 1.38 degrees, 25.15%) and twist (maneuver condition 2.13 degrees, 30.05%). Furthermore, the highest differences in displacement and rotation estimations are computed in the strut and wing tip. In cruise flight condition, the High and Low-Fidelity deformations do not have big differences (twist 0.38 degrees, 16% at tip) which implies that the Low-Fidelity model gives proper results. Nevertheless, in pull-up maneuver conditions the twist differences increase in the spanwise direction up to 1.77 degrees at the tip, which should be taken into account. As expected, the differences in the deformation are larger in the maneuver flight condition since the load is larger than in cruise.

Regarding the stress, the main wing and strut values are underestimated by the Low-Fidelity model, while the main wing-strut joint for both flight conditions is overestimated by the Low-Fidelity model.

To conclude, the Low-Fidelity model has an advantage in terms of computational cost, but for both flight conditions the Low-Fidelity the stress results are not well estimated. However, all the displacements and rotations, except the twist in the pull-up maneuver, present slight differences but acceptable (lower than 6.51cm and 2.13degrees) to get a general idea of the deformation of the SBW structure.

Chapter 5

Optimization results

The optimization results obtained from both constrained and unconstrained optimizations are going to be detailed below. Both problem statements, including design variables, objective functions and constraints were previously defined in Section 4.1

5.1 Unconstrained problem

The unconstrained problem aims to determine the thickness distribution that results in the closest deformation possible to the one of the Low-Fidelity model in a cruise flight condition. From the objective function study shown in Section 4.3.2 it has been decided to use the objective function thk3 which is described in Equation 4.12. Since this optimization does not have constraints, the optimizer has complete freedom to modify the thickness distribution within its upper and lower boundaries, which does not happen in the constrained optimization.

The spar and skin thickness distributions resultant of the unconstrained optimization together with the baseline thickness distribution are going to be shown in Figure 5.1. In the latter Figure, it can be observed that the optimized thickness distribution presents thickness values that fit inside the airfoils. Furthermore, the joints are located between the bounds used in the constrained optimization which means that the solution given by the optimizer is a realistic one. For these reasons, from a geometrical perspective the solution can be considered feasible. It has to be highlighted that the optimizer tries to match the deformation only for the cruise flight condition. Nevertheless, the maximum stress value, presented in Table 5.1, exceeds the maximum stress value of 266MPa. As the maneuver load is much larger than the cruise one, the maximum stress value will be much higher for that flight condition, which means that the solution obtained from the unconstrained optimization is not realistic in terms of stress for this case.

The optimized solution is shown in Figure 5.1 where it can be observed that it has the same values and distribution for the skin and spar at the strut and fairing. The thicknesses at these areas are larger

than the baseline ones, due to the fact that the optimizer tries to strengthen the structure to match the deformation. Nevertheless, the optimized main wing spar has significantly lower values than the skin and baseline ones but not at the tip, where the thickness value is larger than the baseline one, as it happens in the skin at the tip. The optimized skin at the main wing shows slightly smaller thickness values in the outer part of the kink and slightly larger thickness values at the tip which results in a better matching of the twist at the kink but not at the tip. As the optimizer has the freedom to adjust the joint, it has maintained the main strut thickness in the skin and spar during the whole strut and it has increased its value only at the joint. The baseline distribution, however, it puts the kink one meter before the joint where the thickness starts increasing its value until it reaches the joint value which is the maximum of the linear distribution.

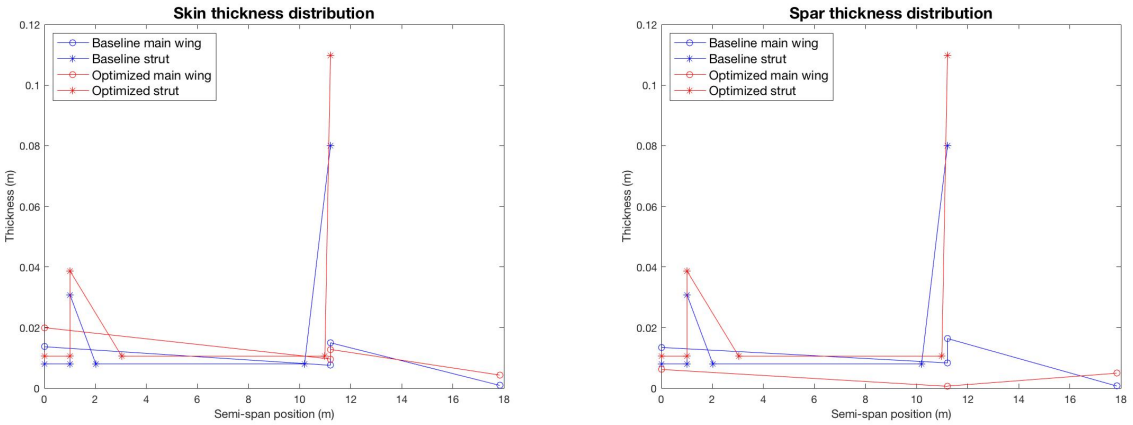

(a) Skin

(b) Spar

Figure 5.1: Thickness distribution from the unconstrained optimization

In Table 5.1 are presented the structural mass and maximum stress values together with the vertical displacement, bending and twist for the Baseline and Optimized thickness distributions. These latter magnitudes are the absolute maximum differences found between High and Low-Fidelity models, as indicated in the table heading. For comparison purposes, the Low-Fidelity results have also been included in the table. It can be noted that the differences in vertical displacement and bending are lower in the Optimized distribution than in the Baseline one but the twist difference is slightly higher. In Figure 5.2, where the vertical displacement and twist results are presented, it can be seen that the maximum difference between the High and Low-Fidelity models occur at the tip, where the Optimized distribution has a larger twist value than the Baseline one. If the whole twist graph is observed, it can be concluded that the Optimized thickness distribution matches better the Low-Fidelity twist than the Baseline one, even if the maximum difference value does not suggest the same thing.

The increase in mass for the Optimized solution in respect to the Baseline one comes from the fact that the optimizer is trying to stiffen the structure to match better the deformation. The differences at the joint shown in Figure 5.1 do not cause the mass increase shown in Table 5.1. The fact that the

optimized distribution positions the joint kink one meter more in the outboard direction than the baseline distribution compensates the thickness increase that the optimizer computes at the joint where the strut ends.

Thickness distribution	Structural weight $[kg]$	Stress max $[MPa]$	Vertical displacement $[m]$ max($\|HF-LF\|_z$)	Bending $[°]$ max($\|HF-LF\|_{\theta_x}$)	Twist $[°]$ max($\|HF-LF\|_{\theta_y}$)
Baseline	1928.5	225	0.0295	0.7485	0.3799
Optimized	2295.6	290	0.0089	0.3409	0.3931
	Structural weight $[kg]$	Stress max $[MPa]$	Vertical displacement at tip $[m]$	Bending at tip $[°]$	Twist at tip $[°]$
Low-Fidelity	1636	110	0.5063	3.8474	2.3222

Table 5.1: Unconstrained optimization thickness distribution results

The stress values shown in Table 5.1 are element results but, as it has been mentioned at the beginning of Section 4.4, the Ansys plots that allow to see the different stress values with colors are nodal results. The differences between the nodal and element solutions are 6MPa and 8MPa for the Baseline and Optimized thickness distributions, respectively. The nodal stress distributions from both Optimized and Baseline thickness distributions in cruise flight condition are shown in Figure A.16 of the Appendix A.4. The Baseline thickness distribution is the one used along the Section 4.4 where the High-Fidelity results are shown previous to the optimization. Since the unconstrained optimization uses the cruise condensed load file at the beam nodes, the Baseline thickness distribution shown in Figure A.16 is computed as well using this type of load file.

In the same way as the previous deformation plots have been displayed, in Figure 5.2 the vertical displacement and twist of the Optimized and Baseline thickness distributions for the High-Fidelity model together with the ones of the LF model are presented. The rest of displacements and rotations are shown in the Appendix A.4. In general, the optimized solution has larger skin thickness at the whole structure, larger spar thickness at the strut and fairing but smaller main spar thickness. The reason is that, to be able to match better the deformation, the optimizer is stiffening the structure. In Figures A.14 and A.15, presented in the Appendix, it can be seen that the resultant structure is stiffer in the three displacements (x,y,z), also in sweep and bending angles at the strut and first main wing part. However, it is more flexible in twist at the whole structure, but not at the tip where it has the same twist value than the baseline distribution.

To conclude the unconstrained optimization, the deformation computed with the optimized thickness distribution gets values that match considerably the LF deformation, being lower than 10% the maximum difference between the High and Low-Fidelity models in all the displacements and rotations but not the twist where the maximum difference is 17% at the tip. In addition, the maximum stress value computed with the optimized thickness distribution exceeds the stress limit, being 2.64 times higher than the one from the LF model. In the following sections it is going to be noted that the maximum stress value is not

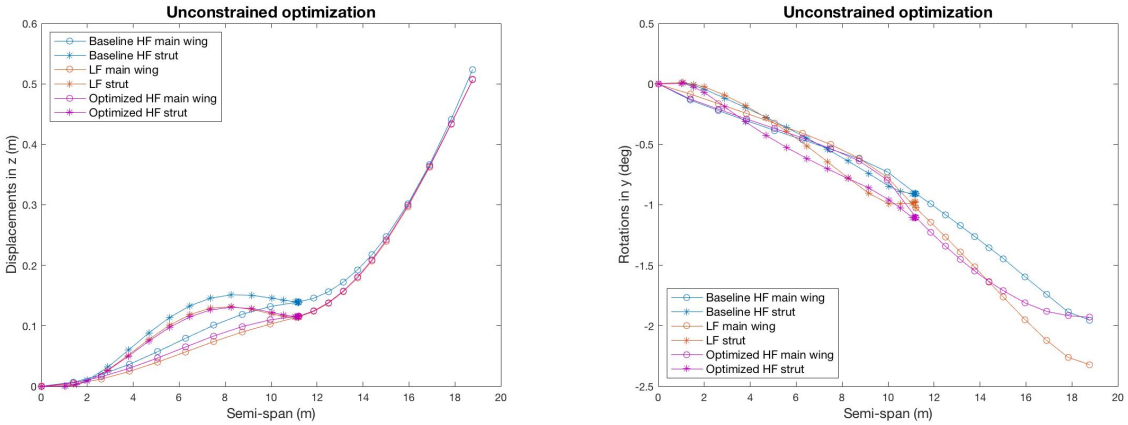

(a) Vertical displacement

(b) Twist

Figure 5.2: Vertical displacement and twist from the unconstrained optimization thickness distribution

going to facilitate the constrained optimization.

5.2 Constrained problem

The objective of this optimization problem is to minimize the structural mass while trying to match the deformation of the Low-Fidelity model for the cruise flight conditions by varying the thickness and its distribution along the main wing and the strut without exceeding a given value of stress for the pull-up maneuver conditions. The constraint equations are defined in Section 4.1.3 and the deformation constraint coefficients (A to F) are defined in Equation 4.13, which were defined after performing the objective function study of the unconstrained optimization. As detailed in Section 4.3.2, these coefficients are percentages that give more importance to some degrees of freedom than to the others. Moreover, the objective function is detailed in Section 4.1.2. To have a general idea of the margin value, the deformation value, which is g_1 from Equation 4.7, computed with the baseline thickness distribution in cruise flight condition is 0.58, being in this case the margin equal to zero. Consequently, if a margin higher than 0.58 is put in a constrained optimization, the deformation will match less than the one with the baseline distribution and vice versa.

The changes made in the constrained optimization to try to obtain the best result possible within the limitations are going to be detailed next. First of all, the results of the constrained optimization with the baseline upper and lower boundaries of the design variables described in Table 4.1 and the new set of boundaries that give more freedom to the optimizer are going to be shown. Then, the margin is going to be studied to see the implications of it in terms of mass and stress. Furthermore, it has been included two additional kinks in the main wing thickness distribution, one in each half of it, due to the fact that the results with the bilinear thickness distribution seem to limit the optimizer which is explained later.

Baseline bounds results

First of all, the constrained optimization has been computed with the baseline bounds defined in Table 4.1 and with a margin of 3 (m=3 in Equation 4.7), which allows to have a worse match in deformation than the one shown in Section 4.5 where the High and Low-Fidelity model results are compared. This optimization ended up converging to an infeasible point since the stress and deformation constraints could not be satisfied at the same time. Another optimization was performed with the Baseline bounds without the deformation constraint, which is equivalent to put a huge margin to have always a negative value in this constraint, to see if the margin was over constraining the optimization. The result of it was that the optimizer could not find a point within the feasible region that satisfied the stress constraint. The results from this latter optimization are the ones shown in this section. The skin and spar thickness distributions resultants of the optimization are shown in Figure 5.3. In addition, the vertical displacement and twist are plotted in Figure 5.4, while the rest of displacements and rotations are presented in the Appendix A.5.

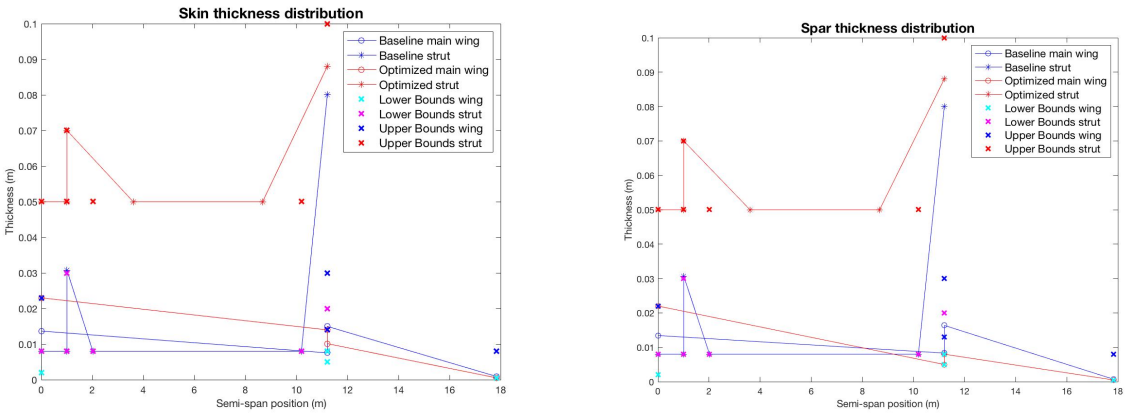

(a) Skin (b) Spar

Figure 5.3: Thickness distribution from the Constrained optimization with the baseline bounds

Figure 5.3 plots the baseline thickness distribution together with the optimized one with the baseline bounds. For a better understanding of the result provided by the optimizer, the upper and lower bounds have also been plotted. It can be observed in Figure 5.3 that the skin and spar thicknesses at the fairing and strut areas have their maximum value, but not at the joint, where its value is larger than the baseline one but does not reach the upper bound. It has to be highlighted that in both, skin and spar distributions, the strut-kink is located at its lower bound because, in this way, the amount of material at the joint is higher than if the kink was located in the upper bound. As a result, the joint is stiffer and the total structural mass is larger. Furthermore, the first half of the main wing has also the maximum thickness values at the root and in the kink skin but not in the kink spar where the thickness value has its minimum value. However, the second half of the main wing has the minimum values at both kink and tip.

From the previous thickness distribution, where the optimizer tries to stiffen the structure by putting

the maximum values allowable in the whole structure until the kink, including the fairing and strut, and the minimum values from the main wing-kink to the tip, it is expected to have lower deformation than for the baseline thickness distribution. If Figure 5.4 is observed, it can be seen that the areas that have the maximum thickness values allowable have lower vertical displacements than the baseline and the ones that have the minimum values allowable have higher vertical displacements. However, the twist in the whole structure is lower with the optimized thickness distribution than with the baseline one. The rest of the displacements and rotations, which are presented in the Annex in Figures A.17 and A.18, are significantly lower with the optimized thickness distribution than with the baseline one, but not for the bending which shows larger values in the outboard part of the main wing. These deformation results are consistent with the thickness distribution shown previously, but they do not match at all the LF model deformation. It is believed that giving the optimizer more freedom, i.e. by increasing the upper bounds and decreasing the lower bounds which is studied later, can result in a better solution.

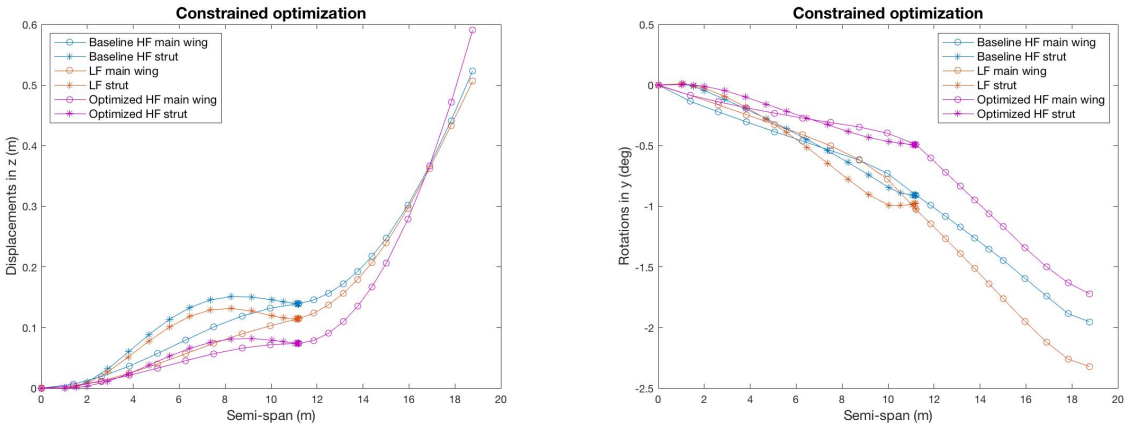

(a) Vertical displacement

(b) Twist

Figure 5.4: Results from the Constrained optimization thickness distribution with the baseline bounds

In Table 5.2 are presented the structural mass and maximum stress values together with the maximum High and Low-Fidelity differences in vertical displacement, bending and twist for the baseline and optimized thickness distributions, as indicated in the table heading. For a better understanding of the magnitudes from the differences in the vertical displacement and rotations, the LF results have also been included in the table. It should be reminded that in the constrained optimization the stress is constrained for the maneuver flight conditions, but the deformation is compared for the cruise conditions, which is the reason why all the values from Table 5.2, except the stress, are equal to the ones shown previously in the Unconstrained optimization. The structural mass, as may be noticed, is much higher (212%) than the one from the baseline thickness distribution. However, the maximum stress exceeds slightly (7%) the limit allowable, although the stress reduction is considerable, being 220MPa lower than the baseline one. As expected, the differences in deformation are huge, being the twist shown in Figure 5.4 the degree of freedom that better matches the Low-Fidelity model. The difference in vertical displacement is 15 times the Baseline one and the bending is 10, while the twist is only 1.5.

Thickness distribution	Structural weight $[kg]$	Stress max $[MPa]$	Vertical displacement $[m]$ max($\|HF-LF\|_z$)	Bending $[^\circ]$ max($\|HF-LF\|_{\theta_x}$)	Twist $[^\circ]$ max($\|HF-LF\|_{\theta_y}$)
Baseline	1928.5	505	0.0295	0.7485	0.3799
Optimized	4086.94	285	0.4540	7.0946	0.5652
	Structural weight $[kg]$	Stress max $[MPa]$	Vertical displacement at tip $[m]$	Bending at tip $[^\circ]$	Twist at tip $[^\circ]$
Low-Fidelity	1636	268	0.5063	3.8474	2.3222

Table 5.2: Constrained optimization thickness distribution results with the baseline bounds

The element and nodal stress solutions from Ansys are shown in Figure A.19 in the Annex due to the maximum stress value being located at the root, as happens with the baseline thickness distribution. As the element and nodal solutions do not provide the same maximum value, existing a 5MPa difference between them, the value taken into account is the one from the element solution (285MPa) for the reasons explained before in Section 4.4.

New bounds

For the reasons mentioned in the previous section, where the constraint optimization has been computed with the initial set of bounds, the range of values that the optimizer can select for the design variables has been broadened. The effect of it on the constrained optimization is going to be shown in this section. The optimization computed has the same objective and constraint functions, being the bounds and margin the parameters changed. In Table 5.3 are shown together the old and new bounds of the design variables. The description of each variable can be found in Table 4.1, where the old bounds are defined. Even though the new upper bounds are larger than the ones expected to be required, these values take into account the airfoils dimensions to have a feasible thickness distribution if one of the design variables results in its upper bound value.

Initially, the optimization was computed with a reasonable margin value (1.5) but as the optimization converged to an infeasible point, the margin was increased up to 2.5 and 3, ending up in the same way. Thus, the deformation constraint was removed to see if a feasible point could be found constraining only the maximum stress. The result was, as in the previous computations, that the optimizer could not find a solution in the feasible region. The results from this latter optimization are the ones shown in this section. The results computed with the different margin values are shown later in the Parametric Study on the Margin Section.

In this section the plots show the constrained optimization results computed with the old and new bounds for comparison purposes. The thickness distribution obtained from the constrained optimization with the new bounds is shown in Figure 5.5. It can be noticed that the strut and fairing do not have thickness values as large as with the older bounds and that its values are slightly lower than the older lower bounds, in both skin and spar. In addition to the strut and fairing, the whole main wing spar exceeds

Variable	New lower bound	Old lower bound	New upper bound	Old upper bound
x_1 $[mm]$	1	2	150	23
x_2 $[mm]$	1	5	34	14
x_3 $[mm]$	1	8	40	30
x_4 $[mm]$	0.1	0.5	30	8
x_5 $[mm]$	1	2	150	22
x_6 $[mm]$	1	5	34	13
x_7 $[mm]$	1	8	30	30
x_8 $[mm]$	0.1	0.5	30	8
x_9 $[mm]$	10	20	100	100
x_{10} $[mm]$	1	8	50	50
x_{11} $[mm]$	10	30	100	70
x_{12} $[\%]$	5	5	25	25
x_{13} $[\%]$	75	75	95	95

Table 5.3: New design variables bounds

the older bounds, being its thickness values higher than the older upper bounds. The main wing skin remains within the old bounds, getting at the root and tip the older upper bound thickness value and at the joint the older lower bound. Increasing the thickness in the spar has lower repercussion in terms of mass than increasing it in the skin, since its cross sectional area is smaller. Furthermore, the thickness value at the joint is significantly lower than the one with the older bounds and the kink is located one meter in the outboard direction of the wing, which is closer to the joint in regard to the old bound set. Both facts contribute to reduce largely the mass whose value is shown in Table 5.4. Since the bounds have been broadened, it is not required to have the maximum values in the strut and fairing, as happens with the older bounds. The optimizer puts more thickness in the areas that have larger stress such as the main wing root and the joint, as expected, while the less stressed areas present thinner thicknesses.

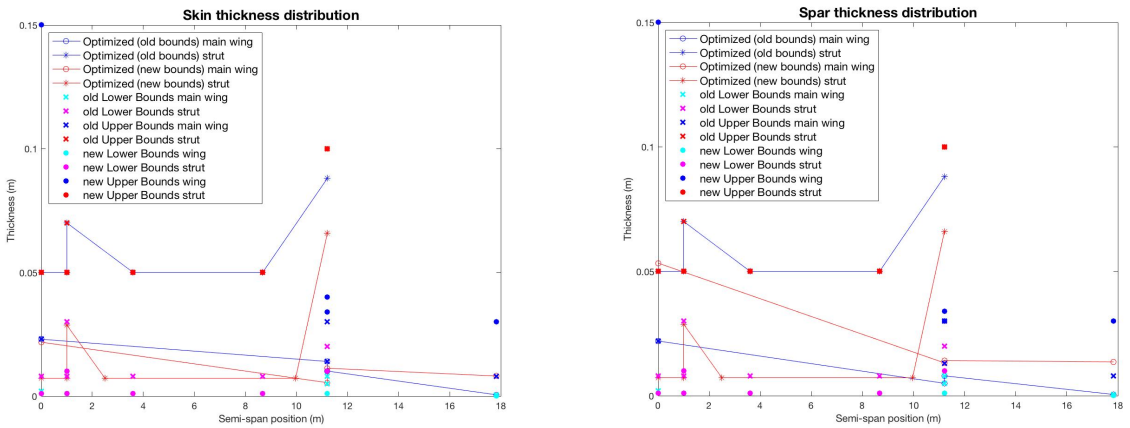

(a) Skin (b) Spar

Figure 5.5: Thickness distribution from the Constrained optimization with the new bounds

In Figure 5.6 are shown the vertical displacement and twist for the cruise flight conditions, since it is the one used in the deformation constraint. As the results shown in Table 5.4 reveal, the vertical displacement matches better with the new bounds but not the twist, where the point with the largest dif-

ference with the LF model occurs at the tip. It should be reminded that, as in the optimization with the old bounds, the optimizer converged to an infeasible point since it was not able to match all the constraints which is the reason why the stress value shown in Table 5.4 exceeds the maximum allowable stress in 88MPa.

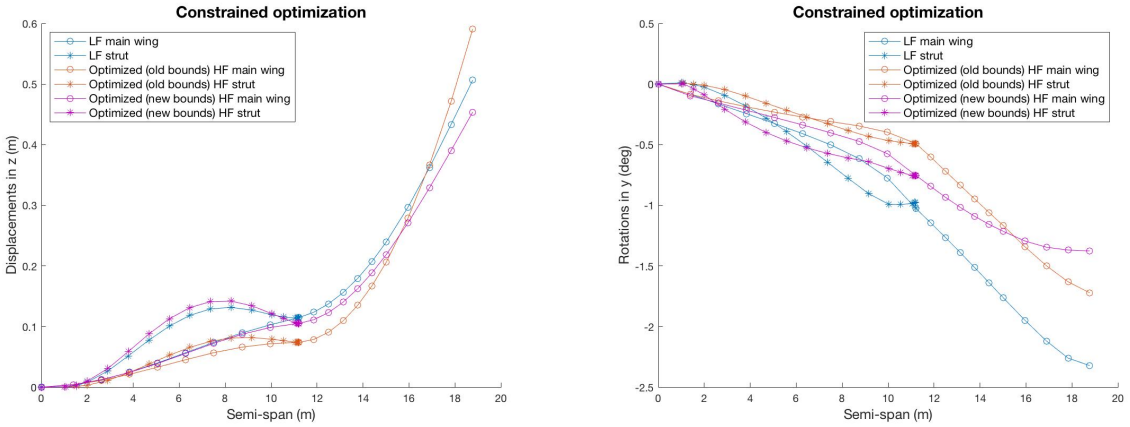

(a) Vertical displacement

(b) Twist

Figure 5.6: Results from the Constrained optimization thickness distribution with the new bounds

Thickness distribution	Structural weight $[kg]$	Stress max $[MPa]$	Vertical displacement $[m]$ max($\|HF-LF\|_z$)	Bending $[°]$ max($\|HF-LF\|_{\theta_x}$)	Twist $[°]$ max($\|HF-LF\|_{\theta_y}$)
Optimized (old bounds)	4086.94	285	0.4540	7.0946	0.5652
Optimized (new bounds)	2523.02	354	0.0844	0.8102	0.9460
	Structural weight $[kg]$	Stress max $[MPa]$	Vertical displacement at tip $[m]$	Bending at tip $[°]$	Twist at tip $[°]$
Low-Fidelity	1636	268	0.5063	3.8474	2.3222

Table 5.4: Constrained optimization thickness distribution results with the old and new bounds

In Figure 5.7 are shown the interior and exterior views of the maximum stress value for the optimization with the new bounds. It can be noted that the maximum stress is located at the strut and that the main wing stress in the skin is within the allowable stress values. Since the stress which exceeds the limit is localized in a small region, coloured in red and orange in (a), this region could be reinforced by changing the aluminium by another stronger material, such as titanium. In this way, the stress constraint will be satisfied. However, the deformation continues being larger than the one desired. For this reason, two additional kinks are going to be introduced in the main wing to allow for a higher design freedom in the optimization process and, consequently, to better match the deformation between High and Low-Fidelity models.

Added design freedom

This section is going to study if adding two more kinks to the main wing thickness distribution allows to obtain a feasible solution for the constrained optimization. As it has been mentioned previously, even

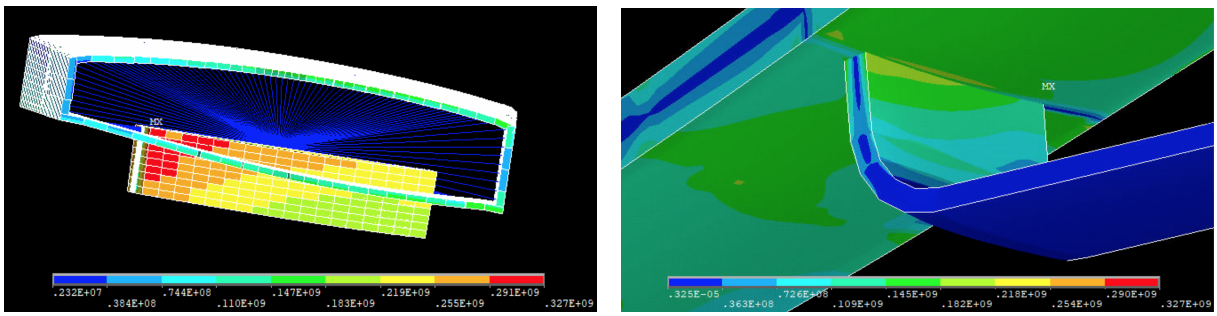

(a) Interior view of the joint

(b) Exterior view of the joint

Figure 5.7: Von Misses maximum stress location from the Constrained optimization with the new bounds

if the deformation is a constraint of the optimization, providing a bigger margin in Equation 4.7 allows the optimizer to give a solution even if the deformation between the High and Low-Fidelity models do not match very well. It should be remembered that the Baseline thickness distribution presents the maximum stress value at the main wing root and a high stress area at the areas around the joint, which are shown in Figure A.9. In the thickness distribution plots shown in Figure 5.1, it can be seen that the thickness has been increased significantly at the joint in a small region of the span. The result of it is that the localized high stress is reduced without increasing significantly the mass.

From the previous constrained optimizations, it can be concluded that, the two areas that have higher stress values are the main wing root and the joint, thus the optimizer puts higher thickness values at these points which are the beginning and end of the first main wing linear distribution (inboard part of the wing). Consequently, the mass is increased to be able to satisfy the stress constraint. As a localized stress reduction is needed and it is not desired to increase substantially the mass with respect to the baseline mass, it is considered necessary to modify the thickness distributions to give more freedom to the optimizer to find a solution within the feasible region. For instance, the kink located at the joint gives the freedom to the optimizer to increase the thickness in a small part of the strut in the spanwise direction. In order to avoid the significant mass increase in addition to give more design, two additional kinks have been included.

As a result of adding more segments to the thickness distribution, it is needed to add more design variables to the ones previously defined in Table 4.1. The new design variables correspond to the skin and spar thickness at the new kinks and the location of these two kinks along the span. The design variables used in the optimization described in this section, which includes the old variables and the new ones, are shown in Table 5.5. It is worth to mention that the new boundaries defined in the previous section are also used in this section, since they provide better results than the older ones, as discussed previously.

As in the optimizations with the old and new bounds discussed previously, this optimization ended up converging to an infeasible point. This is due to the fact that the optimizer is not able to satisfy all

Variable	Lower bound	Upper bound	Description
x_1 $[mm]$	1	150	Skin thickness at the root
x_2 $[mm]$	1	34	Skin thickness at the joint inboard
x_3 $[mm]$	1	40	Skin thickness at the joint outboard
x_4 $[mm]$	0.1	30	Skin thickness at the tip
x_5 $[mm]$	1	150	Spar thickness at the root
x_6 $[mm]$	1	34	Spar thickness at the joint inboard
x_7 $[mm]$	1	30	Spar thickness at the joint outboard
x_8 $[mm]$	0.1	30	Spar thickness at the tip
x_9 $[mm]$	10	100	Strut thickness at the joint
x_{10} $[mm]$	1	50	Main strut thickness
x_{11} $[mm]$	10	100	Strut thickness at the fairing
x_{12} $[\%]$	5	25	Kink position at the joint measured as strut length %
x_{13} $[\%]$	75	95	Kink position at the fairing measured as strut length %
x_{14} $[mm]$	1	150	Skin thickness at the first kink inboard
x_{15} $[mm]$	1	150	Skin thickness at the first kink outboard
x_{16} $[m]$	0	10	Skin first kink position measured as span length
x_{17} $[mm]$	1	150	Spar thickness at first kink inboard
x_{18} $[mm]$	1	150	Spar thickness at first kink outboard
x_{19} $[m]$	0.01	10	Spar second kink position measured as span length
x_{20} $[mm]$	0.1	30	Skin thickness at the second kink inboard
x_{21} $[mm]$	0.1	30	Skin thickness at the second kink outboard
x_{22} $[m]$	10.70	18.77	Skin second kink position measured as span length
x_{23} $[mm]$	0.1	30	Spar thickness at second kink inboard
x_{24} $[mm]$	0.1	30	Spar thickness at second kink outboard
x_{25} $[m]$	10.70	18.77	Spar second kink position measured as span length

Table 5.5: Optimization design variables - additional kinks

the prescribed constraints, which are to not exceed the maximum stress allowable and to match the LF deformation with a margin = 3. It should be reminded that, having a margin = 3 in deformation allows to have a different deformation between the High and Low-Fidelity models. Anyway, the results of the optimization are going to be discussed to see if there is an improvement in the solution with the two additional kinks. The new thickness distribution with the two additional kinks, each one located at each half of the main wing, computed in the optimization is shown in Figure 5.8. This image shows the results from three different optimizations, each one with a different margin (1.5, 2.5 and 3) but only the results with a margin = 3 are going to be discussed in this section. The effect of the margin in the optimization results are going to be discussed in the following section where the parametric study on the margin is described.

Figure 5.8 shows that the thickness value at the root in both, skin and spar, is significantly higher than the baseline one. As the main wing root together with the joint are areas with higher stress values, the thickness there should be larger than in the rest of the areas. It can be observed that the first additional kink is located near the main wing root, being the thickness step considerably large. It allows to reduce the high stress values at the root without increasing significantly the mass. The step of the second kink is very small, but it allows to have a larger thickness at the kink and smaller at the joint and tip; thus allowing to stiffen the middle areas of the second segment of the main wing with a lower overall mass. The main wing joint presents larger thickness values to reinforce this area. Regarding the fairing and strut skin and spar distributions, it can be said that it does not show big differences. The fairing has larger values and the strut kink is located before the baseline one in the span direction, which

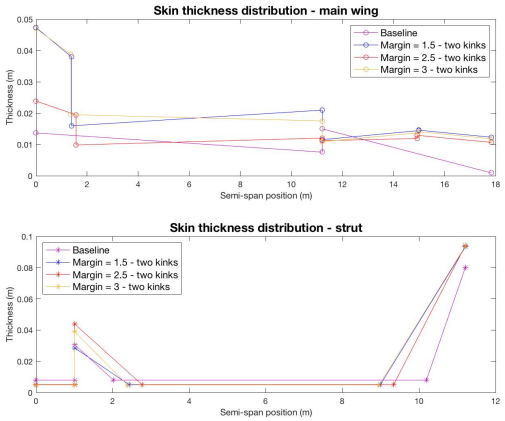

(a) Skin

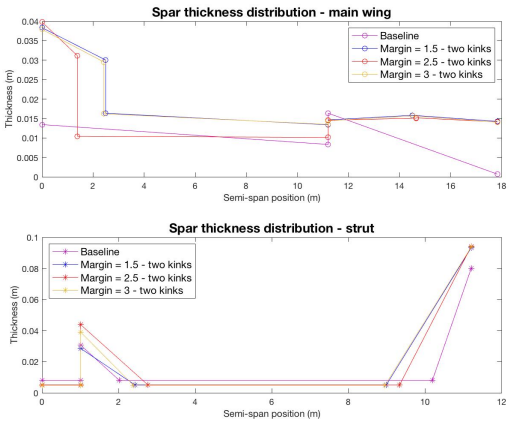

(b) Spar

Figure 5.8: Thickness distributions from the Constrained optimization with two additional kinks

make them stiffer as shown in Figure 5.9. These skin and spar thickness distributions end up stiffening the structure more than required to match the LF model deformation, as shown in Figure 5.9 where the vertical displacement and the twist are shown. In these plots it can be seen that both, displacement and rotation, have lower values in the additional kinks results than in the LF ones, being larger the differences in the latter where the tip has less than half of the Low-Fidelity twist.

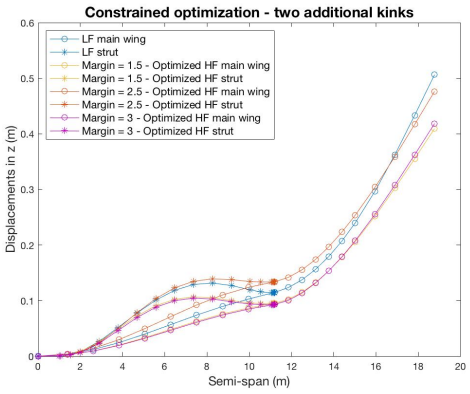

(a) Vertical displacement

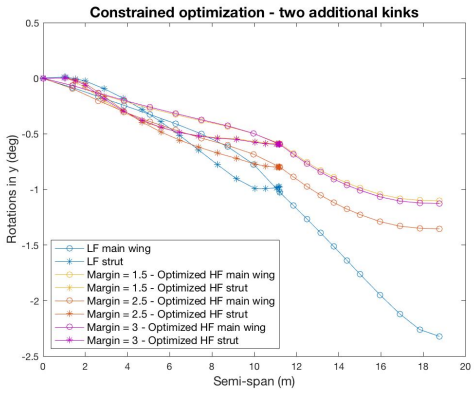

(b) Twist

Figure 5.9: Results from the Constrained optimization thickness distribution with the two additional kinks

Table 5.6 shows the mass and maximum stress results in addition to the differences in vertical displacement, bending and twist between the optimization results and the LF ones. The results from this section are shown together with the parametric study results to avoid repeating information and to see the additional kinks effect when the margin is changed. In Table 5.6, if the row ”margin = 3 (+2 kinks)” is observed, it can be noticed that the stress constraint is almost satisfied, but the differences in deformation are very large, as shown in Figure 5.9. The vertical displacement and twist differences from the table are located at the tip. The maximum stress is located at the strut near the fairing, as shown in the Appendix Figure A.23 where the nodal stress solution is plotted by Ansys.

In addition to the optimizations discussed in the last two sections, which use the algorithm Interior-Point, it has been tried the SQP algorithm for the optimization with the two additional kinks to confirm that it cannot provide a feasible solution either. Since the SQP is an algorithm that tries first to minimize the objective function and then it tries to reach a feasible solution, as mentioned in Section 4.2, the optimizer could not find a feasible solution, as it was expected. The results from this optimization are not going to be shown as they do not satisfy both constraints at all.

From this optimization and the ones with old and new bounds discussed in the last two sections, it can be concluded that the optimizer does not have enough freedom to provide a feasible solution. None of the constraints is satisfied in the constrained optimizations shown so far. A new optimization problem is going to be defined to try to get a feasible solution.

Parametric study on the Margin

If the High and Low-Fidelity deformations match, the margin required in the deformation constraint would be zero. Ideally, the difference in deformation between both models should be lower than 10%, which does not happen in any of the constrained optimizations discussed up to now. The parametric study in the margin consists in increasing the margin to evaluate its impact on mass and stress. Initially, the margin was reduced to 1.5, converging to an infeasible point. After computing the optimizations with margin = 1.5 and get an infeasible point solution, it has been decided to increase the margin up to 3 to see if the optimizer could get a feasible solution but it did not. Further optimizations with different margins have not been computed since this latter do not match at all the LF solution. It should be reminded that in the stress constraint a margin cannot be added due to the stress limit required to ensure a safe flight.

The deformation constraint that includes the margin is shown in Equation 4.7. Even if the optimizations did not converge to a feasible point, the results are going to be shown in Table 5.6, which includes the optimization results from the new bounds and the ones with the two additional kinks, described previously. It can be noted from Table 5.6 that none of the maximum stress values satisfies the stress constraint, which is to not exceed the value of 266MPa.

When the results from Table 5.6 are observed, it can be noted that the structural mass is inversely proportional to the maximum stress value. Furthermore, when the margin is increased the stress values are also larger, but not in the case of two additional kinks with margin = 3. The differences in deformation between the High and Low-Fidelity models do not show a clear trend when the margin is increased or reduced. In all the cases discussed up to now, the optimizer is not capable to find a solution for the design variables within its boundaries that satisfy all the constraints, being the mass values shown in Table 5.6 not minimized.

1.5	3315.70	280	Strut near fairing	0.1062	0.7251	1.2018
1.5 (+2 kinks)	3135.54	296	Strut near fairing	0.0969	0.8897	1.2194
2.5	3056.03	346	Strut near joint	0.0629	0.5067	1.0333
2.5 (+2 kinks)	2464.40	414	Main wing near root	0.0301	0.6397	0.9677
3	1876.08	612	Main wing root	0.0592	0.8473	0.8029
3 (+2 kinks)	3247.99	289	Strut near fairing	0.0879	0.7808	1.1952

Table 5.6: Parametric study on the Margin - Constrained optimization

In conclusion, it can be said that there even if the margin is increased, using the Interior-Point algorithm, the optimizer could not get a solution that satisfies the stress constraint by minimizing the mass. Since it has not been able to match the deformation by increasing the bounds and adding kinks, a new optimization with different objective and constraint functions is going to be defined.

5.3 Jig shape optimization

As it has been shown in the constrained optimization results along Section 5.2, it has not been possible to find a feasible solution for the constrained problem defined. It is thought that changing the initial main wing twist distribution, which means changing the geometry during the optimization, will help to match the final shape of the High and Low-Fidelity models. It has to be reminded that the strut does not have an initial twist distribution. Since it is desired to have the same twist as the Low-Fidelity model when the structure is loaded, if the optimizer is able to modify the initial twist distribution, the High-Fidelity twist from the optimized structure is expected to be closer than the ones from previous optimizations. The importance to match the deformation comes from having the same deformed shape to get the same lift distribution in both models.

5.3.1 Optimization Problem Statement

The statement of this new optimization problem is to match the Low-Fidelity deformation in cruise flight conditions, which is matching the displacements and rotations in the three axes, by varying the thickness and its distribution along the main wing and the strut in addition to varying the main wing twist distribution without exceeding a given value of stress and structural mass in pull-up maneuver conditions.

5.3.2 Design Variables

The design variables of the optimization problem are the skin and spar thickness distributions of the main wing and strut, the kink position of the strut at the fairing and at the joint between the main wing and strut, the two kink positions at the main wing in addition to the main wing twist distribution. The total amount of design variables is 35, being the first 25 the design variables from the constrained optimization with two additional kinks shown in Table 5.5. The new design variables added in this optimization are

the twist at each main wing airfoil. To avoid confusing the reader, all the design variables as well as their lower and upper bounds are detailed in Table 5.7, even if the first 25 have already been defined previously.

Variable	Lower bound	Upper bound	Description
x_1 $[mm]$	1	150	Skin thickness at the root
x_2 $[mm]$	1	34	Skin thickness at the joint inboard
x_3 $[mm]$	1	40	Skin thickness at the joint outboard
x_4 $[mm]$	0.1	30	Skin thickness at the tip
x_5 $[mm]$	1	150	Spar thickness at the root
x_6 $[mm]$	1	34	Spar thickness at the joint inboard
x_7 $[mm]$	1	30	Spar thickness at the joint outboard
x_8 $[mm]$	0.1	30	Spar thickness at the tip
x_9 $[mm]$	10	100	Strut thickness at the joint
x_{10} $[mm]$	1	50	Main strut thickness
x_{11} $[mm]$	10	100	Strut thickness at the fairing
x_{12} $[\%]$	5	25	Kink position at the joint measured as strut length %
x_{13} $[\%]$	75	95	Kink position at the fairing measured as strut length %
x_{14} $[mm]$	1	150	Skin thickness at the first kink inboard
x_{15} $[mm]$	1	150	Skin thickness at the first kink outboard
x_{16} $[m]$	0	10	Skin first kink position measured as span length
x_{17} $[mm]$	1	150	Spar thickness at first kink inboard
x_{18} $[mm]$	1	150	Spar thickness at first kink outboard
x_{19} $[m]$	0.01	10	Spar second kink position measured as span length
x_{20} $[mm]$	0.1	30	Skin thickness at the second kink inboard
x_{21} $[mm]$	0.1	30	Skin thickness at the second kink outboard
x_{22} $[m]$	10.70	18.77	Skin second kink position measured as span length
x_{23} $[mm]$	0.1	30	Spar thickness at second kink inboard
x_{24} $[mm]$	0.1	30	Spar thickness at second kink outboard
x_{25} $[m]$	10.70	18.77	Spar second kink position measured as span length
x_{26} $[deg]$	0	5	Initial twist of the first main wing airfoil
x_{27} $[deg]$	-0.5	5	Initial twist of the second main wing airfoil
x_{28} $[deg]$	-3	5	Initial twist of the third main wing airfoil
x_{29} $[deg]$	-3	5	Initial twist of the fourth main wing airfoil
x_{30} $[deg]$	-3	5	Initial twist of the fifth main wing airfoil
x_{31} $[deg]$	-3	5	Initial twist of the sixth main wing airfoil
x_{32} $[deg]$	-3	5	Initial twist of the seventh main wing airfoil
x_{33} $[deg]$	-3	5	Initial twist of the eighth main wing airfoil
x_{34} $[deg]$	-3	3	Initial twist of the ninth main wing airfoil
x_{35} $[deg]$	-3	3	Initial twist of the tenth main wing airfoil

Table 5.7: New Optimization design variables

5.3.3 Objective function

The objective of the optimization is to minimize the differences in deformation between both models. For practicality reasons, it has been used the same function defined as deformation constraint in the constrained optimization which is shown down below in Equation 5.1, where m is equal to 1. The value of this number is not relevant for the convergence of the optimization described in this section as it was in the previous constrained optimization where the value of g_1 had to be negative to satisfy the deformation constraint. It has been decided to define m = 1 to facilitate the understanding of the output values that the software computes during the optimization process.

$$f_1(x) = 0.05 \cdot max(|\frac{\Delta x - \Delta x_0}{\Delta x_0}|) + 0.05 \cdot max(|\frac{\Delta y - \Delta y_0}{\Delta y_0}|) + 0.05 \cdot max(|\frac{\Delta z - \Delta z_0}{\Delta z_0}|) + \\ + 0.25 \cdot max(|\frac{\Delta \theta_x - \Delta \theta_{x_0}}{\Delta \theta_{x_0}}|) + 0.4 \cdot max(|\frac{\Delta \theta_y - \Delta \theta_{y_0}}{\Delta \theta_{y_0}}|) + 0.2 \cdot max(|\frac{\Delta \theta_z - \Delta \theta_{z_0}}{\Delta \theta_{z_0}}|) - m \quad (5.1)$$

In the same way as the previous optimizations, the beam nodes located at the main wing root and fairing together with the following beam node in the outboard direction are not used to compute in Matlab the objective function shown in Equation 5.1. The reason is that they have zero or nearly zero displacement and rotation, so a slight difference between High and Low-Fidelity will result in a big value. As some other beam nodes have small values in some of the displacements or rotations, the differences are only computed at the wing tip to check if a better solution can be provided by the optimizer. It has been selected the tip beam node due to the fact that largest displacements and rotations are found there. The objective function for this optimization is shown in Equation 5.2 down below where m = 1.

$$f_2(x) = 0.05 \cdot (|\frac{x_{tip} - x_{0_{tip}}}{x_{0_{tip}}}|) + 0.05 \cdot (|\frac{y_{tip} - y_{0_{tip}}}{y_{0_{tip}}}|) + 0.05 \cdot (|\frac{z_{tip} - z_{0_{tip}}}{z_{0_{tip}}}|) + \\ + 0.25 \cdot (|\frac{\theta_{x_{tip}} - \theta_{x_{0tip}}}{\theta_{x_{0tip}}}|) + 0.4 \cdot (|\frac{\theta_{y_{tip}} - \theta_{y_{0tip}}}{\theta_{y_{0tip}}}|) + 0.2 \cdot (|\frac{\theta_{z_{tip}} - \theta_{z_{0tip}}}{\theta_{z_{0tip}}}|) - m \quad (5.2)$$

5.3.4 Constraints

The constraints used to define the feasible region in this optimization problem are inequality constraints which means that each constraint function has to be lower than or equal to a given value. The constraints are the stress (σ), that should not exceed the maximum yield stress (σ_{max}) of the material (266MPa), and the structural mass (M), that should not exceed 220% of the Low-Fidelity mass (M_0 + 3600kg). This percentage could seem very high, but the reality is that the Baseline thickness distribution used in the LF model (1928.5kg) does not support the high stress of the pull-up maneuver load and the previous constrained optimization showed that a big increase in mass is necessary to support the pull-up maneuver load. This latter observation has been further described in Section 4.5. Consequently, a large mass margin is required to be able to satisfy the stress constraint. Both stress and mass constraints are defined in Equations 5.3 and 5.4 down below.

$$g_1 = \frac{\sigma - \sigma_{max}}{\sigma_{max}} \quad (5.3)$$

$$g_2 = \frac{M - M_0}{M_0} - 2.2 \quad (5.4)$$

It should be highlighted that the mass constraint is required to limit the amount of material. The more mass the optimizer puts in the structure, the more rigid it will be. As it has been shown in the previous constrained optimization, the solutions provided by the optimizer tend to stiffer structures than

the Low-Fidelity one to satisfy the stress constraint.

5.3.5 Optimization results

In Table 5.8 are shown the results of the new optimizations performed and the ones of the LF model. The thickness distribution ”Optimized 1” and ”Optimized 3” have been computed with the objective function that compares the High and LF deformations at all the beam nodes, defined in Equation 5.1. However, ”Optimized 2 - interior point” and ”Optimized 2 - SQP” have been computed with the one that compares only the deformation at the tip, defined in Equation 5.2. Regarding the constraints, all of them were constrained with Equation 5.3 and 5.4, but not ”Optimized 3” which allowed to have 2045kg as maximum structural mass which is 125% of the LF structural mass. All the thickness distributions are computed with the algorithm interior point except for ”Optimized 2 - SQP”, which uses the SQP algorithm as its name suggests. The reason to try the same optimization with both algorithms is to see if the SQP can provide a better solution than the interior point one, since the optimization with the interior point algorithm converged to a feasible point. As the results of Table 5.8 suggest, the optimization with the SQP algorithm converged to an infeasible point so this optimization is not displayed in the plots.

Initially, the idea was to constraint the mass up to 2045kg to not increase it too much in respect to the baseline thickness distribution. After checking the results provided by ”Optimized 3”, it was considered necessary to increase the mass allowable to the value shown in Equation 5.4 to be able to satisfy the stress constraint. With this value the optimizer adds more mass to reduce the maximum stress but, consequently, the structure is stiffer and the deformation matching is worse. In Table 5.8 it can be seen that ”Optimized 3” presents the thickness distribution that has the best twist values, being the differences between the High and Low-Fidelity twist lower than 12%. However, the maximum stress is 454MPa, which exceeds in 1.7 times the limit, so it is not a feasible solution even if the goal of the optimization is to match the deformation. This is the reason why this thickness distribution is not shown in the following graphs.

”Optimized 1” and ”Optimized 2 - interior point” are the only thickness distributions converged to a feasible solution, since they satisfy the stress and mass constraints. As mentioned at the beginning of this section, the former minimizes the differences in deformation at all the beam nodes and the latter minimizes the differences in deformation just at the tip. If the vertical displacement, bending and twist differences shown in Table 5.8 are observed, it can be seen that the optimization that minimizes the differences at the tip provides a better solution, being the values smaller. Furthermore, the structural weight of ”Optimized 2 - interior point” is approximately 1000kg lighter than the ”Optimized 1” one, being both maximum stress values within the limit.

In Figure 5.10 are shown ”Optimized 1” and ”Optimized 2 - interior point” thickness distributions, since they are the only ones that provide a feasible solution, from a stress perspective. They are shown

Thickness distribution	Structural weight $[kg]$	Stress max $[MPa]$	Vertical displacement $[m]$ max($\|HF - LF\|_z$)	Bending $[°]$ max($\|HF - LF\|_{\theta_x}$)	Twist $[°]$ max($\|HF - LF\|_{\theta_y}$)
Optimized 1	4803.91	251	0.1933	1.5102	1.4588
Optimized 2 - interior point	3830.51	265	0.0558	0.6468	1.0953
Optimized 2 - SQP	5290.66	306	0.0953	0.7748	1.3521
Optimized 3	2096.49	454	0.3605	4.4583	0.2638
	Structural weight $[kg]$	Stress max $[MPa]$	Vertical displacement at tip $[m]$	Bending at tip $[°]$	Twist at tip $[°]$
Low-Fidelity	1636	268	0.5063	3.8474	2.3222

Table 5.8: Jig shape optimization thickness distribution results

in the legend as "Deformation at beam nodes" and "Deformation at tip", respectively. It can be seen that "Optimized 2 - interior point" in both, skin and spar, has a larger step in the distribution than "Optimized 1", being the kinks located in a more outboard position than the latter. Furthermore, the spar of "Optimized 2 - interior point" has larger thickness values in the inboard part of the main wing than "Optimized 1", but not in the skin, where the latter has larger values along the whole main wing and, as a consequence, a heavier structure. The fact of adding less material in the skin of the outboard part of the wing makes it more flexible, so it can match better the LF vertical displacement and twist, as Figure 5.11 shows. Regarding the strut thickness, "Optimized 1" presents larger values at the end of the fairing and joint, but lower values at the beginning of the fairing and main strut thickness in both skin and spar. Moreover, it locates both kinks nearer to the root in the inboard direction than "Optimized 2 - interior point". The fact that "Optimized 2 - interior point" puts lower thickness values at the joint makes it more flexible so the twist value there matches better the LF model, as mentioned previously. Both thickness distributions and the location of their kinks are consistent with the maximum stress locations, being at the joint the maximum stress value of "Optimized 2 - interior point" and at the strut near the fairing the one of "Optimized 1", as shows Figure A.26 in the Appendix.

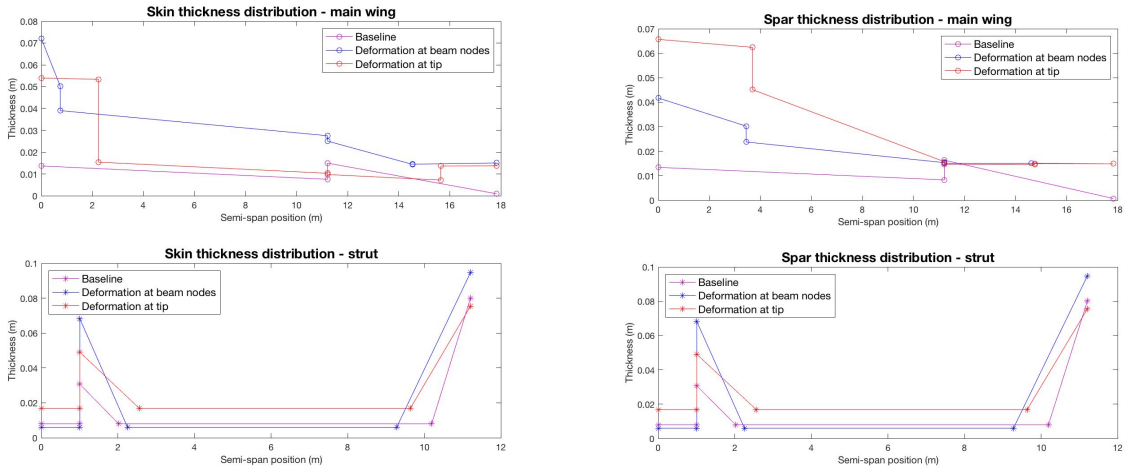

(a) Skin (b) Spar

Figure 5.10: Thickness distributions from the jig shape optimization

In Figure 5.10 are shown the vertical displacement and twist of both thickness distributions. It can be seen that the one that compares the deformation at the tip matches better both vertical displacement and twist. Nevertheless, the differences are higher than 10% at the tip, being higher in twist (47%) than in vertical displacement (11%).

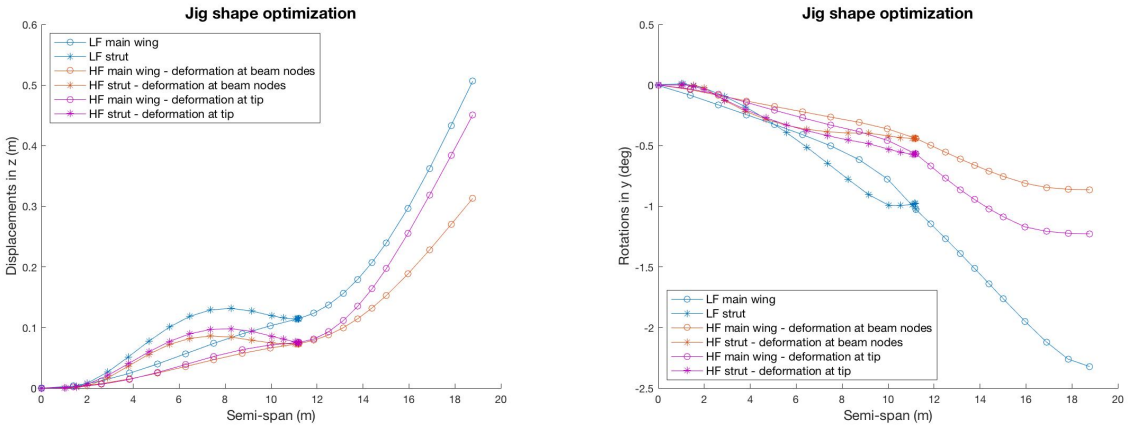

(a) Vertical displacement

(b) Twist

Figure 5.11: Vertical displacement and twist from the jig shape optimization thickness distribution

In Figure 5.12 are represented the baseline and ”Optimized 2 - interior point” twist distributions together with the upper and lower bounds that constraint the twist design variables shown in Table 5.7. It can be noted that the optimized twist distribution has larger values than the baseline one, being the twist at the last two airfoils at the tip almost coincident. In the inboard part until the joint, which is located at 11m of the span, the twist distribution is approximately linear. In the outboard part of the joint, the angle is increased almost two degrees with respect to the one at the joint and then, it decreases smoothly until the last two airfoils, where there is a step and the twist has similar values to the baseline distribution.

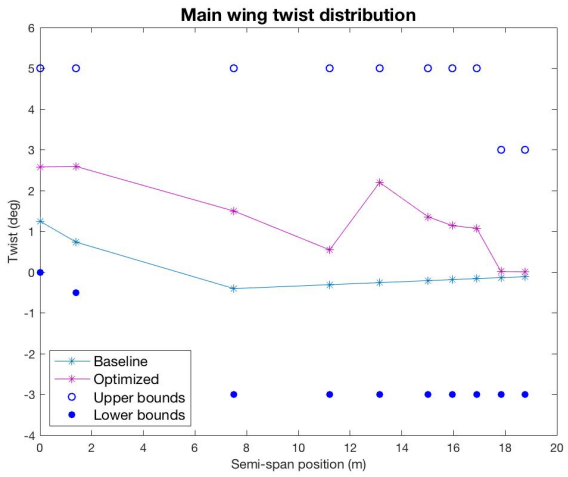

Figure 5.12: Main wing twist distribution from the jig shape optimization

Although the jig shape optimization improves the solution with respect to the previous constrained

optimization detailed in Section 5.2, it has not been able to find a solution that matches the LF deformation within the stress limits. From the jig shape optimization results can be concluded that the optimizer provides a feasible solution in terms of stress, however the main goal of the optimization, that is matching the LF deformation, is not fulfilled because the differences in deformation between the High and Low-Fidelity are higher than 10%.

Chapter 6

Conclusions

6.1 Achievements

This master thesis focuses on comparing the structural and shape optimization of a High and Low-Fidelity structural models for the purpose of validating the Low-Fidelity one. It performs the structural and shape optimization in a High-Fidelity model to match the deformation resulting from the application of a predetermined cruise load to the Low-Fidelity model for a SBW configuration. The design parameters considered relevant to compare both models are vertical displacement, twist, structural mass and the Von Misses stress resulting from applying the aerodynamic loads.

To make the optimization possible, it was imperative to use condensed load files provided by the Low-Fidelity model instead of the distributed ones. An assessment between applying the loads at the beam nodes instead of applying them on the skin and between reading them from a condensed file instead of a distributed one concluded that the results obtained with the new condensed load file are reliable. There were differences found only in twist which show that the condensed load twists less the wing than the distributed one, but the differences are within the admissible values (12.8% in cruise). The stress results obtained from both files have slight differences, being the ones from the condensed files the less accurate ones, but they are still representative of the load case solved in both optimization problems. The results computed using the condensed load files speed up in two orders of magnitude the solving time which made the optimization process feasible.

There are several results worth summarizing from the comparison between High and Low-Fidelity models. The main wing and strut stress values were underestimated by the Low-Fidelity model, while the stress at the main wing-strut joint for both flight conditions was overestimated. The High-Fidelity model maximum stress is 1.91 higher than the one computed by the Low-Fidelity one. These differences were not expected and they made the optimization process difficult as the maximum stress is one of the constraints. Regarding the deformation, the Low-Fidelity model underestimated the value of the displacements of the Strut-Braced Wing structure, however, the differences are not significant. The high-

est differences are found in vertical displacement (cruise 32.94%) and twist (maneuver 30.05%) at the strut and wing tip, being the differences larger in the maneuver load case than in cruise since the load is larger. It can be concluded that the Low-Fidelity model has an advantage in terms of computational cost, but for both flight conditions the stress was not well estimated. However, all the displacements and rotations, except the twist in the pull-up maneuver, present slight differences but acceptable to get a general idea of the deformation of the SBW structure. The Low-Fidelity model can be used in a preliminary design phase, but not in more advanced phases where a High-Fidelity model should be used to refine the design.

Regarding the unconstrained optimization, the deformation computed with the optimized thickness distribution matches the Low-Fidelity deformation, being all the displacements and rotations within the required tolerances but not the twist, where the outboard part of the main wing exceeds the required tolerances. The mass for the optimized solution is larger than the baseline one since the optimizer stiffens the structure to match better the Low-Fidelity deformation. The maximum stress value from the optimized thickness distribution exceeds the stress limit, being higher than the one from the Low-Fidelity model, hinting to the difficulties in the following optimizations.

The constrained optimization converged to an infeasible point since the optimizer could not find a solution that satisfies the stress constraint and, at the same time, matches the Low-Fidelity deformation. Even broadening the design variables bounds and adding two new kinks to the thickness distribution of the main wing, the optimizer could not provide a feasible solution since, apparently, it does not have enough design freedom. A new optimization with different objective and constraint functions was needed to get a feasible solution.

The jig shape optimization found two feasible solutions in terms of stress, however in terms of deformation both solutions have differences in deformation higher than 10% in comparison with the Low-Fidelity model. Both solutions require heavier structural masses than the one of the Low-Fidelity model, as expected at this point. Although the jig shape optimization improved the solution with respect to the previous constrained optimization, it has not been possible to find a solution that matches the Low-Fidelity deformation within the stress limits.

In the author's opinion, the difficulty to match the deformation within the stress limits stems from the poor stress estimation from the Low-Fidelity model, since it estimates stress values significantly lower than the High-Fidelity. Therefore, either significant stress margins should be added when performing MDO based in LF structural models, or the stress predictive capabilities of such models need to be improved.

6.2 Future Work

Some ideas for further research that may provide a better solution to this problem are detailed next. Is it possible to explore other objective functions and design variables, such as the dihedral angle, to see if the optimizer has more freedom to provide a solution that matches the deformation while satisfying the stress constraint. It is known that the stress constraint will continue difficulting the optimization, however if more design variables that modify the structure are added to the process the deformation might be closer to the Low-Fidelity one, while keeping the added mass as low as possible.

Moreover, other materials, or a combination of them, can be tried to see if the stress can be reduced in the high loaded areas such as the main wing root and the strut joint. If the structure is built with a material with a higher yield stress, the optimizer will be able to reduce the overall stress and maybe it will be able to compute a deformation closer to the Low-Fidelity one.

References

[1] U. Aviation. Aviation benefits: contributing to global economic prosperity, accessed 1 March 2021. URL https://unitingaviation.com/news/economic-development/aviation-benefits-for-a-better-future/.

[2] S. Gudmundsson, M. Cattaneo, and R. Redondi. Forecasting recovery time in air transport markets in the presence of large economic shocks: Covid-19, 2020. URL https://www.researchgate.net/publication/342051795_Forecasting_recovery_time_in_air_transport_markets_in_the_presence_of_large_economic_shocks_COVID-19.

[3] L. Teoh and H. Khoo. Green air transport system: An overview of issues, strategies and challenges. *KSCE J Civ Eng*, 20:1040–1052, 2016. URL https://www.researchgate.net/deref/http%3A%2F%2Fdx.doi.org%2F10.1007%2Fs12205-016-1670-3.

[4] G. Potter. *Conceptual Design of a Strut-Braced Wing Configuration*, 2017. URL http://www.utias.utoronto.ca/wp-content/uploads/2017/09/Potter-Strut_Braced_Wing.pdf.

[5] F. Gern, A. Naghshineh-Pour, E. Sulaeman, R. Kapania, and R. Haftka. Flexible wing model for structural sizing and multidisciplinary design optimization of strut braced wing. *AIAA*, AIAA 2000-1327, 2000.

[6] B. Wainfan. *Design Process: Braced Wings*, 2020. URL https://www.kitplanes.com/design-process-braced-wings/.

[7] F. H. Gern, J. F. Gundlach, A. N.-P. A. Ko, E. Sulaeman, P. A. Tetrault, B. Grossman, R. K. Kapania, W. H. Mason, J. A. Schetz, and R. Haftka. Multidisciplinary design optimization of a transonic commercial transport with a strut-braced wing. *Virginia Polytechnic Institute, State University and University of Florida*, 1999.

[8] M. Bradley, C. Droney, and T. Allen. Subsonic ultra green aircraft research phase ii: volume i–truss braced wing design exploration. *Boeing Research and Technology*, NASA CR-2015-218704, 2015.

[9] G. Carrier, O. Atinault, S. Dequand, J.-L. Hantrais-Gervois, C. Liauzun, B. Paluch, A.-M. Rodde, and C. Toussaint. Investigation of a strut-braced wing configuration for future commercial transport. *Onera, the French Aerospace Lab, France*, 2012.

[10] M. Berci, V. V. Toropov, R. W. Hewson, and P. H. Gaskell. Multidisciplinary multifidelity optimisation of a flexible wing aerofoil with reference to a small uav. *University of Leeds, University of London, Imperial College and University of Durham*, 2014.

[11] T. Robinson, K. Willcox, M. Eldred, and R. Haimes. Multifi-delity optimization for variable-complexity design. *11th AIAA/ISSMO Multidisciplinary Analysis and Optimization Conference, Virginia*, 2006.

[12] X. Sun, J. Ge, T. Yang, Q. Xu, and B. Zhang. Multifidelity multidisciplinary design optimization of integral solid propellant ramjet supersonic cruise vehicles. *National University of Defense Technology, China*, 2019.

[13] S. Choi, J. Alonso, I. Kroo, and M. Wintzer. Multifidelity design optimization of low-boom supersonic jets. *Journal of Aircraft*, 2008.

[14] J. M. Grasmeyer. Multidisciplinary design optimization of a strut-braced wing aircraft. Master's thesis, Virginia Polytechnic Institute and State University, 1998.

[15] J. R. R. A. Martins, G. K. W. Kenway, and T. Brooks. Multidisciplinary design optimization of aircraft configurations—part 2: High-fidelity aerostructural optimization. *Lecture series, Von Karman Institute for Fluid Dynamics, Sint–Genesius–Rode, Belgium*, 2016.

[16] L. Cavagna, S. Ricci, and L. Riccobene. Structural sizing, aeroelastic analysis, and optimization in aircraft conceptual design. *Journal of Aircraft*, 48(6), 2011.

[17] S. Ghoman, R. Kapania, P. Chen, D. Sarhaddi, and D. Lee. Multifidelity multistrategy and multidisciplinary design optimization environment. *AAIA*, AIAA 2013-4672, 2013.

[18] R. Liem, C. Mader, E. Lee, and J. Martin. Aero- structural design optimization of a 100-passenger regional jet with surrogate-based mission analysis. *13th AIAA Aviation Technology*, AIAA 2013-4372, 2013.

[19] Y. Zuo, P. Chen, L. Fu, Z. Gao, and G. Chen. Advanced aerostructural optimization techniques for aircraft design. *National Key Laboratory of Aerodynamic Design and Research, Northwestern Polytechnical University, AVIC China Helicopter Research and Development Institute, State Key Laboratory for Strength and Vibration of Mechanical Structures*, 2015.

[20] e. a. C. Kazuhisa. High-fidelity multidisciplinary design optimization of aero-structural wing shape for regional jet. *Springer*, 3410, 2005.

[21] Y. Zuo, Z. Gao, G. Chen, and et al. Efficient aero-structural design optimization: Coupling based on reverse iteration of structural model. *Sci China Tech Sci*, 2015.

[22] A. March and K.Willcox. Constrained multifidelity optimization using model calibration. *Department of Aeronautics & Astronautics, Massachusetts Institute of Technology*, 2012.

[23] N.-V. Nguyen, S.-M. Choi, W.-S. Kim, J.-W. Lee, S. Kim, D. Neufeld, and Y.-H. Byun. Multidisciplinary unmanned combat air vehicle system design using multi-fidelity model. *Aerospace Science and Technology*, 26, 2013.

[24] L. Bonfiglio, P. Perdikaris, J. del Águila, and G. E. Karniadakis. A probabilistic framework for multidisciplinary design: Application to the hydrostructural optimization of supercavitating hydrofoils. *Int J Numer Methods Eng*, 2018.

[25] B. Kumar. An illustrated dictionary of aviation. *New York McGraw Hill*, 2005.

[26] Crane and Dale. Dictionary of aeronautical terms. *Aviation Supplies & Academics*, 1997.

[27] Picture of wright flyer aircraft, accessed 16 February 2021. URL `https://es.wikipedia.org/wiki/Wright_Flyer`.

[28] Rahman, Hammad, and M. Li. Investigation of computational non-linear aeroelastic response of high aspect ratio wing. *Trans Tech Publications*, Applied Mechanics and Materials 419, 2013.

[29] Y. Zhao and H. Hu. Structural modeling and aeroelastic analysis of high-aspect-ratio composite wings. *Institute of Vibration Engineering Research, Nanjing University of Aeronautics and Astronautics, China*, 2004.

[30] K. Ahmad, Z. Wu, and H. Hasham. Fe-modal approach to model geometric nonlinearities of high aspect ratio wing. *Trans Tech Publications*, Applied Mechanics and Materials 390, 2013.

[31] K. Eskandary, M. Dardel, M. H. Pashaei, and A. M. Kani. Effects of aeroelastic nonlinearity on flutter and limit cycle oscillations of high-aspect-ratio wings. *Trans Tech Publications*, 2011.

[32] J. Stankiewicz. Non-linear beam bending of high aspect ratio wing aircraft. Master's thesis, The University of Bristol, 2019.

[33] F. A. Administrator. Weight and balance handbook. *Department of Transportation, U.S*, 2016.

[34] Picture of cessna 180a, accessed 16 February 2021. URL `https://es.wikipedia.org/wiki/Cessna#/media/Archivo:Cessna.180a.g-btsm.arp.jpg`.

[35] N. B. Company. Picture of sugar volt, accessed 16 February 2021. URL `https://www.nasa.gov/topics/aeronautics/index.html`.

[36] G. Farley. Boeing producing battery-powered hybrid plane. *Northwest Cable News*, accessed 16 February 2021. URL `https://archive.is/20130130073137/http:/www.nwcn.com/news/business/boeing-battery-powered-hybrid-plane-99785794.html`.

[37] P. Smith, J. DeYoung, W. Lovell, J. Price, and G. Washburn. A study of high-altitude aircraft strut braced wing of high-aspect ratio. *Kentron International, Inc., an LTV Company*, Hampton Technical Center, Hampton, Virginia, 1981.

[38] W. Pfenninger. Design considerations of large subsonic long range transport airplanes with low drag boundary layer suction. *Northrop Aircraft, Inc.*, Report NAI-54-800 (BLC-67), 1954.

[39] R. Joslin. Aircraft laminar flow control. *Annual Review of Fluid Mechanics*, 30:1—29, 1998.

[40] J. Grassmeyer, A. Naghshineh-Pour, P. Tetrault, B. Grossman, R. Haftka, R. Kapania, W. Manson, and J. Schetz. Multidisciplinary design optimization of a strut braced wing aircraft with tip-mounted engines. *Department of Aerospace and Ocean Engineering, Virginia Polytechnic Institute and State University, Blacksburg, USA*, 1998.

[41] R. Turriziani, W. Lovell, G. Martin, J. Price, E. Swanson, and G. Washburn. Preliminary design characteristics of a subsonic business jet concept employing an aspect ratio 25 strut-braced wing. *Kentron International, Inc., an LTV Company, Hampton Technical Center, Hampton, Virginia*, 1980.

[42] G. Chiozzotto. Wing weight estimation in conceptual design: a method for strut-braced wings considering static aeroelastic effects. *German Aerospace Center*, 2016.

[43] R. Kulfan and J. Vachal. Wing planform geometry effects on large subsonic military transport airplanes. *Boeing Commercial Airplane Company*, 1978.

[44] H. Park. The effect on block fuel consumption of a strutted vs. cantilever wing for a short haul transport including strut aeroelastic considerations. *California*, 1978.

[45] V. Balabanov. Multidisciplinary design optimization in aerospace engineering. *Structures Engineering Design Analysis and Support*, 2020. URL `https://www.mdpi.com/journal/aerospace/special$_$issues/multi_des_optim_aero_eng`.

[46] G. Vanderplaats. Numerical optimization techniques. computer aided optimal design: Structural and mechanical systems. *Mota Soares*, 1987. URL `https://doi.org/10.1007%2F978-3-642-83051-8$_$5`.

[47] C. Irving. Wide-body-the triumph of the 747. *William Morrow and Company, New York*, 1993.

[48] J. Martins and A. Lambe. Multidisciplinary design optimization: a survey of architectures. *AIAA*, 2013.

[49] M. Hutchison, E. Unger, W. Mason, B. Grossman, and R. Haftka. Variable-complexity aerodynamic optimization of a high-speed civil transport wing. *Journal of Aircraft*, 31(1), 1994.

[50] S. Doyle, K. Alston, and T. Winter. Developing the aerodynamics module for the integrated multidisciplinary optimization object system. *49th AIAA Aerospace Sciences Meeting*, 2011.

[51] A.-T. Le, K. Gray, and M. L. Baker. Building the aerodynamics module for the integrated hypersonic aeromechanics tool. *42nd AIAA Aerospace Sciences Meeting*, 2004.

[52] D. Myers. Matrix formulation of co-kriging. *Journal of the International Association for Mathematical Geology*, 14(3), 1982.

[53] A. I. J. Forrester, A. Sóbester, and A. J. Keane. Multi-fidelity optimization via surrogate modelling. *Proceedings of the Royal Society A: Mathematical, Physical and Engineering Sciences*, 463(2088), 2007.

[54] L. Huang, Z. Gao, and D. Zhang. Research on multi-fidelity aerodynamic optimization methods. *Chinese Journal of Aeronautics*, 26(2), 2013.

[55] M. Xiao, G. Zhang, P. Breitkopf, P. Villon, and W. Zhang. Extended co-kriging interpolation method based on multifidelity data. *Applied Mathematics and Computation*, 323, 2018.

[56] H. Bungartz and M. Schafer. Fluid-structure interaction: modelling, simulation, optimization. *Springer*, 2006.

[57] R. Palacios and C. Cesnik. Low-speed aeroelastic modeling of very flexible slender wings with deformable airfoils. *AAIA*, AIAA-2008- 1995, 2008.

[58] ANSYS. *Fluid-Structure Interaction*, accessed 24 February 2021. URL `https://www.ansys.com/products/platform/multiphysics-simulation/fluid-structure-interaction`.

[59] N. Bartoli, T. Lefebvre, S. Dubreui, R. Olivanti, R. Priem, N. Bons, J. Martins, and J. Morlier. Adaptive modeling strategy for constrained global optimization with application to aerodynamic wing design. *Aerosp. Sci*, Technol. 90, 2019. URL `https://doi.org/10.1016/j.ast.2019.03.041`.

[60] G. Giangaspero, D. MacManus, and I. Goulos. Surrogate models for the prediction of the aerodynamic performance of exhaust systems. *Aerosp. Sci*, Technol. 92, 2019. URL `https://doi.org/10.1016/j.ast.2019.05.027`.

[61] A. Batrakov, A. Kusyumov, S. Mikhailov, and G. Barakos. Aerodynamic optimization of helicopter rear fuselage. *Aerosp. Sci*, Technol. 77, 2018.

[62] M. Berci and R. Cavallaro. Hybrid reduced-order model for the aeroelastic analysis of flexible subsonic wings-a parametric assessment. *Aerospace*, 2018.

[63] F. Torrigiani, J. Walther, R. Bombardieri, R. Cavallaro, and P. Ciampa. Flutter sensitivity analysis for wing planform optimization. *International Forum on Aeroelasticity and Structural Dynamics IFASD 2019*, 2019.

[64] J. Issac, R. Kapania, and J. Barthelemy. Sensitivity analysis of flutter response of a wing incorporating finite-span corrections. *NASA-CR-202089*, 1994.

[65] M. Berci and F. Torrigiani. Multifidelity sensitivity study of subsonic wing flutter for hybrid approaches in aircraft multidisciplinary design and optimisation. *Switzerland*, 2020.

[66] S. Kontogiannis and M. Savill. A generalized methodology for multidisciplinary design optimization using surrogate modelling and multifidelity analysis. *Optimization and Engineering*, 2020. URL `https://doi.org/10.1007/s11081-020-09504-z`.

[67] I. Chittick and J. Martins. An asymmetric suboptimization approach to aerostructural optimization. *Optim Eng*, 10(133), 2009. URL https://doi.org/10.1007/s11081-008-9046-2.

[68] T. Kumano, S. Jeong, S. Obayashi, and et al. Multi-disciplinary design optimization of wing shape for a small jet aircraft using kriging model. *AAIA*, AIAA 2006-932, 2006.

[69] T. Zill, P. Ciampa, and B. Nagel. Multi-disciplinary design optimization in a collaborative distributed aircraft design system. *AAIA*, AIAA 2012- 0553, 2012.

[70] S. Rajagopal and R. Ganguli. Multi-disciplinary design optimization of a uav wing using kriging based multi-objective genetic algorithm. *AAIA*, AIAA 2009-2219, 2009.

[71] M. Nikbay, L. Öncü, and A. Aysan. Multi-disciplinary code coupling for analysis and optimization of aeroelastic systems. *Journal Aircraft*, 2009.

[72] Y. Lian and M. Liou. Aero-structural optimization of a transonic compressor rotor. *Journal Propul Power*, 2006.

[73] D. Bryson and M. Rumpfkeil. Multifidelity quasi-newton method for design optimization. *AIAA*, 56 (10):4074–4086, 2018. URL https://doi.org/10.2514/1.J056840.

[74] B. Peherstorfer, K. Willcox, and M. Gunzburger. Survey of multifidelity methods in uncertainty propagation. inference optimization. *SIAM Rev*, 60(3):550–591, 2018. URL https://doi.org/10.1137/16M1082469.

[75] A. Chaudhuri, R. Lam, and K. Willcox. Multifidelity uncertainty propagation via adaptive surrogates in coupled multidisciplinary systems. *AIAA*, 56(1):235–249, 2018. URL https://doi.org/10.2514/1.J055678.

[76] J. R. R. A. Martins and A. Ning. Engineering design optimization. *University of Michigan and Brigham Young University*, 2020.

[77] Y. Zuo, G. Chen, Y. Li, and Z. Gao. Efficient aeroelastic design optimization based on the discrete adjoint method. *Transactions of the Japan Society for Aeronautical and Space Sciences*, 57(6): 343–351, 2014.

[78] A. Swift and K. Badcock. Inter-grid transfer influence on transonic flutter predictions. *AAIA*, AIAA 2010-3049, 2010.

[79] K. Badcock, A. Rampurawala, and B. Richard. Intergrid transformation for aircraft aeroelastic simulations. *AAIA*, AIAA 2003-3512, 2003.

[80] C. Yang, L. Wang, C. Xie, and Y. Liu. Aeroelastic trim and flight loads analysis of flexible aircraft with large deformations. *Sci China Tech Sci*, 55:2700–2711, 2012.

[81] S. Aly, M. Ogot, R. Pelz, and et al. Jig-shape static aeroelastic wing design problem: A decoupled approach. *Journal Aircraft*, 39:1061–1066, 2002.

[82] A. Sherif, M. Ogot, R. Pelz, and M. Siclari. Jig-shape static aeroelastic wing design problem: a decoupled approach. *Journal Aircraft*, 39:1061–1066, 2002.

[83] H. Ashley. On making things the best - aeronautical uses of optimization. *Journal of Aircraft*, 1982.

[84] J. A. Green. Aeroelastic tailoring of aft-swept high-aspect-ratio composite wings. *Journal of Aircraft*, 1987.

[85] B. Grossman, Z. Gurdal, G. J. Strauch, W. M. Eppard, and R. T. Haftka. Integrated aerodynamic/structural design of a sailplane wing. *Journal of Aircraft*, 1988.

[86] J. Sobieszczanski-Sobieski and R. Haftkas. Multidisciplinary aerospace design optimization: Survey of recent developments. *Structural Optimization*, 14(1), 1997.

[87] I. Kroo. Mdo applications in preliminary design: Status and directions. *AAIA*, AIAA 97-1408, 1997.

[88] A. Giunta, V. Balabanov, D. Haim, B. Grossman, W. Mason, L. Watson, and R. Haftka. Multidisciplinary optimization of a supersonic transport using design of experiments theory and response surface modelling. *The Aeronautical Journal*, 1997.

[89] D. Knill, A. Giunta, C. Baker, B. Grossman, W. Mason, R. Haftka, and L. Watson. Hsct configuration design using response surface approximations of supersonic euler aerodynamics. *AIAA*, AIAA 98-0905, 1998.

[90] T. Megson. Aircraft structures for engineering students (fourth edition), 2007.

[91] K. Grebici, D. Wynn, and P. Clarkson. Modelling the relationship between uncertainty levels in design descriptions and design process duration, 2008.

[92] L. Ilcewicz, D. Hoffman, and A. Fawcett. Comprehensive composite materials, 2000.

[93] 1 - introduction to aerospace materials, 2012. URL `https://www.sciencedirect.com/science/article/pii/B9781855739468500017`.

[94] J. Woidasky, C. Klinke, and S. Jeanvré. Materials stock of the civilian aircraft fleet, 2017. URL `https://res.mdpi.com/recycling/recycling-02-00021/article_deploy/recycling-02-00021-v3.pdf`.

[95] Ansys. Introduction to ansys mechanical apdl, Accessed on 14 april 2021. URL `https://www.ansys.com`.

[96] A. Inc. Ansys mechanical apdl element reference, 2011. URL `https://www.mm.bme.hu/~gyebro/files/vem/ansys_14_element_reference.pdf`.

[97] Abaqus. Mesh convergence, Accessed on 23 april 2021. URL `https://abaqus-docs.mit.edu/2017/English/SIMACAEGSARefMap/simagsa-c-ctmmeshconverg.htm`.

[98] Simscale - mesh quality, Accessed on 14 june 2021. URL `https://www.simscale.com/docs/simulation-setup/meshing/mesh-quality/`.

[99] G. R. Bhashyam. Ansys mechanical-a powerful nonlinear simulation tool. *Ansys, Inc*, 1(1):39, 2002.

[100] In fea, what is linear and nonlinear analysis?, Accessed on 7 june 2021. URL https://www.femto.eu/stories/linear-non-linear-analysis-explained/.

[101] P. Ghisbain. Application of a gradient-based algorithm to structural optimization, 2009.

[102] F. Afonso, G. Leal, J. Vale, E. Oliveira, F. Lau, and A. Suleman. The effect of stiffness and geometric parameters on the nonlinear aeroelastic performance of high aspect ratio wings. *Proceedings of the Institution of Mechanical Engineers, Part G: Journal of Aerospace Engineering*, 231(10): 1824–1850, 2017. doi: https://doi.org/10.1177/0954410016675893.

[103] S. Sreenath, U. Saravanan, and V. Kalyanaraman. Beam and shell element model for advanced analysis of steel structural members. *Journal of Constructional Steel Research*, 67(12):1789–1796, 2011. ISSN 0143-974X. doi: https://doi.org/10.1016/j.jcsr.2011.05.003. URL https://www.sciencedirect.com/science/article/pii/S0143974X11001519.

Appendix A

Results

A.1 High-Fidelity model

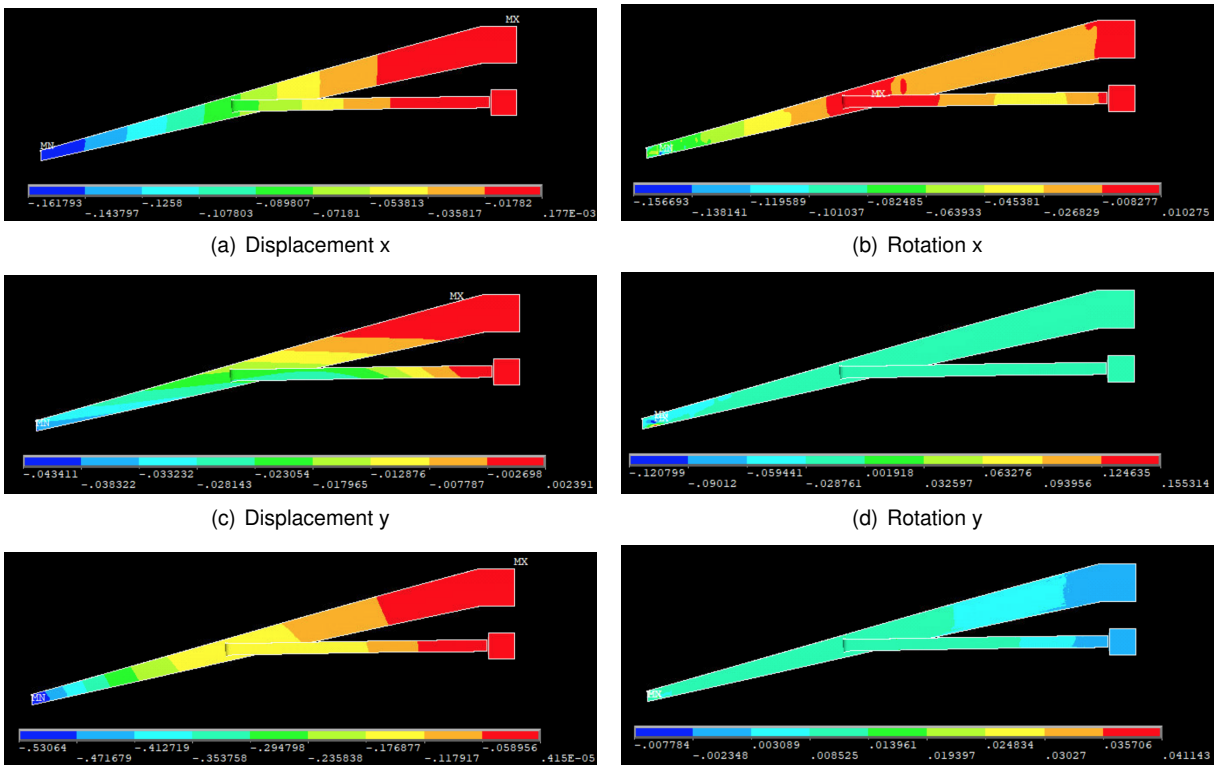

(a) Displacement x

(b) Rotation x

(c) Displacement y

(d) Rotation y

(e) Displacement z

(f) Rotation z

Figure A.1: Displacement and rotation results in x,y,z of the High-Fidelity model for the Cruise Case

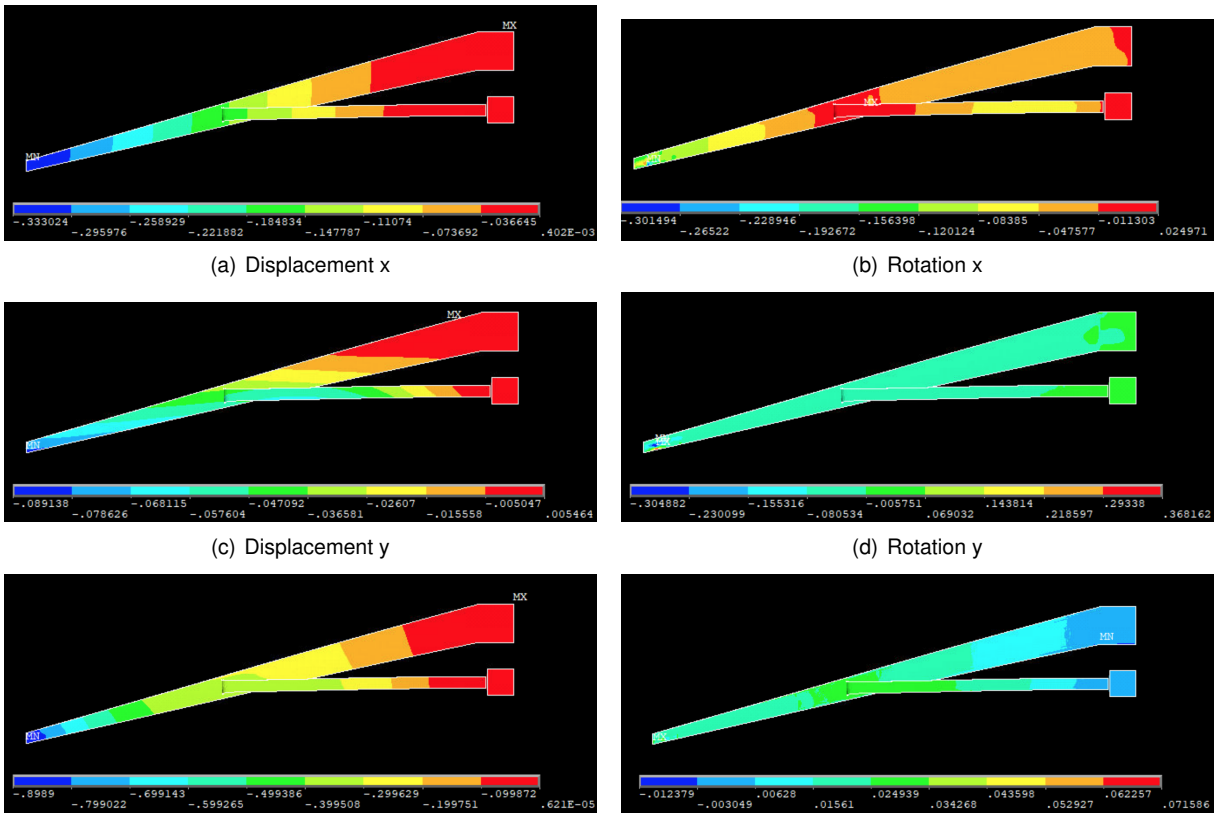

(a) Displacement x

(b) Rotation x

(c) Displacement y

(d) Rotation y

(e) Displacement z

(f) Rotation z

Figure A.2: Displacement and rotation results in x,y,z of the High-Fidelity model for the Maneuver Case

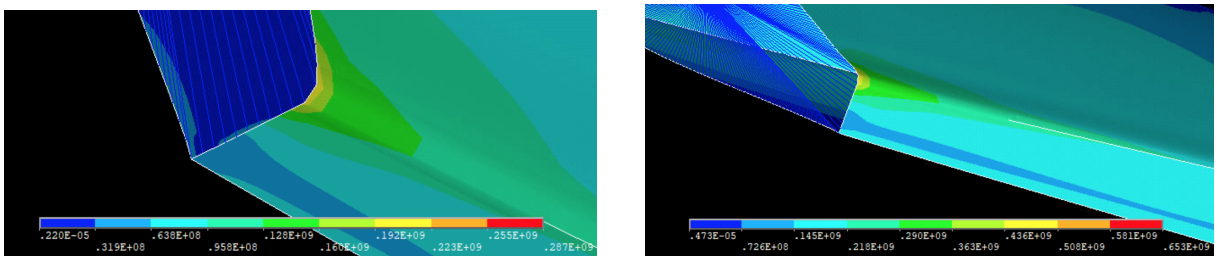

(a) Cruise

(b) Maneuver

Figure A.3: Maximum Von Misses stress area of the High-Fidelity model for the Cruise and Maneuver Cases

A.2 Comparison condensed and distributed loads High-Fidelity model

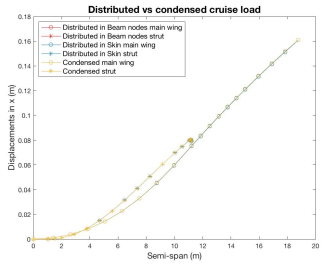

(a) Displacement x

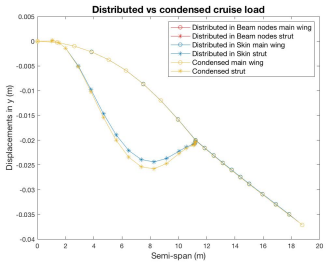

(b) Displacement y

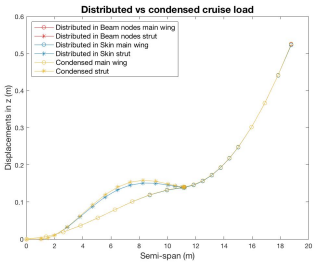

(c) Displacement z

Figure A.4: Displacement results of the condensed and distributed loads for the Cruise Case

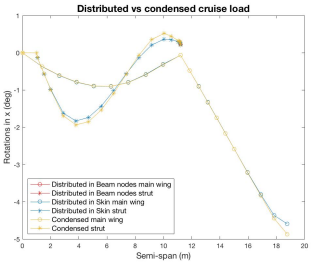

(a) Rotation x

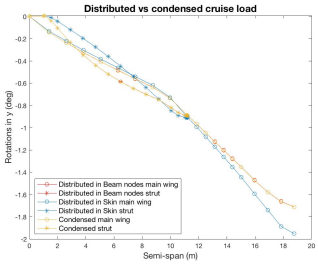

(b) Rotation y

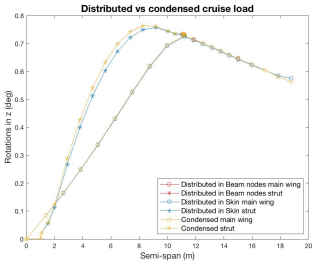

(c) Rotation z

Figure A.5: Rotations results of the condensed and distributed loads for the Cruise Case

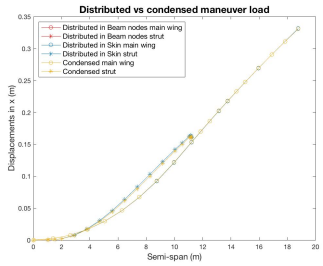

(a) Displacement x

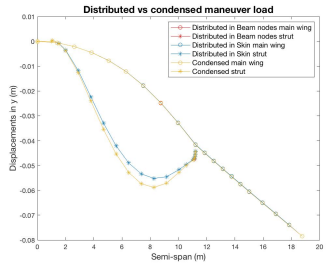

(b) Displacement y

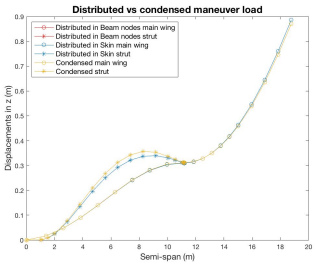

(c) Displacement z

Figure A.6: Displacement results of the condensed and distributed loads for the Maneuver Case

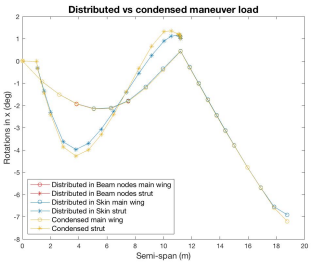

(a) Rotation x

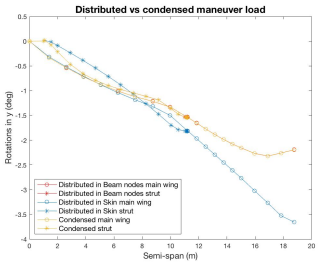

(b) Rotation y

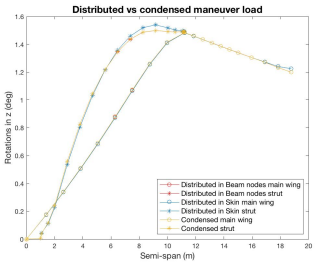

(c) Rotation z

Figure A.7: Rotations results of the condensed and distributed loads for the Maneuver Case

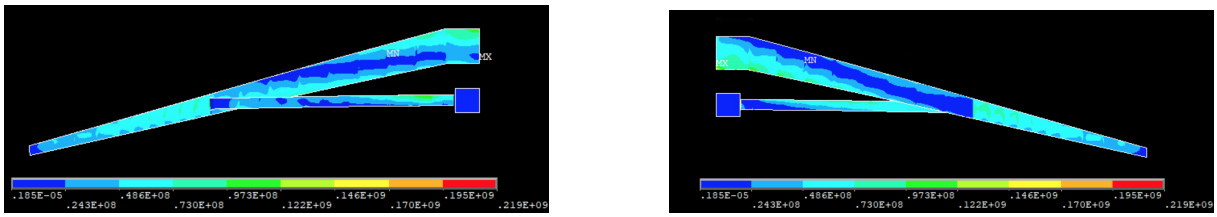

Figure A.8: Von Misses stress results of the condensed load for the Cruise Case

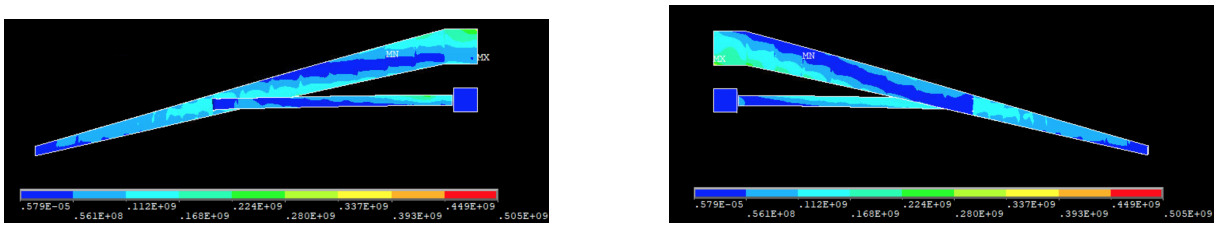

Figure A.9: Von Misses stress results of the condensed load for the Maneuver Case

A.3 Comparison High and Low-Fidelity models

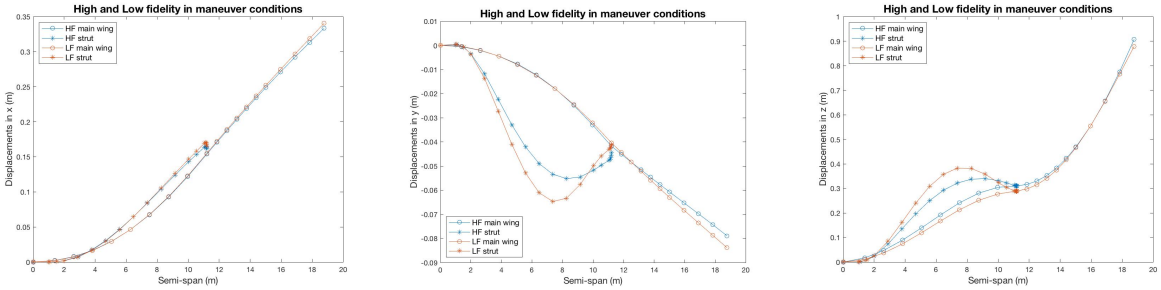

(a) Displacement x (b) Displacement y (c) Displacement z

Figure A.10: Displacement results of the High and Low-Fidelity models for the Maneuver Case

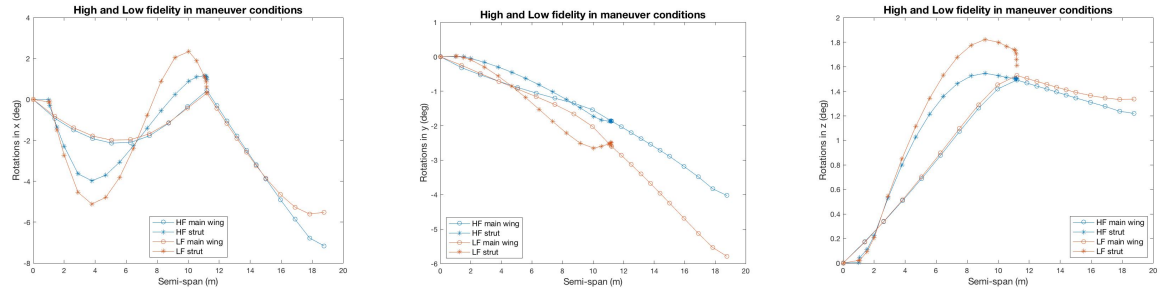

(a) Rotation x (b) Rotation y (c) Rotation z

Figure A.11: Rotations results of the High and Low-Fidelity models for the Maneuver Case

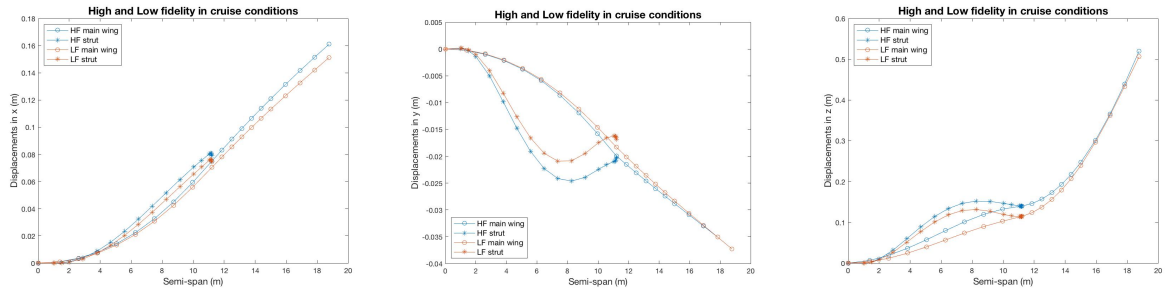

(a) Displacement x (b) Displacement y (c) Displacement z

Figure A.12: Displacement results of the High and Low-Fidelity models for the Cruise Case

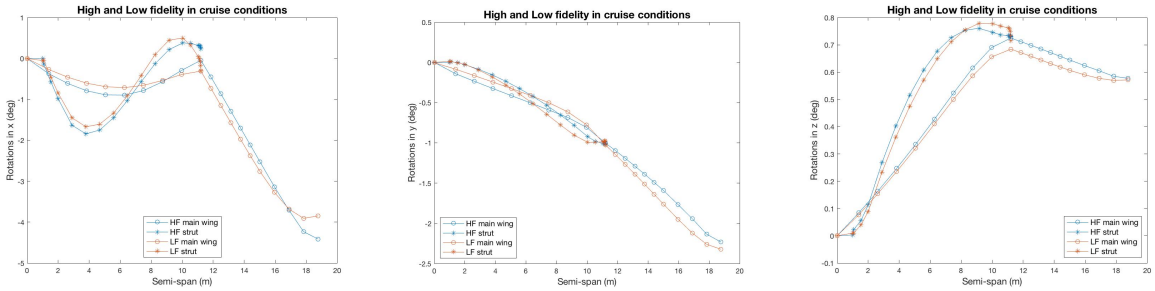

(a) Rotation x (b) Rotation y (c) Rotation z

Figure A.13: Rotation results of the High and Low-Fidelity models for the Cruise Case

A.4 Unconstrained optimization

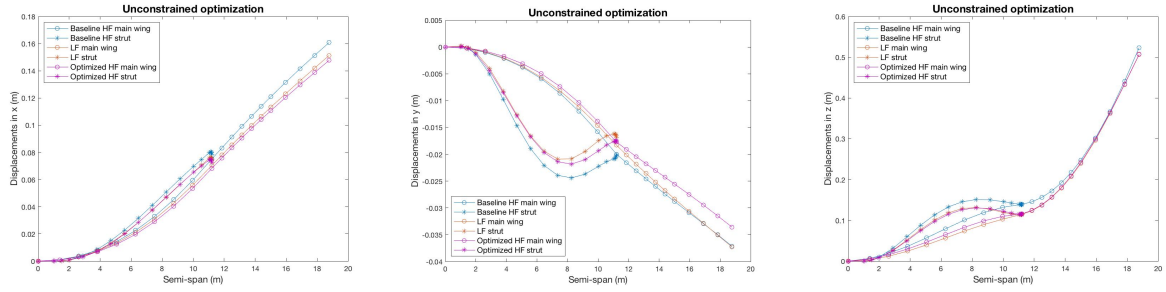

(a) Displacement x (b) Displacement y (c) Displacement z

Figure A.14: Displacements of the Unconstrained optimization, Baseline and LF thickness distributions

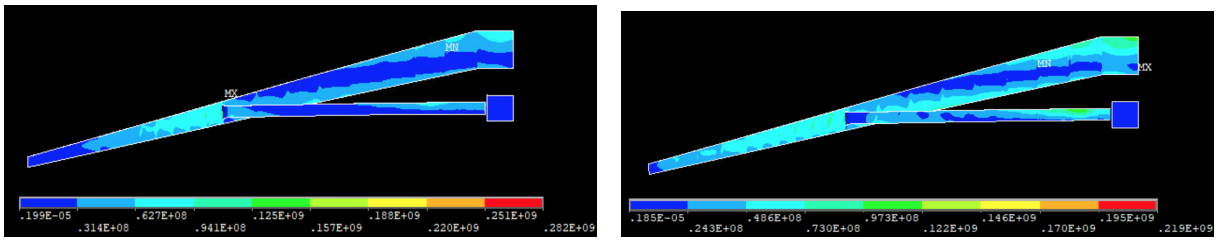

(a) Optimized thickness distribution (b) Baseline thickness distribution

Figure A.16: Von Misses stress results of the Optimized and Baseline thickness distributions in cruise

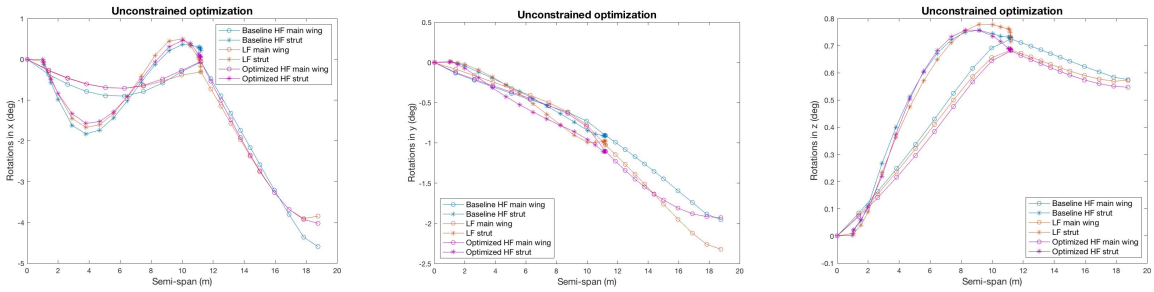

(a) Rotation x (b) Rotation y (c) Rotation z

Figure A.15: Rotations of the Unconstrained optimization, Baseline and LF thickness distributions

A.5 Constrained optimization

A.5.1 Baseline bounds

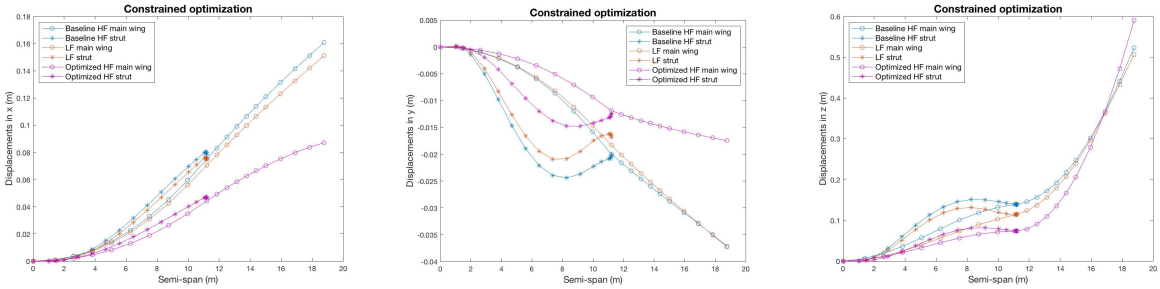

(a) Displacement x (b) Displacement y (c) Displacement z

Figure A.17: Displacements of the Constrained optimization (baseline bounds), Baseline and LF thickness distributions

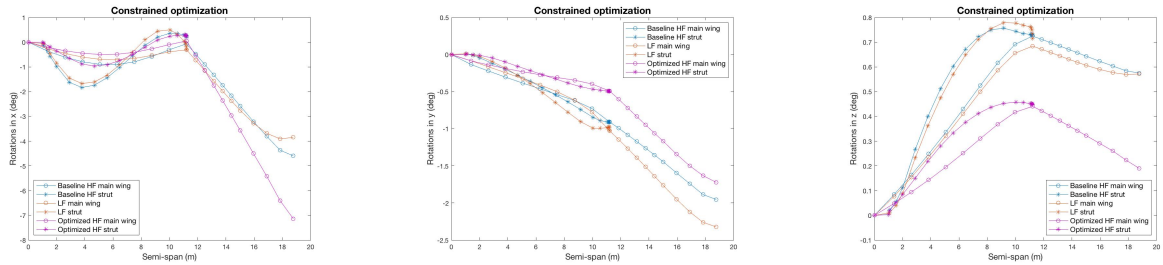

(a) Rotation x (b) Rotation y (c) Rotation z

Figure A.18: Rotations of the Constrained optimization (baseline bounds), Baseline and LF thickness distributions

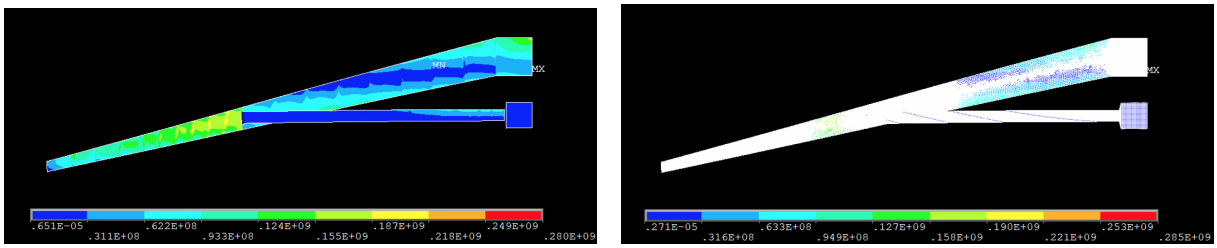

(a) Nodal solution (b) Element solution

Figure A.19: Von Misses stress results from the Constrained optimization with the baseline bounds

A.5.2 New bounds

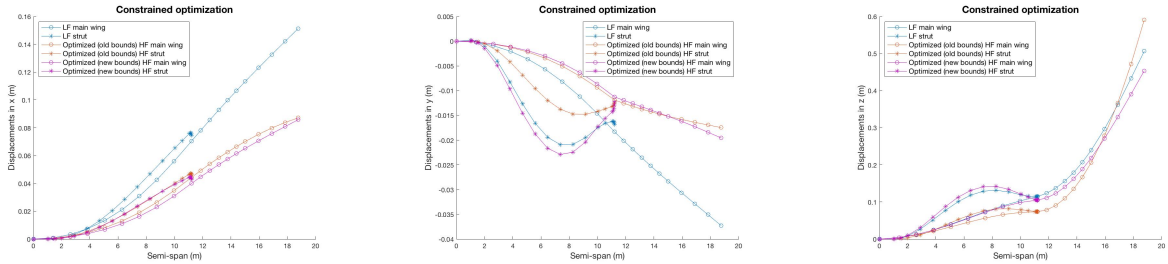

(a) Displacement x (b) Displacement y (c) Displacement z

Figure A.20: Displacement results of the Constrained optimization (new bounds), Baseline and LF thickness distributions

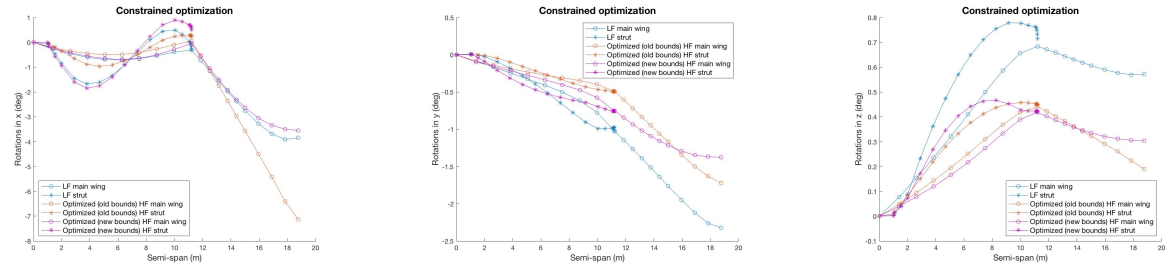

(a) Rotation x (b) Rotation y (c) Rotation z

Figure A.21: Rotation results of the Constrained optimization (new bounds), Baseline and LF thickness distributions

(a) Nodal solution (b) Element solution

Figure A.22: Von Misses stress results from the Constrained optimization with the new bounds

A.5.3 Added design freedom

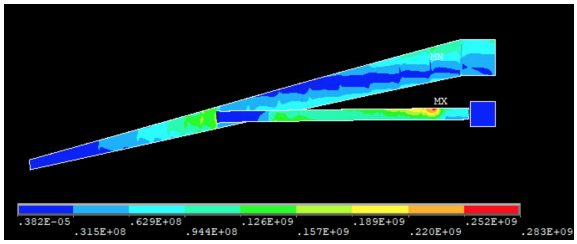

Figure A.23: Von Misses stress results from the Constrained optimization (two additional kinks, m = 3)

A.5.4 Jig shape optimization

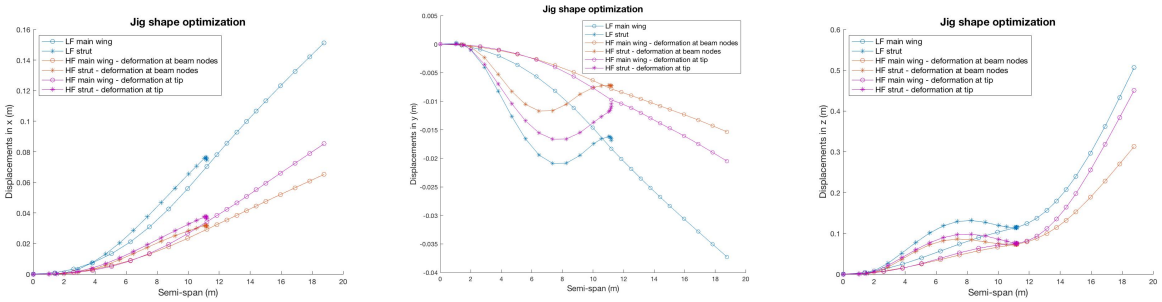

(a) Displacement x (b) Displacement y (c) Displacement z

Figure A.24: Displacements of the Jig shape optimization and LF thickness distributions

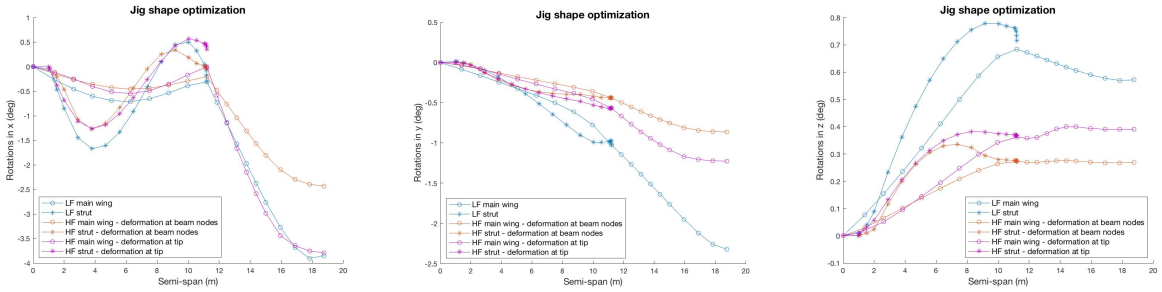

(a) Rotation x (b) Rotation y (c) Rotation z

Figure A.25: Rotations of the Jig shape optimization and LF thickness distributions

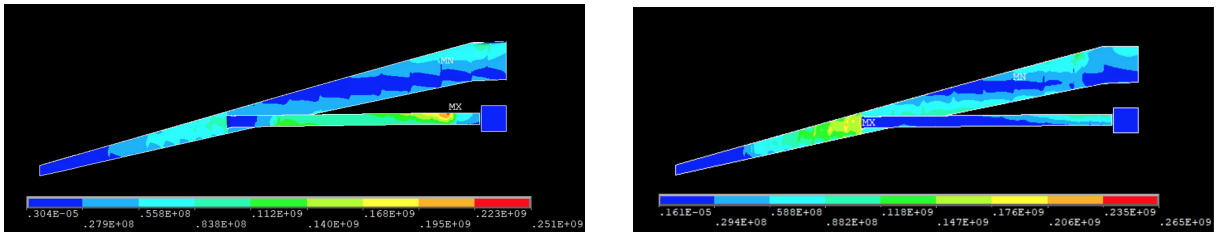

(a) "Optimized 1" (b) "Optimized 2 - interior point"

Figure A.26: Von Misses nodal stress results from the Jig shape optimization